

Electronic Theses and Dissertations, 2004-2019

2009

The Effect Of Heat Transfer Coefficient On High Aspect Ratio Channel Accompanied By Varying Rib Aspect Ratio

An Le
University of Central Florida

 Part of the [Mechanical Engineering Commons](#)
Find similar works at: <https://stars.library.ucf.edu/etd>
University of Central Florida Libraries <http://library.ucf.edu>

This Masters Thesis (Open Access) is brought to you for free and open access by STARS. It has been accepted for inclusion in Electronic Theses and Dissertations, 2004-2019 by an authorized administrator of STARS. For more information, please contact STARS@ucf.edu.

STARS Citation

Le, An, "The Effect Of Heat Transfer Coefficient On High Aspect Ratio Channel Accompanied By Varying Rib Aspect Ratio" (2009). *Electronic Theses and Dissertations, 2004-2019*. 4103.
<https://stars.library.ucf.edu/etd/4103>

THE EFFECT OF HEAT TRANSFER COEFFICIENT ON HIGH ASPECT RATIO CHANNEL ACCOMPANIED BY VARYING RIB ASPECT RATIO

by

AN LE

B. S. University of Central Florida, USA, 2009

A thesis submitted in partial fulfillment of the requirements
for the degree of Master of Science in Mechanical Engineering
in the Department of Mechanical, Materials, and Aerospace Engineering
at the University of Central Florida
Orlando, Florida

Summer Term
2009

© 2009 An Le

ABSTRACT

Heat transfer and pressure data were performed and reported on two different rigs. The first rig has an aspect ratio of (19:1) with two different inlet conditions and the second rig is composed of two different aspect ratio channels, (1:8) and (1:4). Rib turbulators were used as a flow disruptor scheme to enhance the heat transfer and friction factor. Rib aspect ratios ranging from (1:1) to (1:5) rib-height-to-width ratio were used.

The first channel rib-width-to-pitch (W_r/P) ratio was kept at 1/2 where flow was kept at relatively low Reynolds numbers, between 3000 and 13000. Results from the current tests showed that existing correlations could be used for high aspect ratio channels in predicting the effectiveness of the cooling scheme. Two different inlet conditions were tested; one was arranged so that the flow was hydrodynamically fully-developed at the entrance of the heated section, while the other uses an abrupt entrance from bleeding off mass flow from a horizontal channel. The heat transfer augmentation (compared to a well known and accepted correlation proposed by Dittus-Boelter) in these channels are extremely high with an average of 350% to 400%. However, this was accompanied by a substantial increase in the pressure drop, causing the overall thermal performance to increase between twenty to thirty percent.

The second channel rib-width-to-pitch ratio (W_r/P) ranges from 0.1, 0.3, and 0.5; the flow conditions are tested from 20,000 to 40,000 Reynolds number. Correlations for heat transfer and friction augmentation of the test data was also given. The test shows large rib blockage ratio does not demonstrate the best thermal performance; however it does give a high heat transfer augmentation ranging from 200 to 300 percent for both aspect ratios depending on the width of the used ribs.

ACKNOWLEDGMENTS

I would like to express my deepest gratitude to my advisor Professor Jayanta Kapat for the opportunity to learn and work at the Center for Advance Turbine and Energy Research Laboratory. I really appreciated the support, guidance and encouragement that he has given me. I also would like to thank my committee members, Professor Saptashi Basu, Professor Ali Gordon, and Ken Landis for their time and consideration.

I would like to say thank you to my colleagues in the laboratory, especially Mark Ricklick, Carson Slabaugh, Lucky Tran, and Michelle Valentino for their help and support through rig building, running tests and reviewing some of the data collected. Their advice and support were greatly valued.

I will forever be indebted to my parents and family who have always been with me and supported me through the rough and good times in my academic career.

TABLE OF CONTENTS

LIST OF FIGURES	vii
LIST OF TABLES	xi
NOMENCLATURES	xii
CHAPTER 1: INTRODUCTION	1
CHAPTER 2: LITERATURE REVIEW	7
CHAPTER 3: HIGH ASPECT RATIO CHANNEL	24
3.1 Fully developed entrance condition, Configuration A.....	24
3.1.1 Fully developed entrance condition test setup	24
3.2 Split entrance effect, Configuration B	31
3.3 High aspect ratio channel data analysis	36
3.3.1 Heat leakage and lateral conduction correction	36
3.3.2 Heat transfer coefficient calculation.....	38
3.3.3 Friction factor calculation	40
3.4 Results and discussion	41
3.4.1 Heat transfer results.....	41
3.4.2 Pressure distribution.....	47
CHAPTER 4: EFFECT OF VARYING RIB WIDTH	54
4.1 Channel setup.....	55
4.2 Results and discussion	60

4.2.1 Baseline configuration, smooth channel	61
4.2.2 Heat transfer results.....	66
4.2.3 Pressure distribution results.....	77
4.2.4 Channel's correlation	81
CHAPTER 5: CONCLUSION/FUTURE WORKS	85
APPENDIX: UNCERTAINTY CALCULATION.....	87
REFERENCES	118

LIST OF FIGURES

Figure 1: Materials advancement over the years, Sourmail [1]	3
Figure 2: Operating temperature throughout a typical aircraft engine (Rolls-Royce Trent 800), Sourmail [1]	4
Figure 3: Summary of temperature distribution throughout a cross section of a blade or vane, O'Donoghue [2]	5
Figure 4: Cooling schemes usage in the industry, Han [3]	6
Figure 5: Ribs characteristics parameters: p , e , w_r , α	7
Figure 6: Flow pattern using interferometry, Liou [27]	19
Figure 7: Summary of Nu/Nu_o versus ff_o from multiple authors, Ligrani [35]	22
Figure 8: High aspect ratio channel with hydrodynamically fully developed entrance, Configuration A setup	25
Figure 9: Spencer VB 007 blower	26
Figure 10: Venturi and pressure manometers used	27
Figure 11: Watlow silicone rubber heater	28
Figure 12: Variable alternating current (AC) transformer	28
Figure 13: Labview user interface screen	29
Figure 14 Cross-sectional view of the channel (top); Side view of the ribs in the main flow (bottom)	30
Figure 15: Overall setup of the Split entrance test channel, Configuration B	32
Figure 16: VB-110 Spencer blower	33

Figure 17: Different horizontal channel sizes (dimensions are given in term of vertical channel's hydraulic diameter).....	34
Figure 18: 2-D overview of the completed Configuration B setup	35
Figure 19: Contact resistance control volume	38
Figure 20: Configuration A results, normalized with Dittus –Boelter at different vertical channel Reynolds number	41
Figure 21: Configuration B, horizontal channel 1, Reynolds number of 20,000 at the exit of the horizontal channel.....	43
Figure 22: Configuration B, horizontal channel 2a, Reynolds number of 50,000 at the exit of the horizontal channel.....	43
Figure 23: Configuration B, horizontal channel 2b, Reynolds number of 100,000 at the exit of the horizontal channel.....	44
Figure 24: Speculated recirculation zone for Configuration B.....	45
Figure 25: Summary of the average heat transfer coefficient for all cases vs. Reynolds number of the vertical channel	47
Figure 26: Friction factor vs. Reynolds number for all cases.....	48
Figure 27: Friction factor augmentation vs. h augmentation data taken from Ligrani et al. [35]	50
Figure 28: Thermal efficiency of all cases versus Reynolds number	51
Figure 29: Thermal performance taken from Taslim [19].....	52
Figure 30: Cross section of the varying width channel.....	54
Figure 31: Varying rib width channel setup overview.....	56
Figure 32: Completed rig assembly	57

Figure 33: 1:4 Aspect ratio channel	57
Figure 34: 1: 8 Aspect ratio channel	58
Figure 35: Ribs close-up	58
Figure 36: Case 6 repeated with taped rib surface	59
Figure 37: Keithley multimeter.....	60
Figure 38: Smooth wall for 1:4 aspect ratio channel	62
Figure 39: Smooth wall for 1:8 aspect ratio channel	63
Figure 40: Area weighted average for the smooth channel of 1:8 aspect ratio.....	64
Figure 41a: Isovels from a (2:7) aspect ratio channel, Single Phase Heat Transfer Hand Book [29].....	65
Figure 42: Case 1, all walls heat transfer augmentation	67
Figure 43: Case 2, all walls heat transfer augmentation	68
Figure 44: Case 3, all walls heat transfer augmentation	69
Figure 45: Summary of all cases ran for 1:4 aspect ratio channel	70
Figure 46: Case 4, all walls heat transfer augmentation	71
Figure 47: Case5, all walls heat transfer augmentation	72
Figure 48: Case 6a, all walls heat transfer augmentation	73
Figure 49: Case 6b, all walls heat transfer augmentation	74
Figure 50: Summary of all cases ran for 1:8 aspect ratio channel	75
Figure 51: Flow pattern as a function of p/e Webb [13].....	76
Figure 52: 1:4 aspect ratio channel friction factor distribution.....	78
Figure 53: 1:8 aspect ratio channel friction factor distribution.....	78

Figure 54: Thermal performance for the 1:4 aspect ratio channel.....	79
Figure 55: Thermal performance for the 1:8 aspect ratio channel.....	80
Figure 56: Friction roughness function.....	82
Figure 57: Normalize friction roughness function.....	82
Figure 58: Heat transfer roughness function.....	83
Figure 59: Normalize heat transfer roughness function.....	84

LIST OF TABLES

Table 1: VB007 specification	26
Table 2: Venturi table and flow rate	27
Table 3: VB-110 Spencer blower specifications	33
Table 4: Test conditions specifications	34
Table 5: Rib width test runs	55

NOMENCLATURES

A	Projected area, m ²
AR	Aspect ratio
C _p	Specific heat capacity, J/(kg·K)
D _h	Hydraulic diameter, m
e	Height of rib, m
e ⁺	Roughness Reynolds number
<i>f</i>	Darcy friction factor
<i>f_o</i>	Darcy friction factor, Blasius correlation
G	Heat transfer roughness function
<i>h</i>	Heat transfer coefficient, W/m ² K)
H	Channel height, m
k	Thermal conductivity (W/(m·K))
L	Length of the test section, m
<i>m</i>	Mass flow rate (kg/s)
Nu	Nusselt number, (h·L)/k
Nu ₀	Nusselt number from Dittus-Boelter Correlation
P	Pitch
Pr	Prandtl number
<i>Q_{in}</i>	Power input (Watt)
R	Friction roughness function
Re	Reynolds number, ((V·D _h)/ν)

T	Temperature, T
W_r	Width of rib, m
W_c	Width of channel, m
V	Fluid Velocity, m/s
Y	Distance in the vertical direction, m

Greek Symbols

α	Rib orientation angle
ν	Kinematic Viscosity, Pa·s
ρ	Density, kg/m ³
η	Thermal Performance Factor, $(Nu/Nu_0)/((ff_o)^{1/3})$
κ	Thermal Conductivity, W/(mK)
ΔP	Static Pressure, $(P_{inlet} - P_{exit})$, Pa

Subscripts

<i>amb</i>	ambient
<i>b</i>	Bulk Fluid
<i>o</i>	Baseline Value
<i>w</i>	Wall

CHAPTER 1: INTRODUCTION

Developing new cooling schemes has been an ongoing process for decades, especially in the turbomachinery industry. In the harsh environment of complex machinery, such as the turbine, the most critical part exists in the first row of blade and vane, where the exiting or operating temperature of the working fluid far exceeds the melting point of the blade's material composition.

Two different advancements in technology makes this possible, one is to develop a new generation of material, and the other is to have a better cooling scheme. Figure 1 shows the material advancement over the years, but this is still not enough to survive the operating condition of the turbine. From Figure 1, it seems that with the current technology we can only push the blade material limit to operate at only 1150°C using *single crystal alloys* and *thermal barrier coating* (TBC) which survives only up to 1200°C. TBC are ceramic materials, therefore it is impossible for major components to be made out of only these types of materials. Ceramic materials are usually poor performers of tensile stresses, where in the turbine, a tremendous tensile loading occurs due to centripetal acceleration from the rotation of the shaft and every blade connected to it. Blade made out of only TBC will not be able to survive both the operation temperature and the major loading.

Single crystal alloys can survive the major loading component of the turbine, but not the immense temperature. Therefore, current turbine blade and vanes consist of both materials, where the blades are coated with TBC to help protect the blades/vanes alloys, creating a larger thermal resistance between the hot gas and the blade's composition. TBC alone cannot protect

anything without some other type of cooling scheme. If no cooling schemes are used in conjunction, the entire blade or vane will certainly reach the same temperature of the hot gas once the turbine reaches steady state, and catastrophic failure occurs once all blades and vanes are melted away.

Figure 2 shows the operating condition of a Rolls-Royce Trent 800 aircraft engine. The temperature at the exit of the combustion chamber and the inlet to the high pressure turbine (HPT) far exceeds the temperature limit of materials currently available, seen in Figure 3. From Figure 2 and Figure 3, it can be seen that with the current technology, material advancement alone is not enough to produce materials capable of surviving the temperature distribution in the entire gas turbine engine. Other cooling schemes are needed in conjunction of material advancement to be able to push for higher operating temperature.

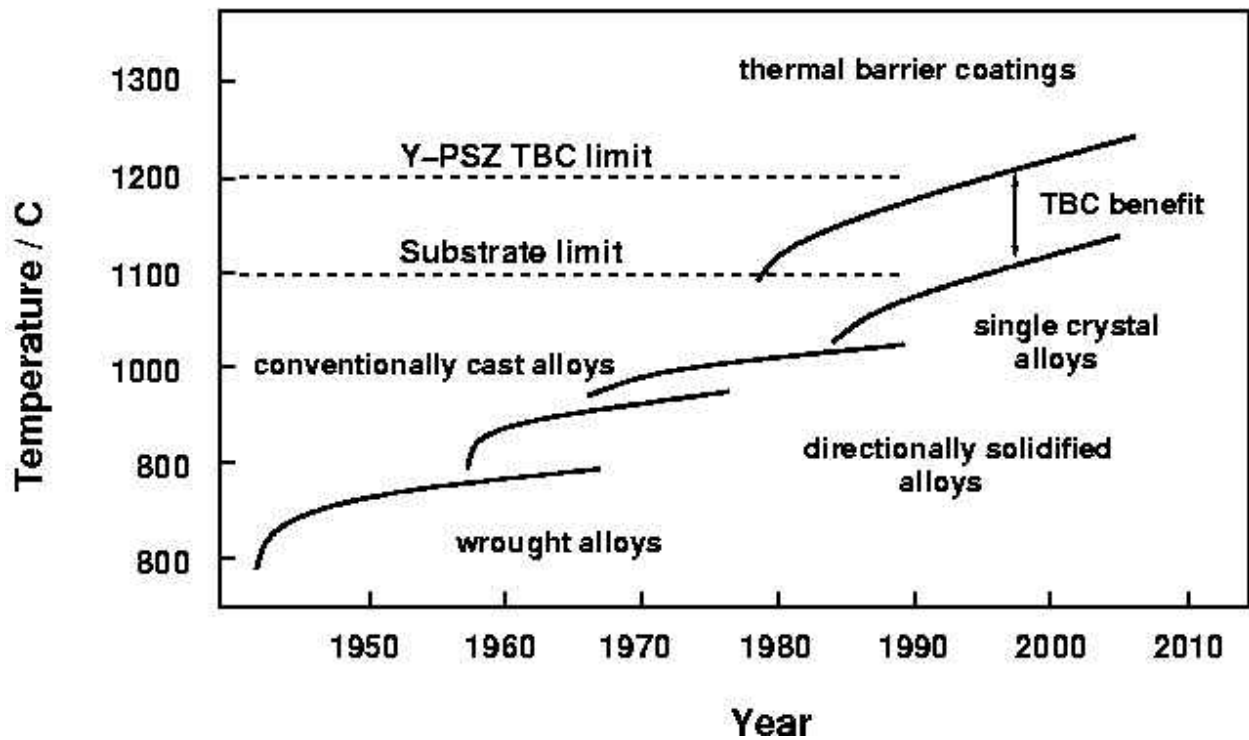


Figure 1: Materials advancement over the years, Sourmail [1]

Two major schemes of cooling are currently utilized by industries, they are active and passive cooling. An example of active cooling is film cooling, where coolant from the compressor is used to create a thin cooling film, blanketing over the critical portion of the blade to protect it. This method is more expensive since it bleeds air from the compressor to cool the blade, after so much work has been spent to compress atmospheric air to such high operating pressure. Once the compressed air is used for coolant, it can never be used to produce any work; hence the name “spent” air. Passive cooling involves mostly internal flow and flow trippers. By turbulating the flow, the boundary layer develops and re-attaches to the heat transfer surface to increase the heat transfer rate. The main objective of turbulators is to cause more mixing to the main stream of air, which makes the thermal information from the viscous layer of the boundary

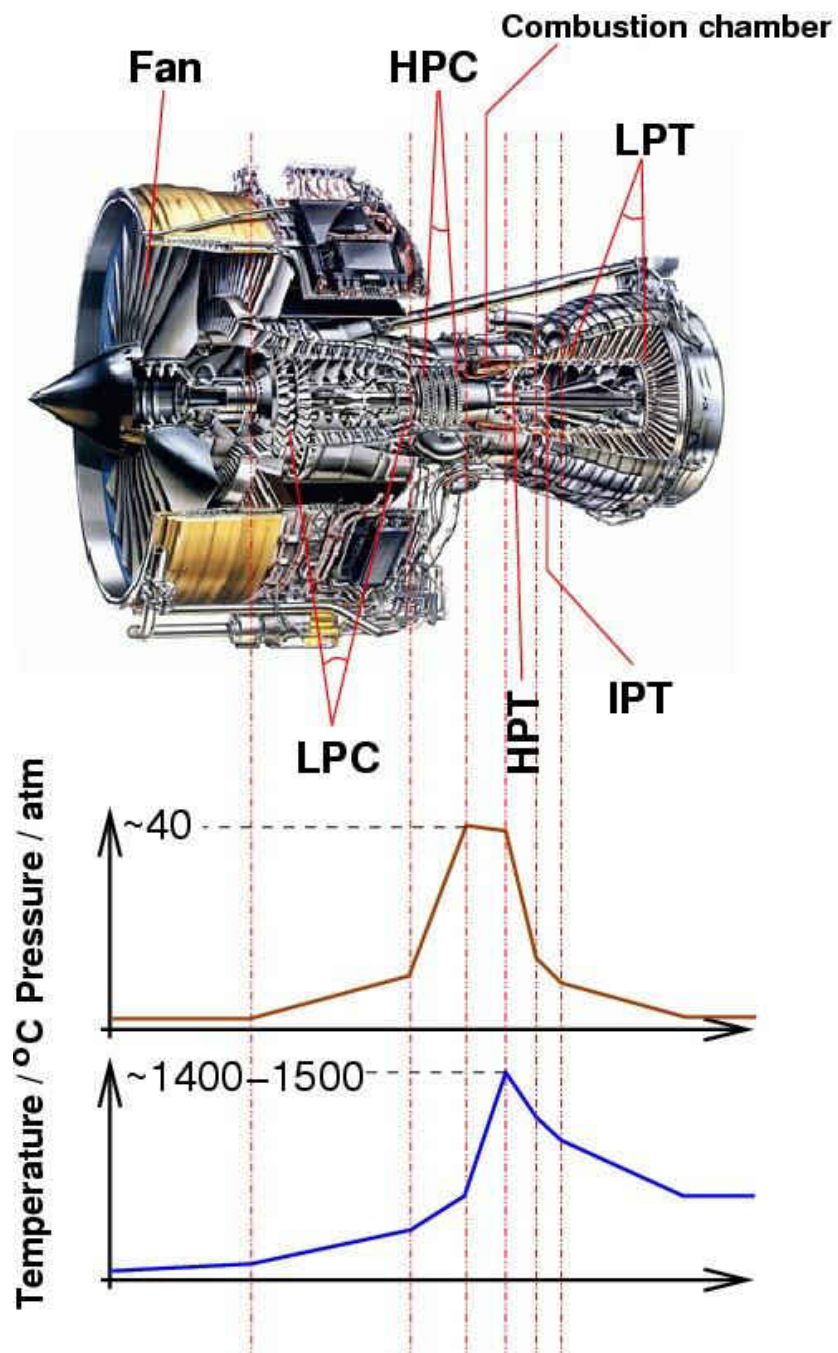


Figure 2: Operating temperature throughout a typical aircraft engine (Rolls-Royce Trent 800), Sourmail [1]

layer to penetrate quickly toward the bulk core (main) flow, thus removing heat quickly away from the heated surface.

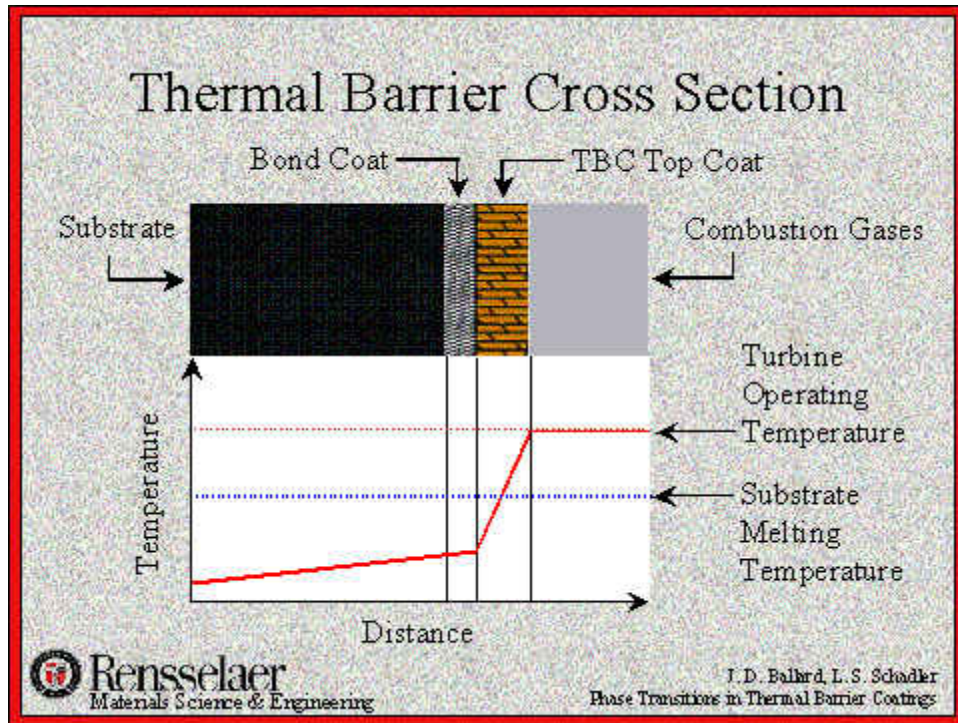


Figure 3: Summary of temperature distribution throughout a cross section of a blade or vane, O'Donoghue [2]

Figure 4 shows an example of the complicated inner working of a classical turbine blade. This blade has three different cooling scheme designs within it; the film cooling and impingement effect at the leading edge of the air foil, rib turbulators in single and multiple passes along the mid-core, and pin-fin cooling at the trailing edge.

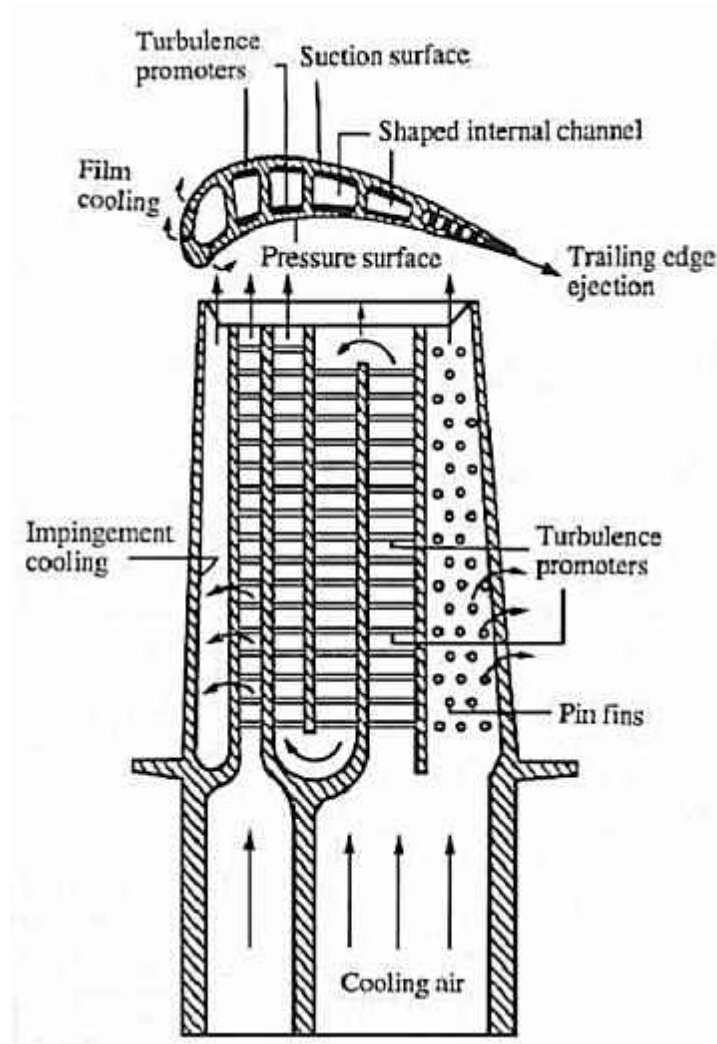


Figure 4: Cooling schemes usage in the industry, Han [3]

Through the years, rib turbulators were used dominantly in turbines, generators, heat exchangers and any other devices which require cooling. Ribs are utilized for their ease of manufacturing and cooling effectiveness.

This research shall look into high aspect ratio of channel as well as ribs aspect ratio and their effect on the average heat transfer augmentation throughout the length of the channel.

CHAPTER 2: LITERATURE REVIEW

Figure 5 shows the characteristics of rib turbulator definitions. By varying any of these basic parameters (different parameters changes the characteristics of the flow slightly), which can either be beneficial or harmful to the overall thermal performance or efficiency of the design. A vast majority of studies have already mentioned parametric designs to find the most efficient characteristics of rib shapes, size, orientation, and installation walls. Some of these works are discussed below.

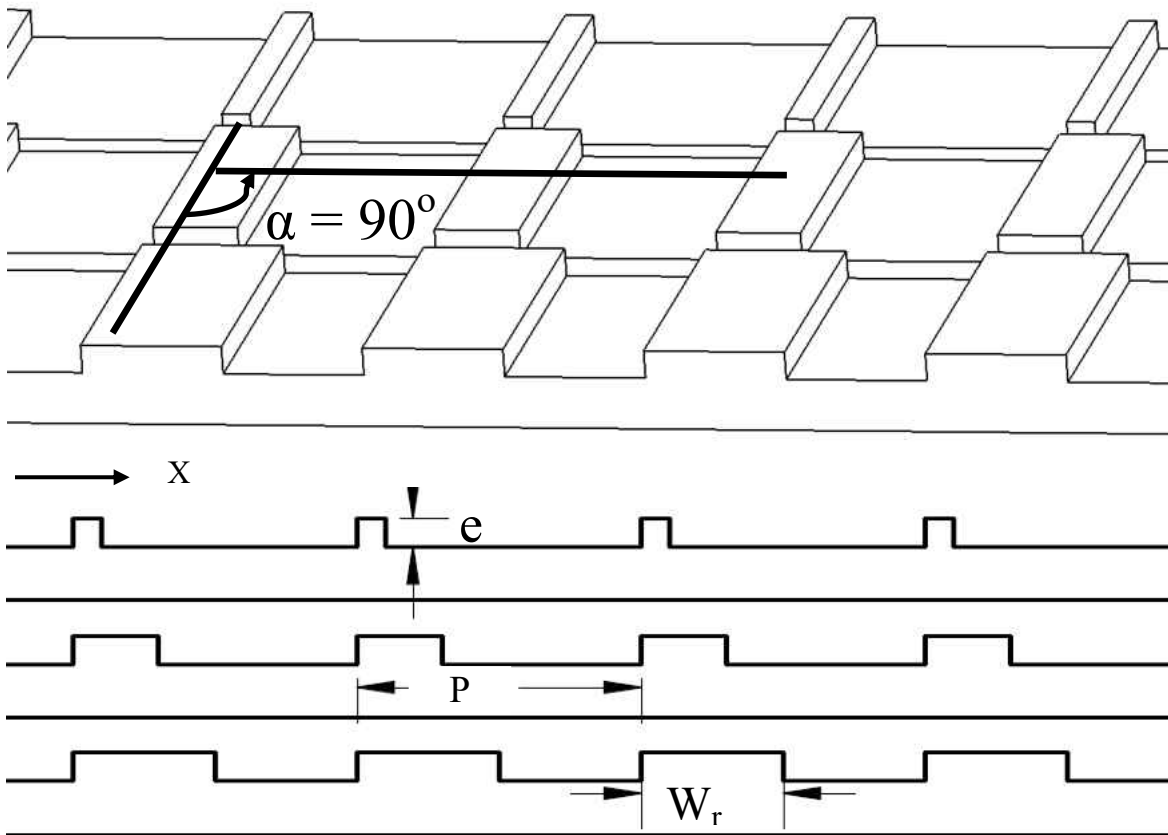


Figure 5: Ribs characteristics parameters: p , e , w_r , α

Rib turbulators have been used for decades in the turbine industries for pushing the limit of heat transfer rate in internal cooling airfoils. One major contributor to the vast amount of resources available on internal cooling using turbulators is definitely credited to J. C. Han. J. C. Han has written scores of papers that utilized the effects of many ribs and channel parameters; for instance, the number of passes, rib orientations, rib arrangements, pitch to height ratio, etc.

In 1978, Han [4] wrote a paper experimentally proving that ribs arranged symmetrically or staggered, does not create a difference in regards to the friction factor, as well as the heat transfer augmentation. In this experiment, he varies both the pitch-to-rib-height (P/e) and the rib-height-to-hydraulic diameter (e/D_h). He reported that $P/e = 10$ produces the largest friction factor and heat transfer coefficient. For $P/e = 10$, the flow is able to re-attach to the wall surface between the ribs, which causes the largest heat transfer coefficient to occur at the re-attachment zone, very close to the next rib. For $P/e > 10$, the re-attachment zone is far from the next rib, and the new boundary layer begins to re-develop. For $P/e < 10$, the flow did not reattach, thus there was a smaller loss in momentum from the fluid to the space between the ribs. Different rib's angle of attacks were also tested, ribs were oriented at 90° , 75° , 45° and 20° with respect to the flow. For the most part, the rib aspect ratio (e/W_r) remained at a one or square rib for a parallel plate channel configuration. He also showed that the angle of attack of 45° provided the optimum thermal performance of all the difference cases ran.

In 1983, Han [5] then changes the channel from two parallel plates to a square channel. Again, the most important aspect of this work was to determine the effect of rib pitch-to-height and rib height-to-hydraulic-diameter ratios on friction factor and heat transfer coefficient with ribs attach to two opposite walls. The e/D_h varied from 0.021 to 0.063 and P/e varied from 10 to

40 for a range of Reynolds number between 7,000 and 90,000. Han reported that rib walls produced an increase of about 1.7 to 2.2 times the Stanton number over the four smooth walls.

Han then used the same channel as in [5] to perform another parametric study of the angle of attack effects on heat transfer and friction factor. The same range of Reynolds number as in [5] and an $e/D_h = 0.021, 0.042, \text{ and } 0.063$ were used for [6-8]. He reported that for an angle of attack of 30 to 45 degrees, the heat transfer rate is 20 to 10% respectively higher than the ribs oriented normal to the main flow. At the same time, these oblique ribs also required 50 to 20% less pumping power to drive the flow correspondingly. These findings greatly affected the nature of turbine blade design.

In 1988, Han and J. S. Park [9] also considered the entrance effects of the channel on heat transfer and friction factor with channels that were associated with rib turbulators. They considered three different channel aspect ratios for this case, $AR = 1, 2 \text{ and } 4$. The rib height-to-hydraulic diameter ratio (e/D_h) used were varied from 0.047 to 0.078, with pitch-to-rib-height varying from 10 to 20. Not only that, the rib orientation also used an angle of attack ranging from $90^\circ, 60^\circ, 45^\circ \text{ or } 30^\circ$. Local data for heat transfer using thermocouples for the first three hydraulic diameters were reported as well the rest of the channel's averaged result. For the first three X/D_h , the heat transfer coefficient enhancement follows a wavy pattern, meaning that the local heat transfer enhancement varies greatly with relative location to the rib.

With the same setup as in [9], Han explored more channel aspect ratio dependent characteristics in [10]. Han [10] did a more in depth study of the channel aspect ratio with width-to-height ratios of $\frac{1}{4}, \frac{1}{2}, 1, 2, \text{ and } 4$. Only the rib angle of attack of 90° was considered in

this study. The pitch-to-rib height ratio also varied from 10 to 20, and only two walls are mounted with rib turbulators. He reported that the Nusselt number ratio displayed the same trend for different channel aspect ratios, but the local heat transfer coefficient ratios were higher in larger aspect ratio channels. In other words, Nusselt number ratio was larger in channels ($W_c/H = 2$ and 4) versus channels with aspect ratio of ($W_c/H = 1/2$ and $1/4$). This is due in part by the larger aspect ratio channels having a larger rib exposure area.

Han et al. [11] expanded the study of rib turbulators yet again. This paper examined the effect of everything stated above and the effect of parallel vs. crossed arrangement of rib on two walls with the orientation at a number of different angles with respect to the main fluid flow. Han reported that the crossed ribs produced a slightly lower heat transfer performance than the parallel ribs. He reported a 5 to 10 percent variation of heat transfer coefficient between the two and the cross ribs also produced a higher friction factor augmentation.

To have a more closely related turbine problem, Han and Zhang [3] studied a case which involves a channel with three passes that represents a portion of the air foil internal cooling channel in Figure 4. They also changed the measurement method to incorporate mass transfer as a way to model heat transfer on a local level throughout the channel. Naphthalene was evenly coated on the entire channel's surface and the flow was then supplied. To back out the heat transfer calculation, a measurement of the thickness of Naphthalene was recorded. In this case, the rate of sublimation of Naphthalene was directly a function of the heat transfer coefficient. The faster the rate of sublimation, the higher the heat transfer coefficient. The effect of the 180 degree turn in the channel caused a huge heat transfer augmentation to occur on the side walls.

This can only be seen in the second and third pass, only at locations right after the turn. The heat transfer augmentation benefit greatly after the first pass due to the turn, secondary effects also played an important role on the outcome of the local heat transfer coefficient near the turns. They also concluded that the parallel ribs with a 60° angle of attack produces the most uniform heat transfer coefficient in all three passes. This is the best design for any situation since uniform heat transfer rate relieve local thermal stress to the overall component which in turns increases life and dependency to the part.

Han and Zhang [12] then researched the effect of broken ribs and its effect on the overall heat transfer enhancement. They reported that the 60° parallel broken rib or the 60° V-shaped broken rib provided the highest heat transfer enhancement, compared to the 45° broken and V-shaped broken ribs and the 90° rib orientations. The 60° rib case has the highest heat transfer augmentation reported thus far, and at the same time, the friction factor augmentation is the same as the 45° parallel broken and V-shaped broken ribs.

For all of Han's paper [4-12], he always included a semi-empirical correlation to account for the heat transfer and friction augmentation using the law of the wall. The law of the wall was first proposed by Nikuradse in the 1950s using sand roughened surface in a circular tube. Han then extended these studies to include a correlation that can be applicable to the rib walls. Friction Roughness function and Heat Transfer Roughness function were used to capture of all his data in all of his papers in equation 1 and equation 2 respectively.

$$R = [12.31 - 27.07 * (\alpha/90^\circ) + 17.86 * (\alpha/90^\circ)^2] * (W/H)^m \quad (1)$$

$$\begin{aligned}
\text{Where } m &= -0.5 & \text{for } 60^\circ \leq \alpha \leq 90^\circ \\
m &= -0.5(\alpha/60^\circ)^2 & \text{for } 30^\circ \leq \alpha \leq 60^\circ \\
m &= 0 & \text{for } \alpha \leq 30^\circ
\end{aligned}$$

$$G = C(e^+)^n \quad (2)$$

$$\text{Where } 2/4 \leq W_c/H \leq 1$$

$$n = 0.35$$

$$C = 2.24, \text{ if } \alpha = 90^\circ$$

$$C = 1.8 \text{ if } 30^\circ \leq \alpha \leq 90^\circ$$

$$\text{for } 1/4 \leq W_c/H \leq 2/4$$

$$n = 0.35 * (W_c/H)^{0.44}$$

$$C = 2.24 * (W_c/H)^{-0.76}, \text{ if } \alpha = 90^\circ$$

$$C = 1.80 * (W_c/H)^{-0.76}, \text{ if } 30^\circ \leq \alpha \leq 90^\circ$$

And e^+ is the Roughness Reynolds Number, which can be defined in equation 3:

$$e^+ = (e/D_h) * Re \sqrt{f/2} \quad (3)$$

The Friction Roughness Function (R) is setup as a function of the pitch and rib height parameter.

$$\mathbf{R} = \sigma^*(P/e)^{0.53} \quad (4)$$

Webb et al. [13] was the first to extend the law of the wall to rib turbulators in pipes. They specified that the correlation was only dependent of P/e on the momentum roughness function (Friction Roughness Function) and independent of e/D_h . They specified a correlation for the Roughness Function to equal:

$$R = 0.95(P/e)^{0.53} \quad \text{for} \quad e^+ > 35$$

And the heat transfer Roughness function is:

$$G = 4.5(e^+)^{0.28}(\text{Pr})^{0.57}$$

$$\text{St} = f/\{\{\{\text{He}^+ - \text{Re}^+\}(2f)^{0.5} + 2\}$$

One thing to keep in mind is that in order for anyone to use these correlations, the friction factor must first be converted to Fanno Friction factor, which is 4 times less than the Darcy friction factor.

Chandra et al. [14] also analyzed a number of internal channel cooling involving rib turbulators. Unlike Han, Chandra tested the effect of varying the number of rib walls. He tested the following parameters: $P/e = 8$ and $e/D_h = 0.0625$ with ribs oriented perpendicular to the main flow and the channel aspect ratio was 2:1 (Width : Height). The friction factor augmentation increased from $2.85f_o$ to $12.4f_o$ depending on which wall containing the ribs and also the number of rib walls. With one rib wall, the heat transfer enhancement was 2.7 to 1.92 times more for Reynolds number ranging from 11,000 to 72,000. At the same time, the h augmented at a ratio of 1.64 to 1.15 for the adjacent smooth wall and a heat transfer augmentation of 1.5 to 1.08 for the

opposite smooth. With two opposite rib walls, a heat transfer augmentation of 2.96 to 2.04 for the same range of Reynolds number was reported and a heat transfer augmentation of 1.91 to 1.38 for the smooth walls. With all the rib walls added, a 3.24 to 2.17 times the heat transfer augmentation was reported. This study also reported the significance of the secondary flow, which occurs by the presence of the rib turtulators. With just one rib wall, the effect of heat transfer augmentation was also felt by the opposite wall.

Chandra et al. [15] extended the study by varying the number of rib walls. Like Han, Chandra used the friction roughness and heat transfer roughness functions to create a semi-empirical correlation. Instead of using a correlation similar to Han and Webb, Chandra determined the value for his channel as

$$R = 3.44 \quad \text{for} \quad e^+ \geq 120$$

And $G = (e^+)^{0.47} \quad \text{for} \quad e^+ \geq 120$

He concluded that with the increasing number of rib walls, the heat transfer augmentation also increases. The heat transfer augmentation increased by 6% from two ribbed walls to one ribbed wall, a 5% increase from three rib walls to two ribbed walls and a 7% heat transfer augmentation increase for four ribbed versus three. The friction roughness function is independent from Reynolds number.

In order to study the passages in a real turbine blade, Chandra and Han [16] used Naphthalene sublimation technique to evaluate heat transfer and pressure drop in a two pass channel with ribs oriented at 90°, 60°, and 45°. For the smooth wall alone, the first pass

produced a pressure and heat transfer similar to the available correlations of smooth pipes. However, in the second pass, due to the 180° turn, the pressure and heat transfer results were double as the amount of the smooth wall correlation. The augmentations amplified with the presence of the different ribs configurations. The angled ribs produced the largest heat transfer and friction augmentation over the 90° or normal rib orientation.

In 1998, Chandra [17] provided a thorough study of the different types of rib geometries and their effects on heat transfer and friction factor distribution. The turbulators' geometries which were tested included the square, cylinder, triangle, irregular hexagon and semi-circle shapes; along with the smooth wall was also tested. Again, copper ribs were glued onto two opposite walls in a square channel. Chandra concluded that square ribs produced the highest friction factor as well as the highest heat transfer augmentation; while rounded ribs produced lower friction and heat transfer augmentation. As a comparison, with the same rib base area, the square ribs exhibited 24% higher heat transfer than the circular ribs while creating 33% more pressure drop than the circular ribs.

Like Chandra, Taslim [18 - 21] also worked with rib geometries and their effects on the overall heat transfer and the pressure drop occurring inside the fully developed channels. Taslim and Spring [18] uses the thermochromatic liquid crystal method with two types of ribs tested, square and 2:1 rib-height-to-width ratio, they were arranged in staggered fashion on two opposite walls oriented at 90° to the flow. Their rounded corner rib counterparts were also tested. Different rib aspect ratios were tested due to the minimum practical limit of turbulator size which existed in air-craft engines on the order of 0.010inches in size. With the built-in rib machining

tolerance of 0.002 – 0.003 inches, then the actual rib may vary as much as $\pm 30\%$. Hence this study also helped to characterize the effect of rib aspect ratio as well as rib spacing on the overall heat transfer and friction factor augmentation. With high blockage ratio, $e/D_h = 0.22$, the optimum P/e appears to be around 8, and by considering only the manufacturing tolerance (30% change in rib size), this may result up to 40% deviation in the Nusselt number from the targeted heat transfer coefficient. Taslim concluded that there was an optimum turbulator spacing (P/e) for every given turbulator blockage ratio (e/D_h) and rib aspect ratio, the sensitivity of Nusselt number to P/e decreases as e/D_h decreases.

Taslim [19] expressed an interest in heat transfer enhancement on the rib surface. This was not previously reported in any publication, since ribs are usually glued to the surface of the channel and the uniform temperature between the rib and the channel surface was assumed. For the current test, ribs were staggered in a square duct with rib orientation 90° to the flow. Taslim also considered the effect of rib blockage ratio, three different rib heights were chosen, e/D_h of 0.133, 0.167 and 0.25; with spacing P/e of 5, 7, 8.5 and 10. Taslim reported that the rib average heat transfer coefficient was much higher than the average of the wall and the rib pitch-to-height ratio of 8.5 constantly produces the best augmentation. Most importantly, the thermal performance decreases with an increase in blockage ratio.

To further study the internal channel cooling, Taslim [20] tested a configuration with relatively large blockage ratio. He investigated a channel with 22% blockage ratio using square and trapezoidal cross-sectional area channels with ribs arranged staggered and normal to the flow. Ribs were added to 2, 3, or 4 walls on both cases of the square and trapezoidal channel

cross section. The test involved the use of thermochromatic liquid crystal for local data of heat transfer; from this data, the heat transfer coefficient is highest at the top of the large rib.

Taslim [21] uses large blockage ratio ribs to further the study of the effect of rib shapes. In this case, he used a square channel with non-square ribs, the ribs has an aspect ratio of $e/W_r = 0.667$ or $W_r/e = 1.5$ with P/e varying from 5, 8.5, and 10. A maximum blockage ratio of $e/D_h = 0.25$ (25 percent), rounded corner ribs were used. The ribs were assembled in staggered manner on two opposite walls with a variation in blockage ratio. Taslim reported that low aspect ratio ribs produce lower pressure drop, along with the decrease in heat transfer coefficient. He concluded that for high blockage ratio, square, and low aspect ratio ribs, the results were insensitive to the pitch-to-height ratio changes in the location of the ribs.

Besides Taslim, others also explored the effect of wide shapes and their benefits in internal cooling channels. Casarsa [22] characterized the velocity and heat transfer field in a high blockage ratio channel. Casarsa uses the Particle Image Velocimetry and liquid crystal thermometry to study the flow pattern, secondary flow, and the local region of high heat transfer in a square cross section channel. The ribs are 30% of the channel's height and mounted on one wall with 90° relative to the main flow.

Wright [23] studied the effects of different rib widths mounted at an angle relative to the flow with a low aspect ratio channel. Wright reported a decrease of space between the ribs in addition to a decrease in the friction factor.

Experimenting with rib shapes is not new, Lewis [24] has tested the effect of rib shapes since 1975. During this time, he tested the different rib geometries and also created correlations to determine the friction and heat transfer roughness function.

Papers written by Liou [25-27] also added to the vast amount of turbulated internal channel cooling flow research. Liou [25] studied the local flow field and heat transfer in a repeated ribbed rectangular channel. Laser holographic interferometry measurements were made and the results were verified with computational fluid dynamics (CFD) using fully elliptic two dimensional Navier-Stokes equations with k- ϵ model. The results from the experiments matched with the results predicted by the CFD model. Both the interferometry and CFD captures the effect of the recirculation zone before and after the ribs, and depending on the spacing (rib-height-to-pitch) ratio, the reattachment of the main flow to the channel wall might not be obtainable.

Liou [26] again uses Laser holographic interferometry and thermocouples to study the flow in a rectangular channel with P/e varying from 10, 15 and 20 and e/D_h varies between 0.063, 0.81 and 0.106. The laser interferometer reveals that there are two major peaks of high enhancement, they are located slightly downstream of the rib's leading edge and a 0.5 to 1.0 rib height upstream of the reattachment point on the wall. Hot spot occurs at the back face of the rib and from 0 to 1 rib height on the wall right after each rib.

Unlike other authors, Liou [27] completely detached the rib location from the wall. This means that the flow can go over and under the ribs. Figure 6 shows the different scenarios which occurred and how the flow reacts if there was a gap under the rib. The first photograph in Figure 6 illustrated a normal scenario of glued ribs, showing the flow of a normal rib. The reattaching zone and the newly formed boundary layer effect on the top of each rib were also shown. The main aim for the detached ribs was to completely eliminate the local hot spots that occur around

the rear of the ribs. The reported thermal performance was actually worse than the smooth wall for high Reynolds number in these detached wall cases.

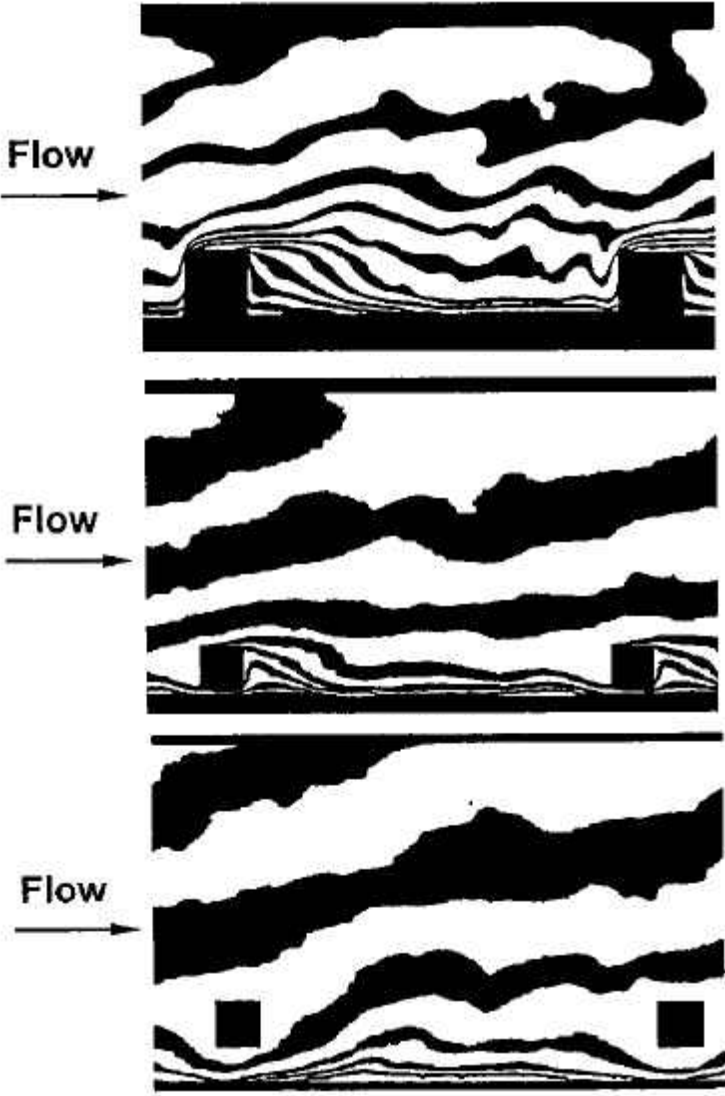


Figure 6: Flow pattern using interferometry, Liou [27]

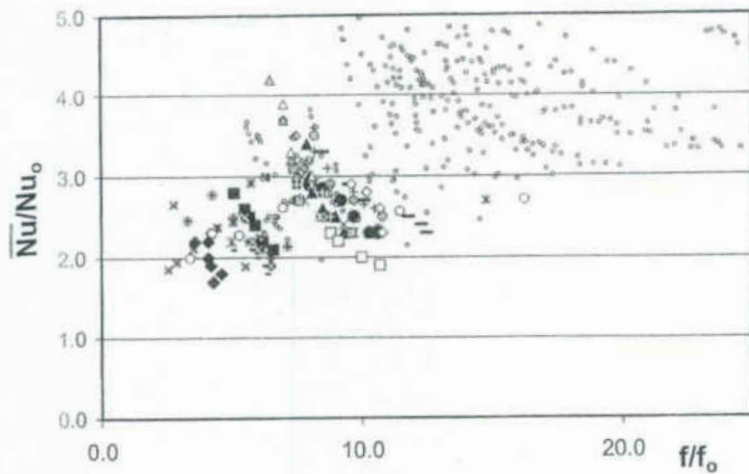
Large channel aspect ratio papers were also presented in many existing literatures. Sparrow [28] tested a very high aspect ratio channel ($W_c/H = 18$) using naphthalene sublimation technique. Sparrow only tested a smooth channel for this case; he only wanted to capture the effect of symmetrical versus asymmetrical heating from the channel boundary condition. The difference of the heat transfer coefficient reported varied only by 7 percent; resulting in the symmetrical heating having the best performance. The calculation for the 7% is found in the Heat Transfer Handbook [29] based on the correlation for symmetrical versus asymmetrical heating.

Zhang [30] also studied large aspect ratio channels. Instead of using only ribs, he included grooves at strategic locations; this is to accomplish mitigating the secondary flow effects happening after every row of ribs. With the groove in place, there is extra surface area, thus increasing the heat transfer coefficient when compared to the projected area. Zhang reported that there was an increase of 36% for the channel with ribs and groove present versus only rib.

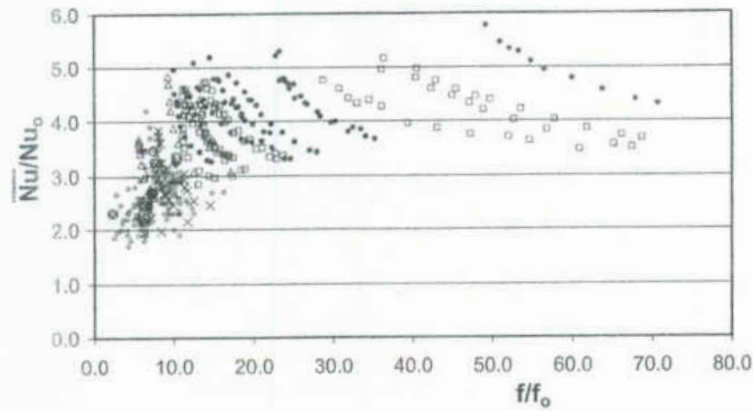
Both Olsson [31] and Cai [32] experimented with channels that are 8:1 aspect ratio. Olsson used a wide variety of rib designs and arrangements; he tested cross, parallel, cross V-shaped, and parallel V-shaped ribs. Smoke wire visualization and LDV (Laser Doppler Velocimetry) were used for flow visualization and measurements. Since smoke wires are used, only a small Reynolds number range would be viewable (range of 1100 and LDV at 3000). Cai on the other hand used smooth walls for the 1:8 aspect ratio in a two pass the channel. By changing the angle of the deflector board on the dividing channel, different heat transfer augmentation was obtained in the second pass. This will have a great impact on the design of the

internal channel arrangement in an airfoil. By using naphthalene sublimation technique, local data were also obtained.

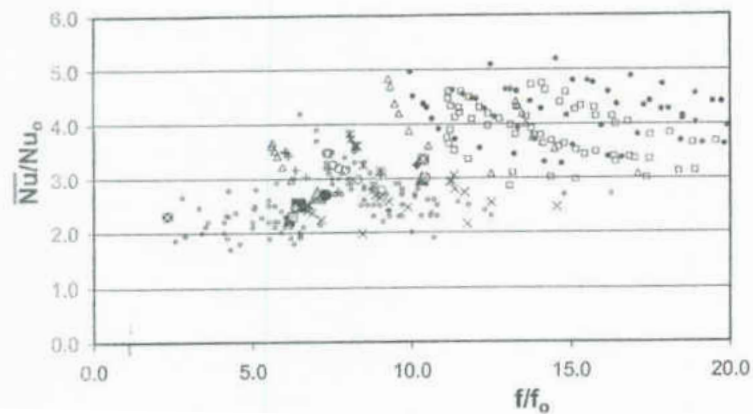
Although there are more papers available on this subject matter, the same parameters are repeated over and over again. There are other types of literature available that kindly summarized all valuable data to anyone who is interested in the subject. Chang [33] briefly summarized on the effectiveness of different rib geometry versus scaled and dimple surfaces. The *Single Phase Convective Heat Transfer Handbook* [29] also contains a summary and additional reference to hundreds of papers on convective heat transfer alone. Everything Han has done plus different schemes of internal heat transfer and the cooling of different turbine components can be found in Han's book [34]. Also Ligrani [35] did an extensive summary of different cooling schemes used up to the year 2003. He compared techniques like pin-fin arrays, dimpled surfaces, rib turbulators and swirl chambers performed by past authors. Results from Ligrani on rib turbulators are summarized below in Figure 7.



a)



b)



- × 30 deg continuous Han and Park Ref. 52
- ≠ 45 deg continuous Han and Park Ref. 52
- × 60 deg continuous Han and Park Ref. 52
- 90 deg continuous Han and Park Ref. 52
- × 90 deg continuous Han et al. Ref. 53
- × 60 deg parallel Han et al. Ref. 53
- 60 deg crossed Han et al. Ref. 53
- + 60 deg V-up Han et al. Ref. 53
- 60 deg V-down Han et al. Ref. 53
- 45 deg parallel Han et al. Ref. 53
- ◆ 45 deg crossed Han et al. Ref. 53
- ▲ 45 deg V-up Han et al. Ref. 53
- 45 deg V-down Han et al. Ref. 53
- 60 deg continuous Han et al. Ref. 54
- ◇ 60 deg broken Han et al. Ref. 54
- △ 60 deg V-broken Han et al. Ref. 54
- 60 deg V-continuous Han et al. Ref. 54
- ◇ 90 deg continuous Han et al. Ref. 54
- ◇ 90 deg broken Han et al. Ref. 54
- ⋈ Delta forward Han et al. Ref. 54
- △ Delta backward Han et al. Ref. 54
- Wedge continuous Han et al. Ref. 54
- ◇ Wedge broken Han et al. Ref. 54
- Data from Refs. 55,61,96,97

- 90 deg in-line Cho et al. Ref. 61
- ⋈ 90 deg shifted Cho et al. Ref. 61
- ▲ 60 deg parallel in-line Cho et al. Ref. 61
- 60 deg parallel shifted Cho et al. Ref. 61
- ◇ 60 deg cross in-line Cho et al. Ref. 61
- 60 deg cross-shifted Cho et al. Ref. 61
- ◇ 60 parallel in-line, staggered gaps Cho et al. Ref. 61
- ◆ 60 deg parallel shifted, staggered gaps Cho et al. Ref. 61
- △ 60 deg cross in-line, staggered gaps Cho et al. Ref. 61
- 60 deg cross shifted, staggered gaps Cho et al. Ref. 61
- ≠ 60 deg parallel in-line, two row gaps Cho et al. Ref. 61
- ◇ 60 deg cross in-line, two row gaps Cho et al. Ref. 61
- 90 deg continuous Taslim and Wadsworth Ref. 96
- 45 deg continuous Taslim and Lengkong Ref. 97
- × 90 deg staggered continuous Taslim et al. Ref. 55
- △ 45 deg staggered continuous Taslim et al. Ref. 55
- × 45 deg staggered V-down Taslim et al. Ref. 55
- 45 deg staggered V-up Taslim et al. Ref. 55
- + 45 deg staggered discrete Taslim et al. Ref. 55
- Data from Refs. 52,53,54

Figure 7: Summary of Nu/Nu_0 versus f/f_0 from multiple authors, Ligrani [35]

From different studies, there was not enough papers available involving the entrance effects on an extremely high aspect ratio channel with turbulators. The effect of high blockage ratio in conjunction with ribs and the change of channel aspect ratio have not been looked into. Therefore the objective of this paper is to provide some average heat transfer and frictional data occurring in high aspect ratio channel and the impact of rib width changes while keeping the pitch-to-rib-height-ratio constant.

CHAPTER 3: HIGH ASPECT RATIO CHANNEL

3.1 Fully developed entrance condition, Configuration A

Two different test sections were executed for this thesis. The first was composed of very high aspect ratio channel using copper blocks with appropriate opening milled out material; and the second channel was composed of 4 different walls assembled together to create a sharp cornered channel with copper blocks overlaying the inner surface at the heat transfer test section.

3.1.1 Fully developed entrance condition test setup

In laboratories, the fully developed conditions were usually tested. In part, due to the limited amount of time and resources available, and the different correlations derived can be used universally. Figure 8 shows a 3D model of the high aspect ratio channel with the hydrodynamically fully developed portion.

From Figure 8, the entrance of the test section is made of Plexiglas at $\frac{3}{4}$ inches thick and the total entrance length is $35 D_h$. Copper bars are used for the test section with a (19:1) aspect ratio channel milled out. Fiber glass clamps are used for both structure support of the test section and for providing adequate loads to prevent air leakage from the channel once all copper blocks are assembled. Teflon was used as the guide rail during the assembly process and as insulation material during the heat transfer tests.

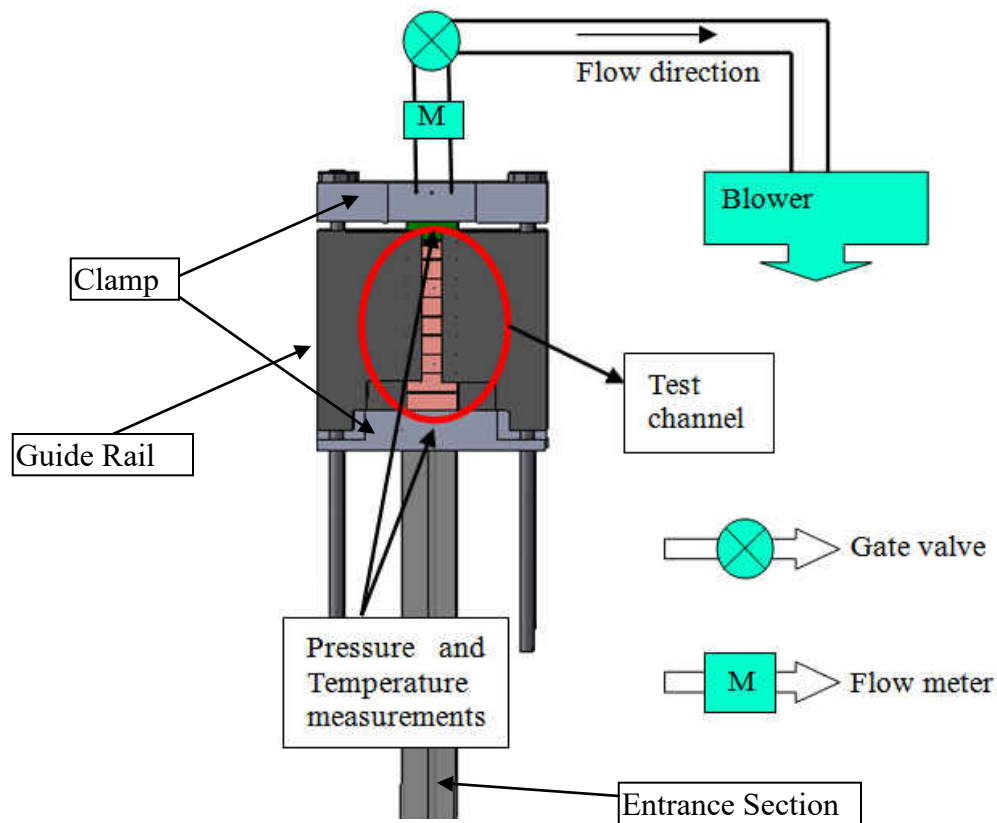


Figure 8: High aspect ratio channel with hydrodynamically fully developed entrance, Configuration A setup

Equipments used

The driving force behind the whole test section was a VB-007 blower (Figure 9) by Spencer with the specification provided in Table 1. The blower was configured in suction mode, with air drawn from the room, maintained at 25 ± 2 °C.



Figure 9: Spencer VB 007 blower

Table 1: VB007 specification

SPECIFICATIONS

Model No.	Freq	Maximum Volume		Maximum Operating Pressure		Maximum Operating Vacuum			Standard Voltage	FLA Current	Locked Rotor Current	Speed	Estimated Acoustical Noise Level @ 1.5m	Weight	
		cfm	m ³ h	"H ₂ O	mbar	"H ₂ O	mbar	hp						Volts	Amperes
VB-007S	60	107	181.8	51	127	45	112.1	1	115/208-230, 1Ø	12.4/6.5-6.2	89/40.2-44.5	3450	70dba@60Hz	65	29.5
	50	89	151.2	35	87.2	32	79.7	1	100-110/220, 1Ø	12.7-12.4/6.2	72.7-80/40	2850		65	29.5
VB-007	60	107	181.8	51	127	45	112.1	1	200-230/460,3Ø	2.7-2.8/1.4	20.9-24/12	3450	64dba@60Hz	50	22.7
	50	89	151.2	35	87.2	32	79.7	.83	190/380-415,3Ø	2.8/1.4-1.5	20/10-9.2	2850		50	22.7

Maximum Ambient Temperature: 104°F/40°C. Maximum Internal Motor Temperature: 311°F/155°C.

The flow rate was measured using a series of venturi meters. Venturi meters are basically converging diverging nozzles which utilized the Bernoulli’s equation to back calculate the flow rate. Venturi required the pressure drop measurement across it to resolve for the flow rate. Figure 10 shows an example of the venturi used along with the pressure manometers. Table 2 lists a summary of the different venturi. The appropriate venturi needed to be selected for the

different cases and tests depends on the analyzed flow rate. For the high aspect ratio simple channel, only venturi 3 and 4 were used. A gate valve was connected downstream from the venturi to adjust the flow rate.



Figure 10: Venturi and pressure manometers used

Table 2: Venturi table and flow rate

	Model	Testing Flowrate (scfm)	Pipe – Throat Size
Venturi 1	PCVF1C2A1	> 100	2” – 65
Venturi 2	PVBRFAAA2C	20 – 70	2” – 20
Venturi 3	PVBRCAAA3A	≥ 7	1” – 38
Venturi 4	PCBRAAAA1C	2 – 7	½” -- 10

For the required high density power, each copper block was powered using a pair of Watlow Silicone Rubber heaters. Each pair of heaters was wired in parallel configuration and controlled independently using a variable AC (alternating current) transformer. A total of 9 copper blocks were used, with a total of 18 heaters and 9 transformers used. Figure 11 and Figure 12 shows an example of the heater and transformer respectively. Regular multimeters obtained from Home Depot were used to get voltage and resistance reading in the pair of heaters.



Figure 11: Watlow silicone rubber heater



Figure 12: Variable alternating current (AC) transformer

Each copper block also contained three type T thermocouples to measure the temperature. The thermocouples are located at $\frac{1}{4}$, $\frac{1}{2}$ and $\frac{3}{4}$ of the way in the block at the mid-plane. All of these thermocouples read the same temperature during testing which provided a check and backup in case of one or two failures. All three thermocouples reported the same temperature, within the uncertainty of the thermocouples ± 1 °C; this was due to the copper having a high thermal conductivity and was verified using Biot number calculation. All thermocouples were collected using a data acquisition system from Measurement and Computing Inc. and Labview was used as a data acquisition program. An example of the Labview program interface is shown in

Figure 13.

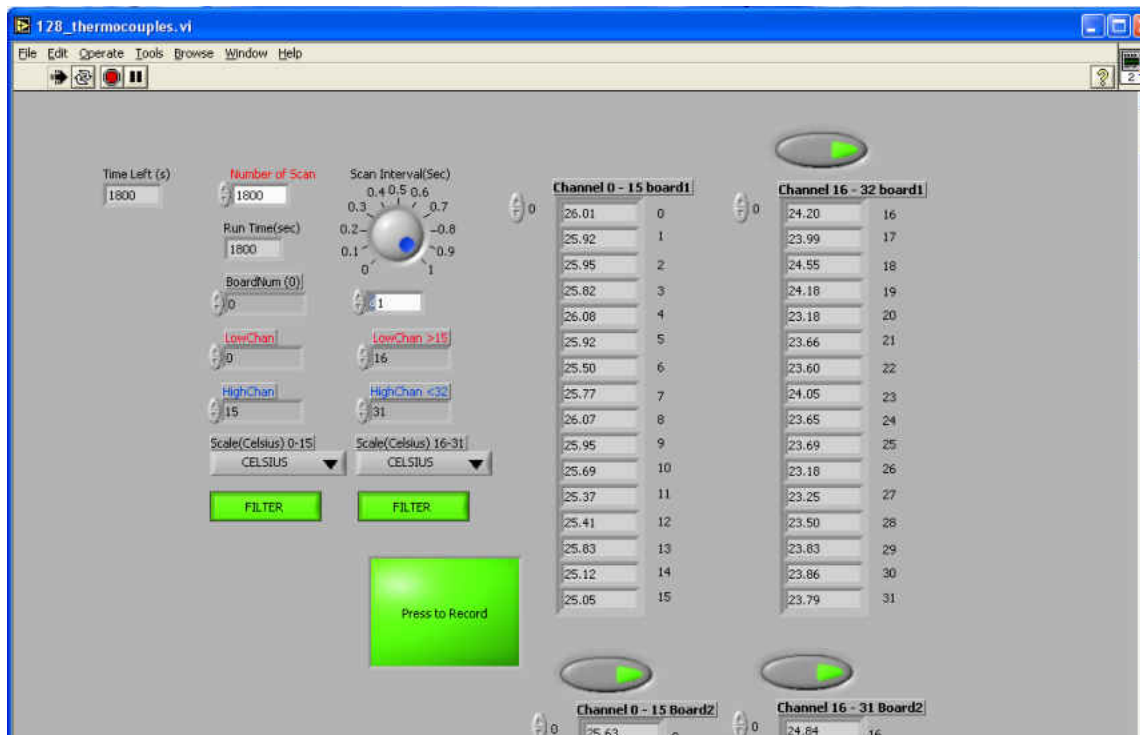


Figure 13: Labview user interface screen

Test Channel Geometry

Figure 14 shows the cross section of the (19:1) aspect ratio channel. Due to machining limitation, the channel has a circular end wall instead of a rectangular cross sectional shape. The test channel was composed of 9 different copper blocks with the following rib parameters: $P/W_r = 2.0$, $e/D_h = 0.0885$, $P/e = 18.8$, $L/D_h = 13.3$, $P/D_h = 1.67$, where D_h is defined as $(2W_c \cdot H / (H + W_c))$. The air flow is normal to the copper blocks and the ribs were oriented at an angle $\alpha = 90^\circ$. These rib parameters led to a 33 percent blockage ratio of the total channel cross sectional area.

A thin layer of polymer insulation was used to separate the copper blocks. To ensure a smooth transition across the insulation, the copper blocks and insulations were machined at the same time.

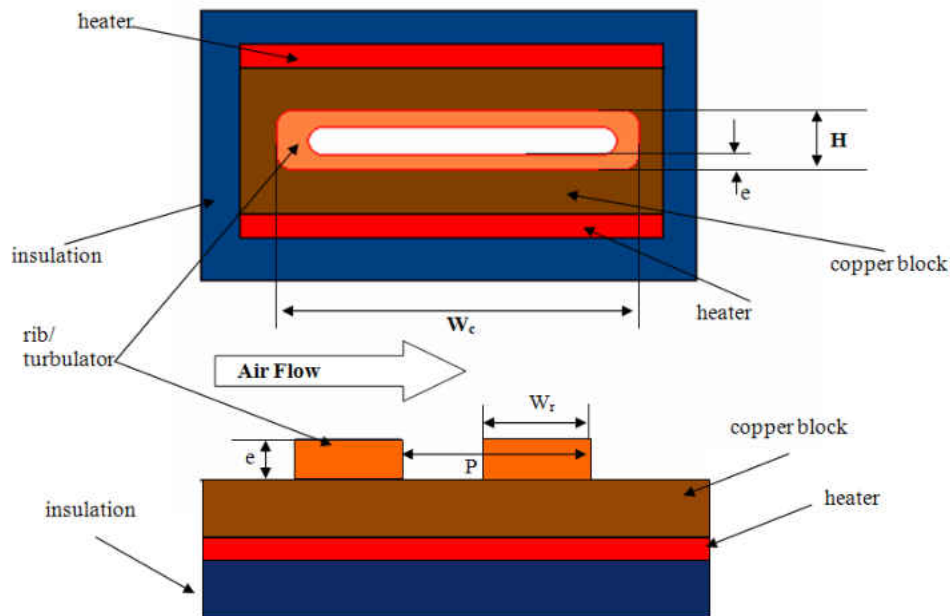


Figure 14 Cross-sectional view of the channel (top); Side view of the ribs in the main flow (bottom)

3.2 Split entrance effect, Configuration B

In typical laboratory conditions, a fully developed portion of the test rig is used to understand the flow structure and to ease calculations and/or develop mathematical correlations. This may not be the case for application in different machines. Frequently, fully developed conditions are not attainable in short channels used in these machines. To simulate a machine of interest, the second portion of this experiment uses a horizontal channel and a vertical test channel to test the overall entrance effect on the average heat transfer augmentation on the vertical channel. Figure 15 shows the overview of the final test section and instrumental locations.

Like the fully developed high aspect ratio used in section 3.1.1, the test section is the same as the previously mentioned. With the extra channel, a new blower is needed. The new blower was also made by Spencer, model VB-110, a 15 Horse power motor blower capable of forcing up to 300 cubic feet per minute of air at 100 inches of water pressure head. Figure 16 and Table 3 shows an example of the blower and its specification respectively. Venturi 1 and 2 were used for the horizontal channel only (refer to Table 2 for more details). Since the blower puts a very large amount of work into the flow, a heat exchanger is needed to keep the inlet temperature of the test section cooled. The heat exchanger was also piped in series with the blower and horizontal flow system. The heat exchanger uses tap water in an open loop to dissipate heat and keeps the inlet temperature of the test section at around 30°C.

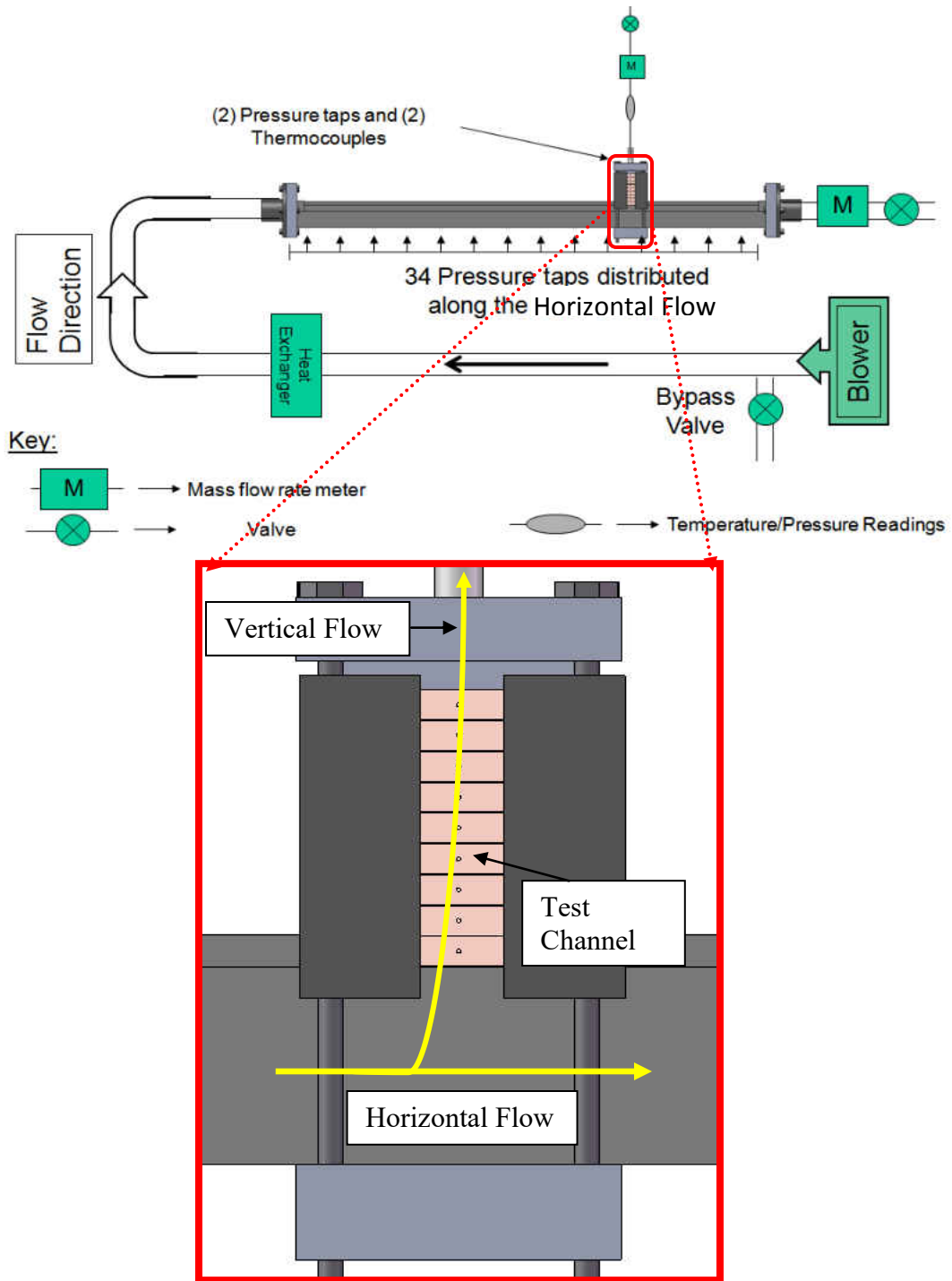


Figure 15: Overall setup of the Split entrance test channel, Configuration B



Figure 16: VB-110 Spencer blower

Table 3: VB-110 Spencer blower specifications

SPECIFICATIONS

Model No.	Freq	Maximum Volume		Maximum Operating Pressure		Maximum Operating Vacuum			Standard Voltage	FLA Current	Locked Rotor Current	Speed	Estimated Acoustical Noise Level	Weight	
		cfm	m ³ h	"H ₂ O	mbar	"H ₂ O	mbar	hp						Volts	Amperes
VB-110	60	645	1096	102	254.1	104	259.1	15	200-230/460,3Ø	40-37/18.5	250.4-288/144	3450	80dba@60Hz	370	168
	50	538	914.2	94	234.2	76	189.3	12.5	190/380-415,3Ø	37/18.5-18	276/138-126.4	2850		370	168

Maximum Ambient Temperature: 104°F/40°C. Maximum Internal Motor Temperature: 311°F/155°C.

Inlet temperatures were collected along the horizontal channel with four type T thermocouples protruding into the flow. The temperature readings obtained for all thermocouples were the same, within the uncertainty of the thermocouples. These four measurements were then averaged as the inlet temperature for the main test (vertical) channel.

To have a more detailed study of the inlet conditions, two horizontal channel sizes were tested to study the effects of the different cross-sectional area in the supply channel on the turning of the flow entering the test channel. Figure 17 shows the two horizontal channel cross-sections. Note that these dimensions are given in terms of the hydraulic diameter of the vertical test section. Due to privacy sensitive information, the exact dimensions cannot be given.

Table 4 summarizes the different cases ran for all high aspect ratio channel test sections.

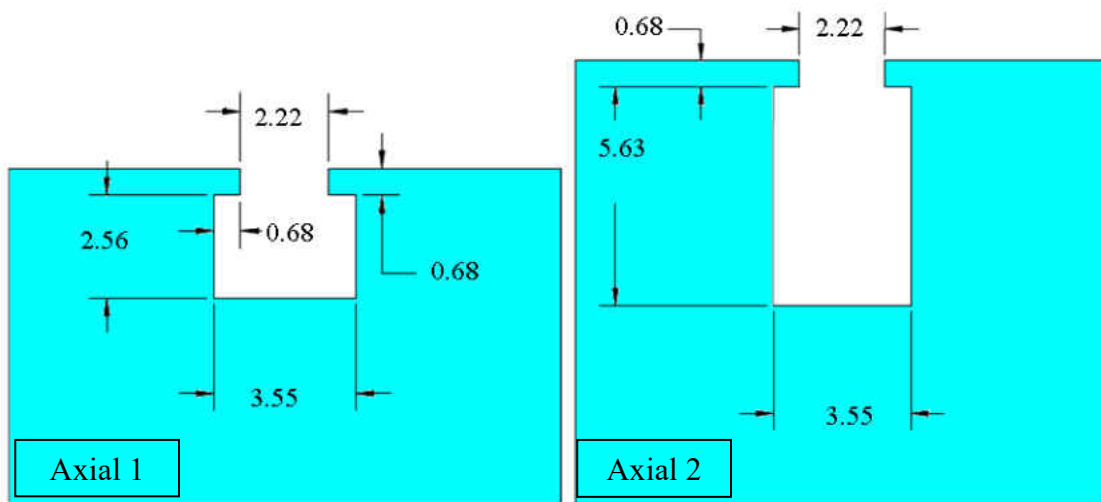


Figure 17: Different horizontal channel sizes (dimensions are given in term of vertical channel’s hydraulic diameter)

Table 4: Test conditions specifications

Configuration	Horizontal channel Configuration	Horizontal channel Reynolds number at the exit
A	None	None
B	1	20,000
B	2a	50,000
B	2b	100,000

Configuration A and B in Table 4 are referring to the fully developed high aspect ratio channel setup and the split entrance condition correspondingly. Horizontal channel 1 and 2 refers to the small or large horizontal channel depicted in Figure 17. The horizontal channel's Reynolds number at the exit refers to the actual Reynolds number that the horizontal channel depicts after the consideration of the flow extraction of the vertical channel.

To emphasize the sign convention and channel overview, Figure 18 reiterates the used sign convention. The Y is in the vertical direction referring to the vertical channel starting at the height of the horizontal channel and the X-direction is in the horizontal flow direction.

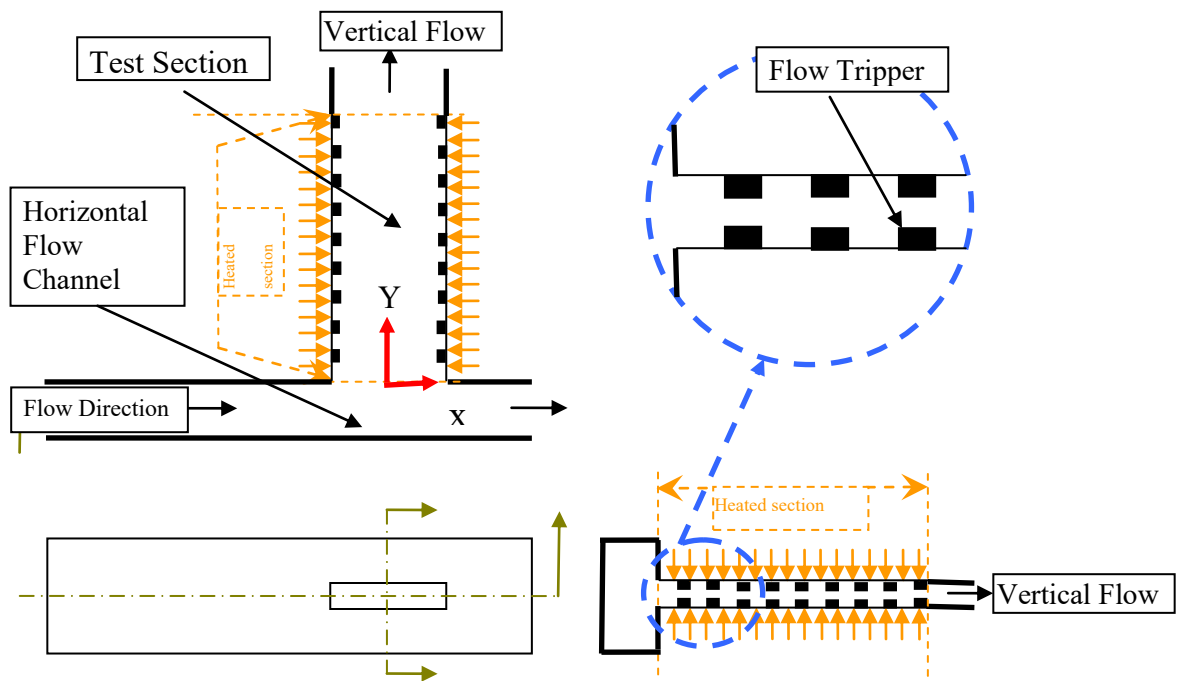


Figure 18: 2-D overview of the completed Configuration B setup

3.3 High aspect ratio channel data analysis

The sought after parameter for heat transfer experiments is the thermal performance factor (η) under constant pumping power (equation 12). The thermal performance is a quantity that describes the ratio of the amount of heat transfer that can occur to a given pressure drop. The best design is the one which maximizes the thermal performance.

Nusselts number (Nu) is the factor that describes the amount of heat transfer across the internal surface of the channel. The friction factor correlates to the pressure drop in the stream wised direction of the channel. The Nusselt number is directly related to heat transfer coefficient (h) which can be obtained by a number of measured parameters in the Heat Transfer Coefficient Calculation, section 3.3.2. Pressure drop through the channel is directly linked to the friction factor (f) and is determined in the Friction Factor Calculation, section 3.3.3.

3.3.1 Heat leakage and lateral conduction correction

Heat leakage tests were done for both configurations. To perform the heat leakage test, all valves and openings were closed or filled with insulation to eliminate the possibility of any convection currents in the channel. A constant amount of power was applied to meet the desired channel temperature, while maintaining an isothermal condition throughout all copper blocks and avoiding lateral conduction between the blocks. Three to five different temperature settings were tested and the collected data was fitted into a curve. From the tests were nine different equations—one for each block—relating leaked power to the temperature difference between the copper blocks and the ambient temperature (Power vs. $(T_w - T_{amb})$). Each equation found the

heat leakage for the respective copper block during data processing. It was discovered, in both cases, the maximum heat leakage was observed to be less than ten percent of the lowest power setting.

It was necessary to determine the amount of heat leakage to the horizontal channel by the bottommost copper block. To do so, a number of 4 to 5 different horizontal flow rates were ran to determine the amount of power needed to maintain all copper blocks at a given temperature. The first set of data was obtained by supplying a known flow rate in the horizontal channel and no flow through the vertical channel. The data of interest was the amount of power required to maintain the bottommost copper block at an actual testing temperature, two or three temperature settings were tested. Next, was an adjustment in the horizontal channel's flow rate and the same sets of temperature settings were ran. Again data was curve fitted, ultimately yielding a correlation for the flow rate versus power input and temperature for the bottommost copper block.

One of the advantages with Configuration B is that the exact thermal resistance between each copper block can be determined. By taking advantage of the horizontal flow, a large temperature gradient between the bottommost copper block and the next block is obtained (Figure 19). The horizontal channel was then subjected to a known flow rate which acts as a means to remove the heat from the bottommost (first) copper block while keeping all other surfaces insulated. The first copper block was then minimally powered and the rest were maintained at a constant temperature of 10 to 20 degree Centigrade above the first block. With the heat leakage completed before hand, the lateral conductions were calculated by employing a simple control volume analysis. The thermal contact resistance was determined using the known

lateral conduction; the temperature difference between the first and the second copper block, the thickness of the insulation, the surface area of contact between the blocks, and the heat removal by the horizontal channel all uses Fourier's Law of conductivity. Equation 5 shows the setup of all the measured parameter to obtain thermal conductivity (k), and algebraic manipulation is needed to isolate k.

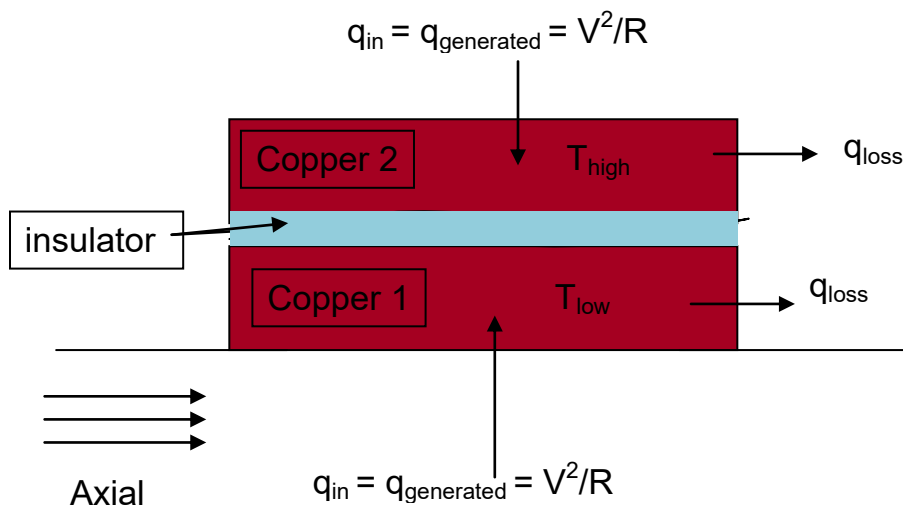


Figure 19: Contact resistance control volume

$$|q_{in} - q_{loss}|_{high} - |q_{in} - q_{loss}|_{low} = \frac{k_{ins} \cdot A \cdot |T_{high} - T_{low}|}{X} \quad (5)$$

3.3.2 Heat transfer coefficient calculation

For a copper block, the heat transfer coefficient (h) was calculated using the following equation:

$$h = \frac{Q_{in}}{A \cdot (T_w - T_b)} \quad (6)$$

where Q_{in} is the power input minus the power leaked to the ambient room condition due to the temperature gradient. A is the total projected wetted area, T_w and T_b –are the wall temperature and the fluid bulk temperature respectively. T_b was calculated with an energy balance at each Y location, based on the total power input, mass flow rate and the fluid’s specific heat capacity (equation 7).

$$T_b = T_{b-1} + \frac{Q_{in}}{\dot{m} \cdot C_p} \quad (7)$$

Now that h is known, we can non-dimensionalize all results with the aid of the Nusselt number (Nu) based on the hydraulic diameter, given by equation 8.

$$Nu = \frac{h \cdot D_h}{k_f} \quad (8)$$

In order to use the Nusselt number for heat transfer enhancement comparison, it is necessary to define a baseline. This baseline, Nu_0 is provided by the Dittus-Boelter correlation (equation 9) for internal flow of heating using the hydraulic diameter of the non-ribbed portion of the test channel.

$$Nu_0 = 0.023 \cdot Re^{0.8} \cdot Pr^{0.4} \quad (9)$$

The overall uncertainty for Nu/Nu_0 was determined to be less than 6.5 percent using the procedures proposed by Kline and Mc-Clintock [36]

3.3.3 Friction factor calculation

Friction factor was calculated based on the pressure drop and average velocity of the fluid through the copper channel as shown in equation 10.

$$f = \frac{\Delta P \cdot D_h}{0.5 \cdot L \cdot \rho \cdot V^2} \quad (10)$$

In this expression ρ is the density of the fluid and V is the velocity based on $\dot{m} = \rho \cdot V \cdot A_c$; and A_c is the cross section area perpendicular to the flow. f_o was determined using the Blasius correlation (equation 11) for Darcy Friction Factor for the Reynolds number range of less than 10^5 [37].

$$f_o = 0.316 \cdot Re^{-0.25} \quad (11)$$

The ratio (f/f_o) was reported in the result section. The overall uncertainty of the friction factor was determined to be less than 6 percent.

3.4 Results and discussion

This project was funded by Siemens Power Generation Inc. therefore detailed results and the channel's exact measurements are not publishable. In order for the publication to take place, everything has to be non-dimensionlized and the results are more useful from an academia point of view.

3.4.1 Heat transfer results

Configuration A

The following results were obtained after normalizing with the Dittus-Boelter correlation (Figure 20) for Configuration A.

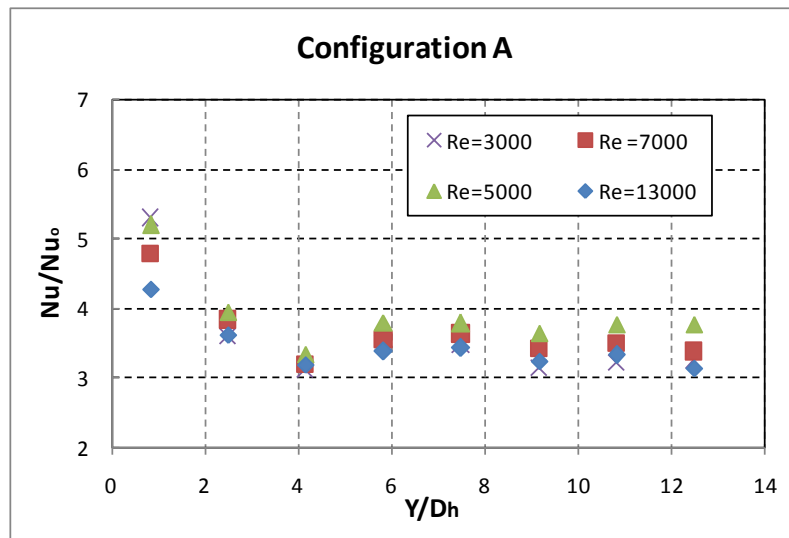


Figure 20: Configuration A results, normalized with Dittus –Boelter at different vertical channel Reynolds number

Since the entrance channel was not heated, as expected, the results in Figure 20 shows a higher Nu at the beginning of the test channel. This is due to the flow at the inlet being only hydrodynamically fully developed and not thermally fully developed. Based on the observed trend for the Nusselt number in this setup, the thermal boundary layer became fully developed after $Y = 5D_h$. This coincides with existing literature like Chandra et al [15]. Figure 20 also shows that the average heat transfer augmentation for the developed portion of the duct was around 3.5 times that of the Nu predicted by the Dittus-Boelter correlation.

Configuration B

The results for Configuration B are shown from Figure 21 through Figure 23. The flow settings for each of the different horizontal channels are shown in Table 4. The Reynolds numbers in the legend of each figure corresponds to the Reynolds number in the vertical channel, calculated with respect to the channel's hydraulic diameter in the non-ribbed cross section.

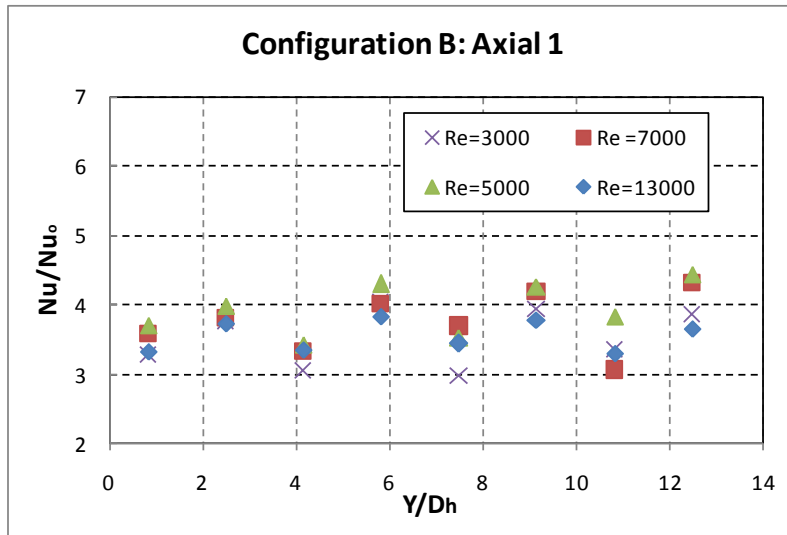


Figure 21: Configuration B, horizontal channel 1, Reynolds number of 20,000 at the exit of the horizontal channel

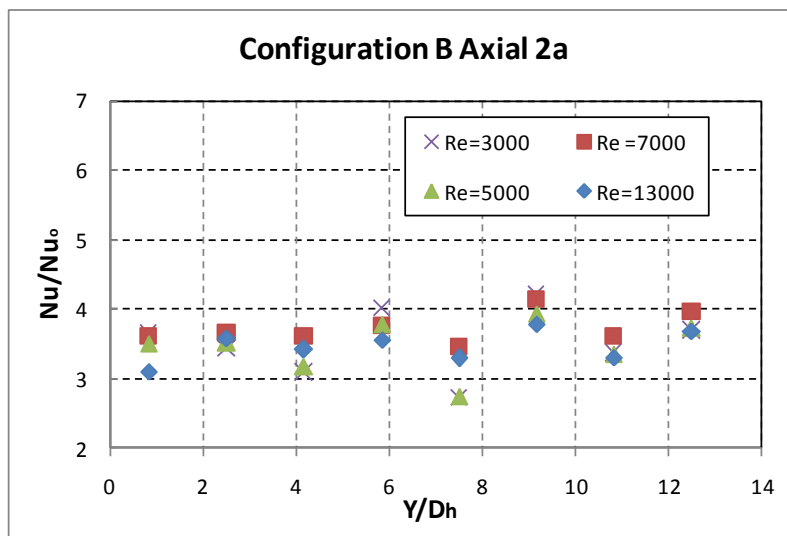


Figure 22: Configuration B, horizontal channel 2a, Reynolds number of 50,000 at the exit of the horizontal channel

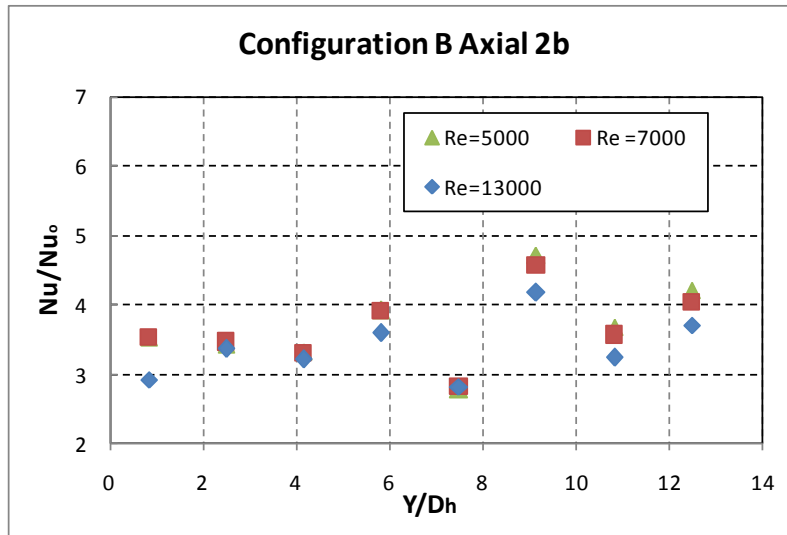


Figure 23: Configuration B, horizontal channel 2b, Reynolds number of 100,000 at the exit of the horizontal channel

The heat transfer augmentation trends of Configuration B in Figure 21 through Figure 23 are different from those in Configuration A. It is clearly shown that there is an oscillatory trend occurring for all cases ran with the added horizontal channel. To explain such a phenomenon, one can speculate that a recirculation zone occurred at the entrance of the vertical channel. Figure 24 was used to visually explain such a zone. The size and flow structure of the zone is only a speculation, so the actual flow might not follow such a pattern.

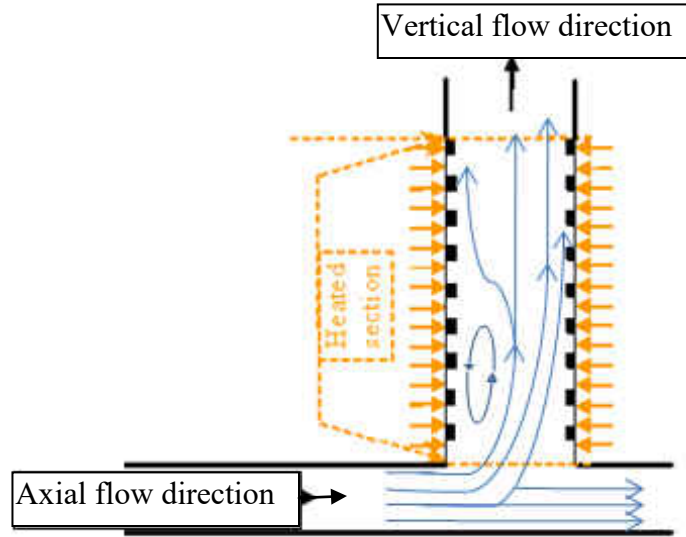


Figure 24: Speculated recirculation zone for Configuration B

The recirculation zone's size is affected by several linked factors within the horizontal channel including flow-rate in both the horizontal and vertical channel cross sectional area of the horizontal channel and the corresponding momentum of the fluids within each channel. These parameters thus affect the overall heat transfer trend throughout the vertical channel. The recirculation zone can extend as much as half ($7 D_h$) of the total length of the vertical channel, explaining the drop in Nu/Nu_0 at the location of $Y = 7D_h$ for high horizontal flow velocity and relatively low vertical velocity. The same effect can be seen clearly in Figure 23 for all vertical flow rates tested. These oscillations do not occur with the pure duct case since the flow is hydrodynamically fully developed before entering the vertical test channel.

It is important to note that all Nu/Nu_0 calculations from Figure 21 to Figure 23 were done with the assumption that none of the thermal energy input from the bottommost copper surface enters the main vertical channel, meaning that the amount of heat leakage from the bottom copper block for all horizontal flow rate is kept without any modification when testing both

horizontal and vertical flow. It is safe to say that some of the energy removed from the bottommost surface actually entered the vertical channel because the thermal boundary layer developed at the beginning of the copper block is directly within the path of the slot which enter the vertical channel. Figure 24 also shows this phenomenon from the streamline point of view. To have a good estimate of such a factor, a detailed Computational Fluid Dynamics (CFD) study at the mentioned location must be performed.

To consider the effects of the entrance condition on the entire vertical channel, the average Nu/Nu_0 from the second to the eighth copper block ($1.7 < Y/D < 13.3$) was plotted in Figure 25. The overall average heat transfer augmentation was not affected by the inlet condition. This may change if one were to consider the heat picked up by the flow before it enters the vertical channel. In addition, the size and flow rate of the horizontal channel is not essential in the overall average heat transfer coefficient. This may not be the case if one were to design turbine blades where uniform heat transfer coefficient values are required for minimizing thermal stress. A more detailed investigation on the rib size with advanced tools such as CFD or local temperature measurement may be required to determine the location or the extent of the recirculation zone in order to eliminate or reduce the size of the zone to significantly avoid the large Nu fluctuation.

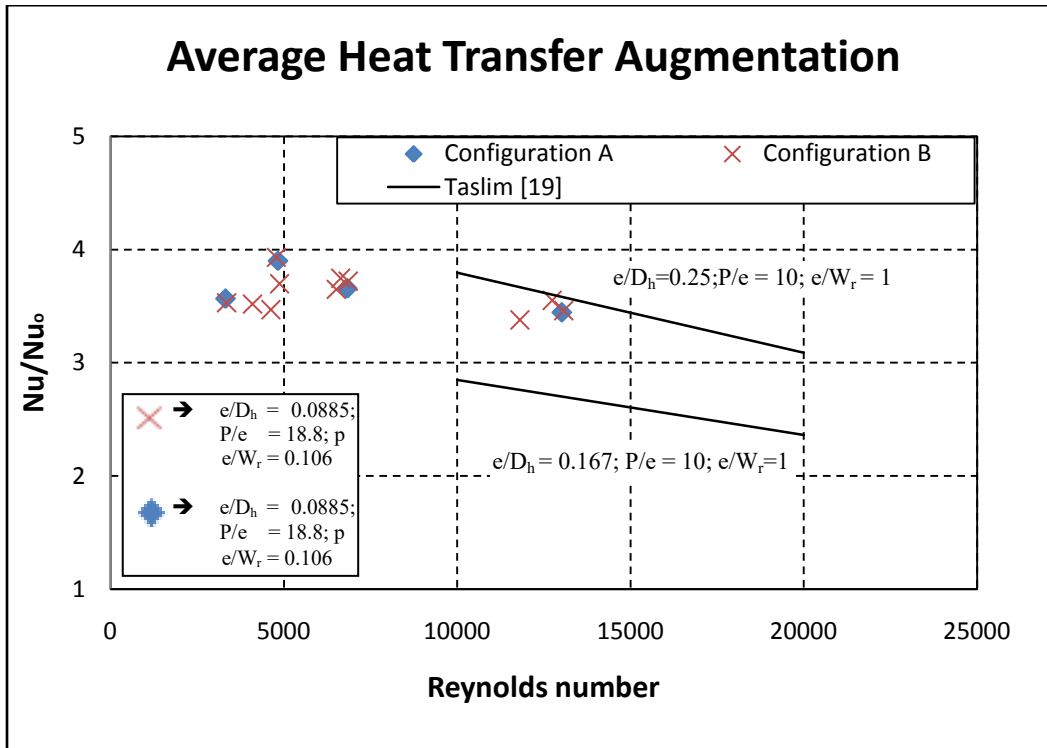


Figure 25: Summary of the average heat transfer coefficient for all cases vs. Reynolds number of the vertical channel

3.4.2 Pressure distribution

The pressure drop across the channel for each case was summarized in terms of the friction factor vs. Reynolds number (Figure 26).

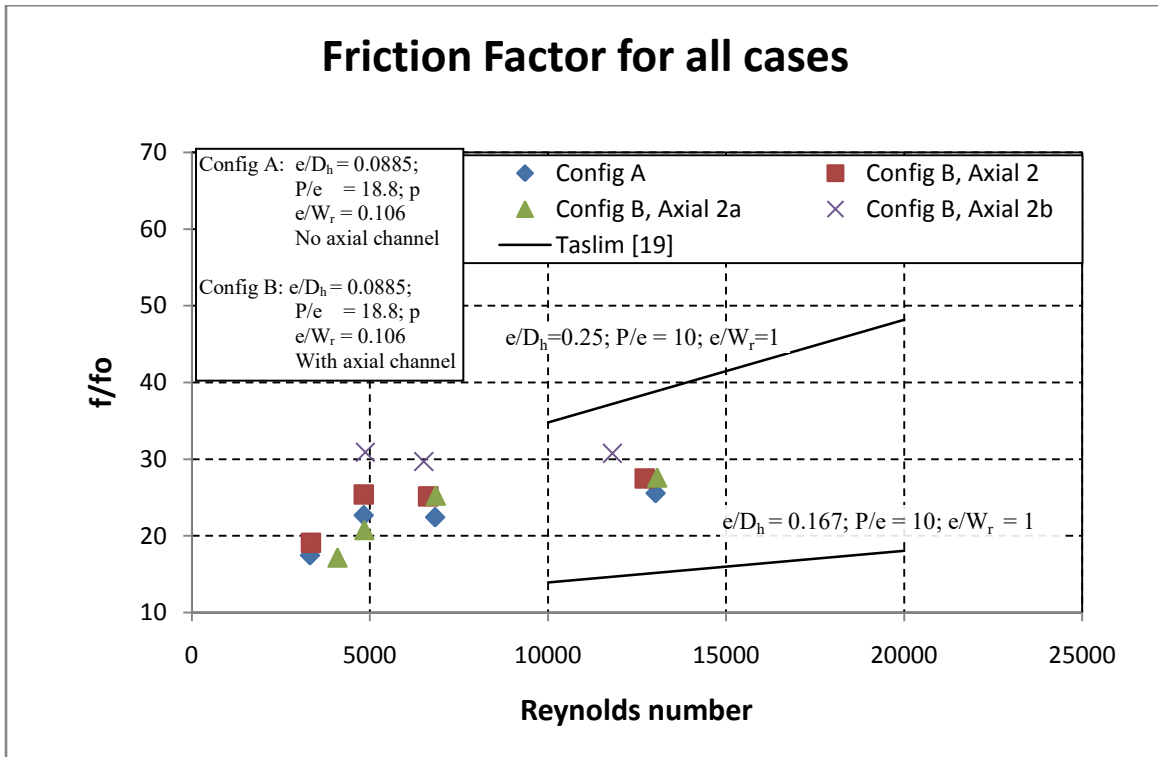


Figure 26: Friction factor vs. Reynolds number for all cases

The friction factor obtained from the current channel exceeds most of the data from Han, Chandra, Zhang and Liou. This is due to the high blockage ratio and the extremely high aspect ratio of the channel being tested. Also, with identical P/e , blockage ratio, and e/D_h ; for a given increase in aspect ratio, the friction factor increases greatly without a significant increase in heat transfer augmentation.

The smooth wall case for this channel was never ran, therefore the rig cannot be validated against well known correlations like Dittus-Boelter and Blassius equations, due to the nature of the work and the confidentiality with Siemens. The results were compared to the existing data summarized by Ligrani [35] and with the comparable blockage ratio performed by Taslim [19].

Figure 25 and Figure 26 contains a summary of the heat transfer augmentation ratio and friction factor augmentation ratio as a function of the vertical channel's Reynolds number along with data taken from Taslim [19]. These are two figures show both the data from the current test section. Two different blockage ratio parameters were chosen by Taslim for his tests. Taslim uses the channel blockage ratio of $e/D_h = 0.25$ and $e/D_h = 0.167$ for a channel with $P/e = 10$ and $AR = 1$ with only two staggered rib walls. These blockage ratios are comparable with the current test setup and the results are similar to each other. The heat transfer augmentation presented by [19] is within the same order of the augmentation received from the current test, as shown in Figure 25. The friction factor augmentation on the other hand, falls within the two limits set by Taslim. This is due to the arrangement of the rib performed by Taslim, his $e/D_h = 0.25$ provided a 25% blockage ratio from the start.

Figure 7 from Ligrani et al. [35] provides an overview of the results obtained from different authors. At a glance, the collected data falls within the range available sources, Figure 27 re-emphasizes the data from this configuration with the existing data set provided by Ligrani.

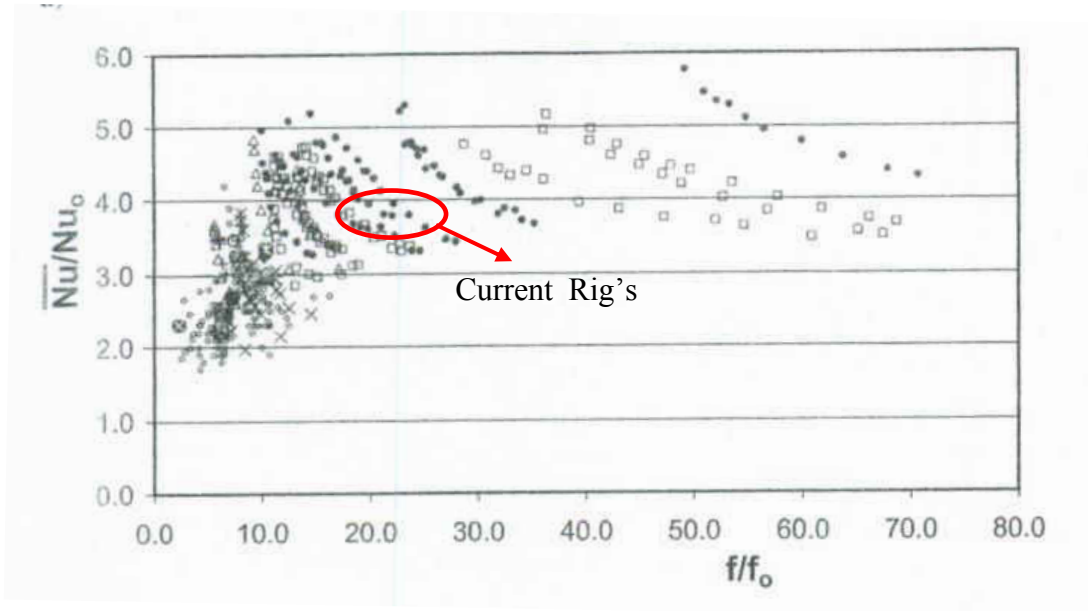


Figure 27: Friction factor augmentation vs. h augmentation data taken from Ligrani et al. [35]

In order to evaluate the effectiveness of a design, thermal performance factor is considered. Equation 12 determines the factors involved in calculating the thermal performance. Thermal performance is a function of both heat transfer and friction factor and how they compare to the smooth wall cases. Equation 12 characterizes the thermal performance factor at constant pumping power.

$$\eta = \frac{Nu/Nu_0}{(f/f_0)^{1/3}} \quad (12)$$

Thermal performance calculated for this rig using equation 12 is graphed on Figure 28. The values Taslim [19] obtained are graphed in Figure 29. Similar thermal performances reported from Taslim are similar with the current setup. It appears that the highest blockage ratio from Taslim ($e/D_h = 0.25$) has a similar thermal performance factor like the current test section. The small variation between the two is because of the different channel aspect ratio, rib parameters, and blockage ratio used.

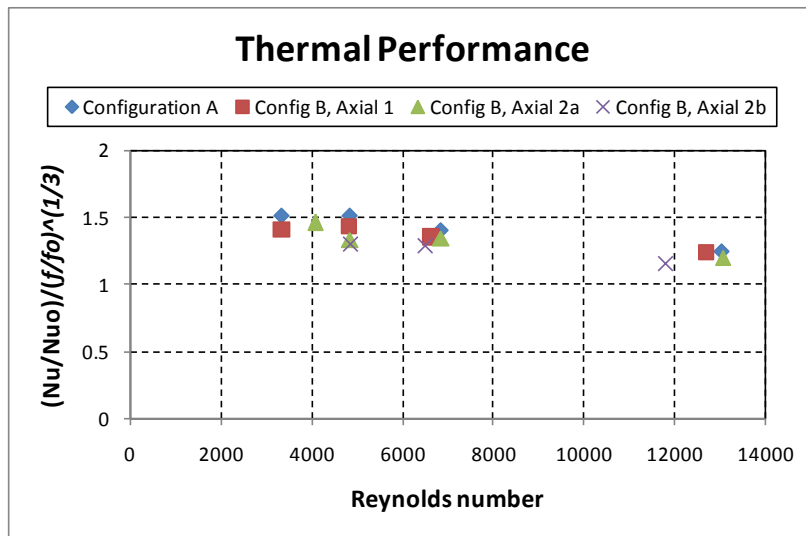


Figure 28: Thermal efficiency of all cases versus Reynolds number

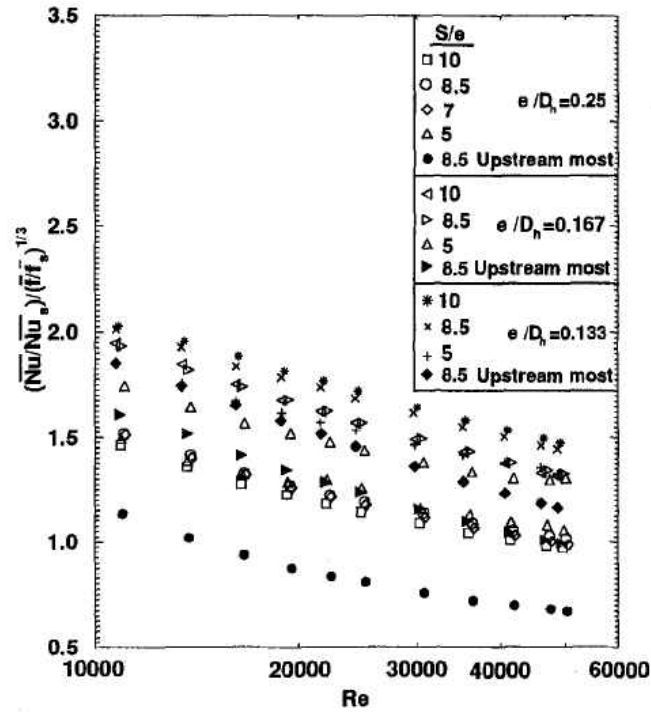


Figure 29: Thermal performance taken from Taslim [19]

Although the channel average thermal performance, friction factor, and heat transfer augmentation is similar between the current setup and existing works, more detailed study is needed at the split portion of the channel to determine the exact flow structure and the circulation zone due to the horizontal flow. Computational Fluid Dynamics (CFD) is one of the tools available to model this complex flow. Local data measurements like thermochromatic liquid crystal or laser interferometer may be used to collect detailed data needed to precisely determine the extent of the re-circulation zone.

Different test configurations are needed to decide the exact amount of energy picked up by the bottom surface entering the vertical channel. This was mentioned in section 3.4 under Configuration B. With the correct fraction of energy picked up from the bottom surface entering

the vertical channel, the heat transfer augmentation in each copper block will increase due to the smaller temperature gradient between the calculated bulk temperature and the copper walls.

CHAPTER 4: EFFECT OF VARYING RIB WIDTH

To have a better understanding of the effect of rib width on the overall heat transfer and friction factor augmentation in an internal flow channel, a new rig was built and tested without ties to Siemens, meaning publication is allowed. The new rig has two associated aspect ratios, 1:4 and 1:8 Height to Width ($H:W_c$) aspect ratio. The rib parameters are $W_r/P = 0.1, 0.3$ and 0.5 , refer to Figure 31 for more details on the current configuration setup, and the W_r/P relative in size can be viewed in Figure 5. Table 5 lists the total cases ran for this rig, each configuration has three different corresponding Reynolds number flow conditions; having a total of 21 separate complete tests in addition to the smooth wall cases for each channel aspect ratio.

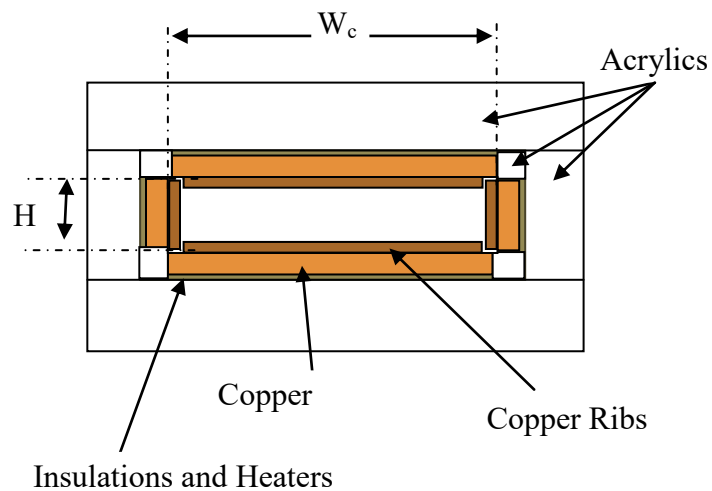


Figure 30: Cross section of the varying width channel

Table 5: Rib width test runs

Case #	W_c (in)	H (in)	e (in)	W_r (in)	P (in)	W_r/P	e/D_h
1	4.0	1.0	0.2	0.2	2.0	0.1	0.125
2	4.0	1.0	0.2	0.6	2.0	0.3	0.125
3	4.0	1.0	0.2	1.0	2.0	0.5	0.125
4	8.0	1.0	0.2	0.2	2.0	0.1	0.1125
5	8.0	1.0	0.2	0.6	2.0	0.3	0.1125
6a	8.0	1.0	0.2	1.0	2.0	0.5	0.1125
6b	8.0	1.0	0.2	1.0	2.0	0.5	0.1125

4.1 Channel setup

Figure 31 illustrates the overview of the setup for the new test section. The same equipments are used for this setup as the previous experiment; however, Kapton foil heaters from EGC Inc. were used instead of the Watlow Rubber Silicone heaters. With the new heaters, a new way to power them was needed. Since the new heaters have a lower resistance than Watlow's, it was more convenient to wire them in series instead of parallel.

The same VB-110 blower from Spencer Inc. was installed and operated under suction mode to draw in ambient room temperature air through the test channel; composing of an entrance length, a test section, and an exit section. The entrance and the test section are 20 inches long and the exit section is 8 inches long, equivalent to almost $12 D_h$ and $5 D_h$ respectively. Venturi 2, PVBRFAAA2C with a throat size of 2" 20 was used for all flow rate tested. A gate valve was connected in series with the blower and the venturi to control the flow rate for each test.

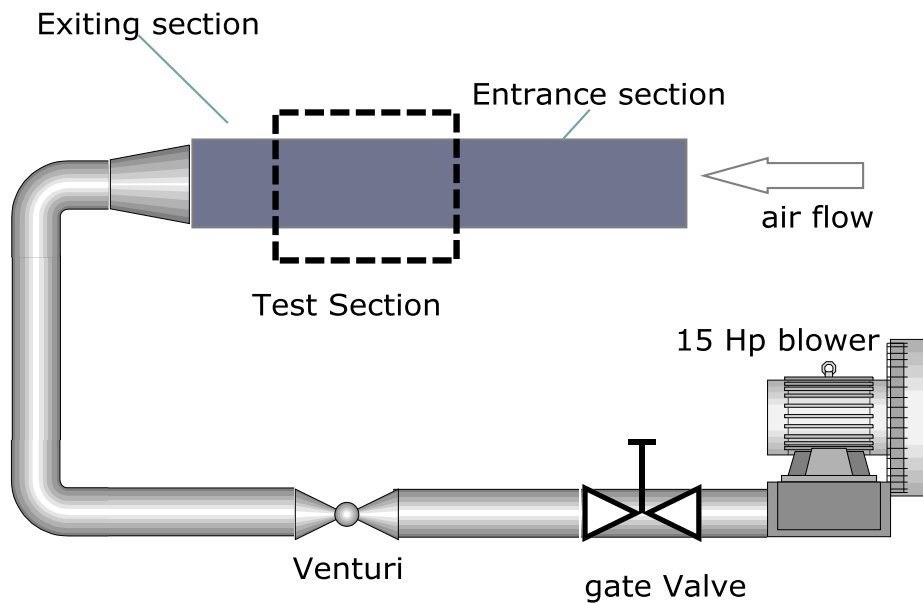


Figure 31: Varying rib width channel setup overview

The basic setup of this channel is akin to the previous test section; the only difference is that this channel has four independently controllable walls instead of a single copper block like the previous test section. Figure 30 shows the basic cross-sectional view of the new rig. Copper was mounted to all four walls using epoxy and cork. To ensure that a smooth transition from one copper block to the next is maintained, single sided Kapton tape was used to connect one block to another.

The actual completed test section is represented in Figure 32. Each individual wall contains full arrays of ribs which can be seen from Figure 33 to Figure 35. Figure 35 shows a close-up of the rib settings, it contains three different increments of rib width sizes. The first from the right is the $W_r/P = 0.1$, then adding the next rib segment increases the rib size to $W_r/P = 0.3$ and the final length creates a rib size of $W_r/P = 0.5$.

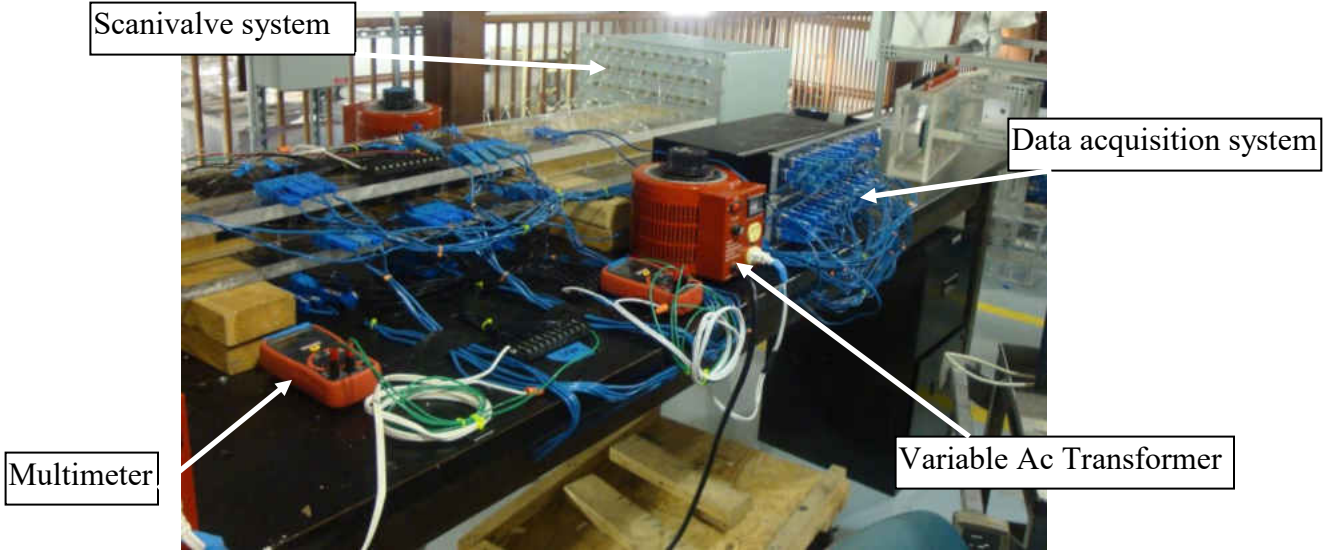


Figure 32: Completed rig assembly

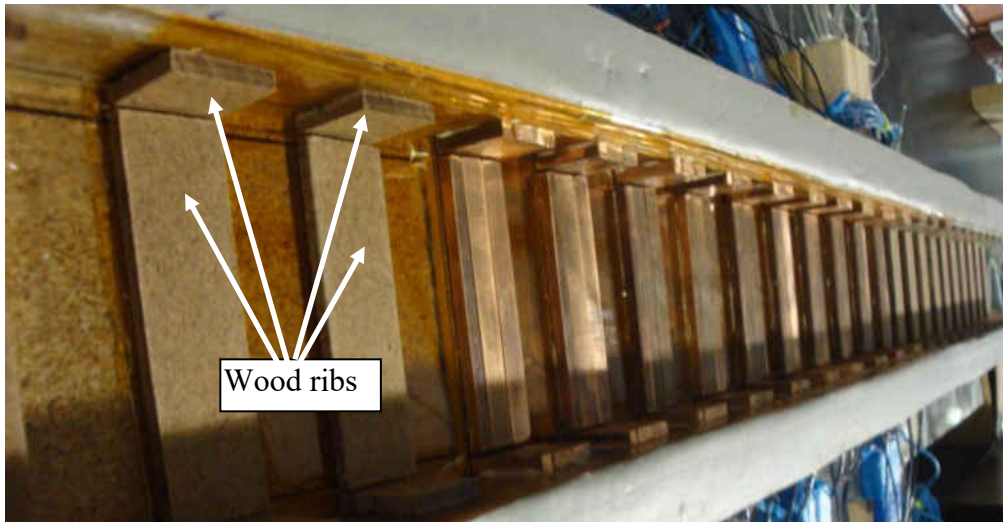


Figure 33: 1:4 Aspect ratio channel



Figure 34: 1: 8 Aspect ratio channel



Figure 35: Ribs close-up

To guarantee that the added rib segment does not create any extra mixing on top of the rib surface, case 6a was repeated to include a thin layer of aluminum tape attached to all of the

rib surfaces. This ensures that the top surface is smooth and flow does not trip because of the rib's surface features. The rib taped channel can be seen in Figure 36. This also made sure that the results from this rig are repeatable and can be trusted that the added rib width is considered as a single full size copper trip strip.



Figure 36: Case 6 repeated with taped rib surface

The test section is composed of nominal $\frac{3}{4}$ inches thick acrylic plates with cork insulation glued between the heaters and the acrylic's backing. The heaters contain adhesive to adhere to the copper plates and the ribs are glued on with high conductive thermal adhesive paste.

The entire test section is composed of 10 sets of four walled blocks of copper. As shown in Figure 33 to Figure 35, each wall contains its own copper plates, ribs, and heaters. Power is supplied through the use of four different variable AC current transformers. The heaters were arranged in series with a voltmeter to collect current, and the voltage was collected through the use of a highly accurate Keithley multimeter (Figure 37).



Figure 37: Keithley multimeter

4.2 Results and discussion

Like the previous test section, heat leakage tests were required in order to accurately process the final heat transfer data. To perform the heat leakage tests, the entire channel was filled with micro fiber glass type insulation to eliminate all possible internal convection currents. The entire test section was heated until thermal equilibrium was achieved. This takes approximately 12 hours for one temporal setting. Voltage, current, and ambient temperature was recorded along the process. Three of these cases were performed for each channel. Data was

then curve fitted with heat leakage as a function of the temperature gradient of the individual copper block with the ambient temperature.

Lateral conduction was also considered with the cork's thermal conductivity provided by the manufacturer and the measureable thickness which separated from one copper block to another. The exact thermal conductivity cannot be determined because in this case a large thermal gradient between any two consecutive copper blocks cannot be achieved like in the previous test section, configuration B. Energy balance was performed from one copper block to the next to find the lateral heat leakage; the same equation can be applied here like in the past experiment, equation 5.

The basic heat transfer and friction factor augmentation equations and thermal performance factor used in this channel is also similar to the previous channel rig from section 3.2 to 3.3.3.

4.2.1 Baseline configuration, smooth channel

Both aspect ratio channels were validated using the smooth wall correlation proposed by Dittus-Boelter. Figure 38 shows Nusselt number ratio results for the (1:4), (W:H), aspect ratio channel and Figure 39 reported the Nusselt number ratio for the (1:8), (W:H), aspect ratio channel. For the lower aspect ratio channel (1:4), the results obtained from the validation tests ended up to be very similar to that of Dittus-Boelter's. This is to show that the hydraulic diameter equivalent can be applied to the (1:4) channel.

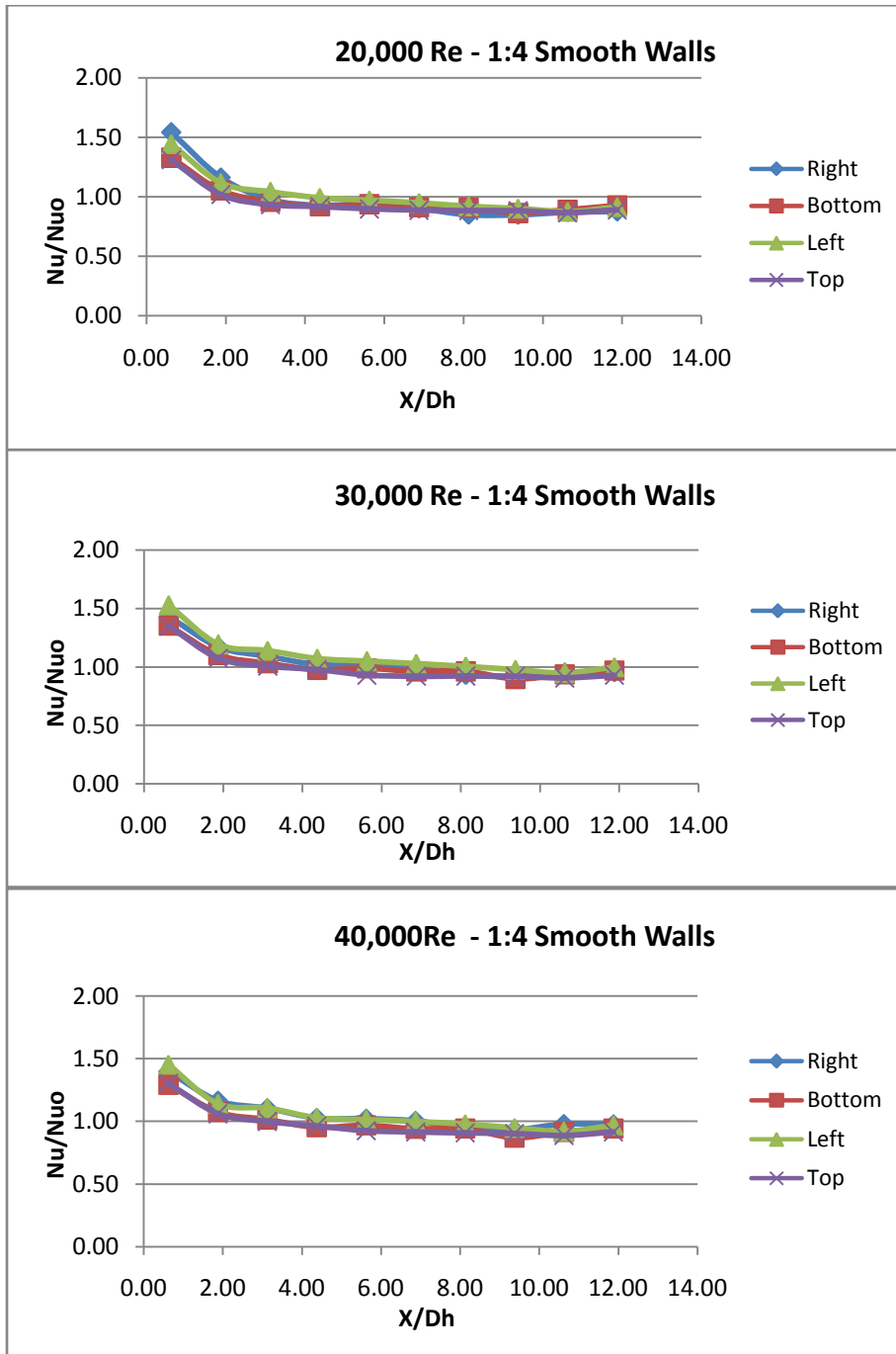


Figure 38: Smooth wall for 1:4 aspect ratio channel

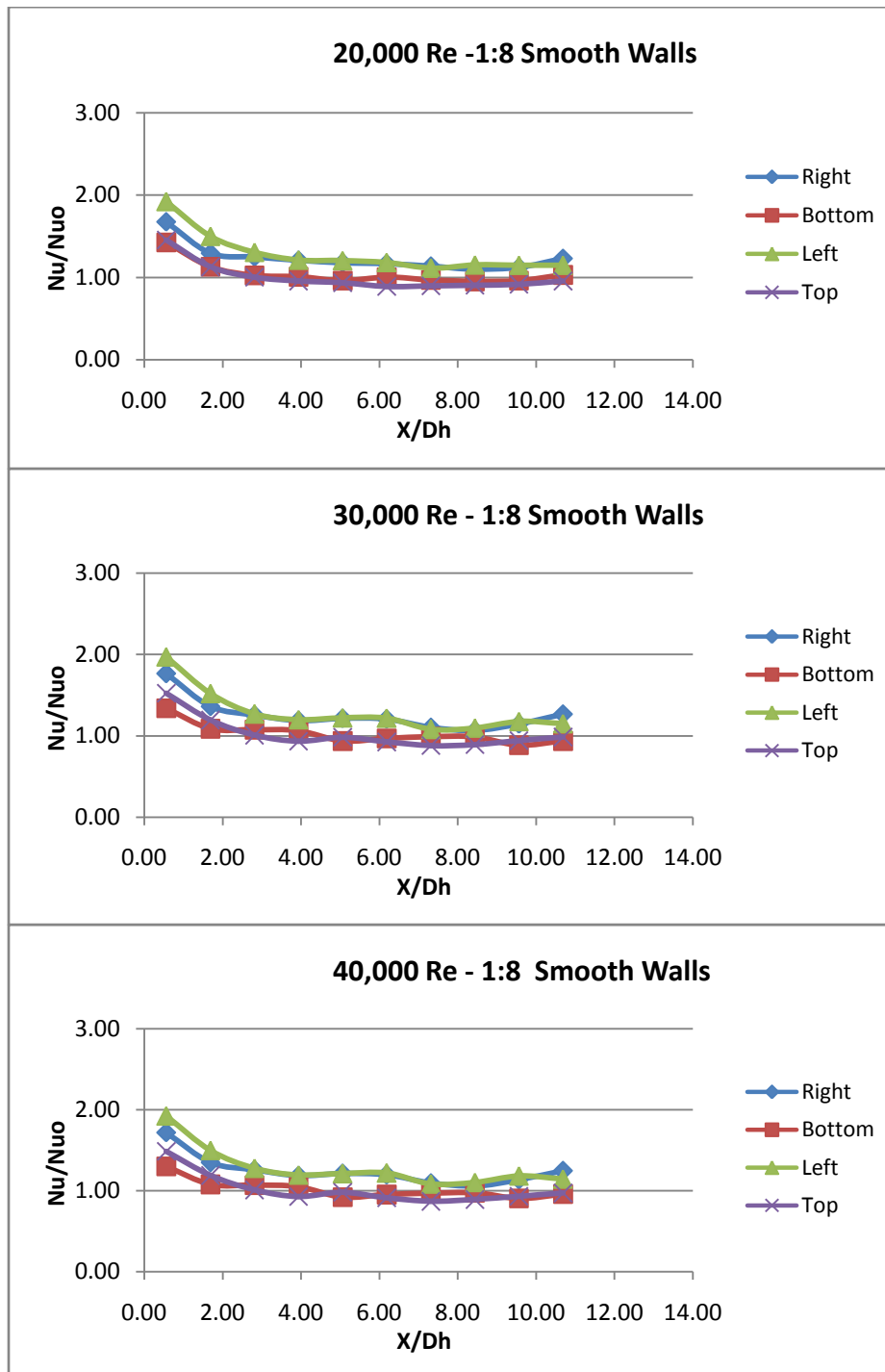


Figure 39: Smooth wall for 1:8 aspect ratio channel

Figure 39 shows that the smooth walls for the (1:8) aspect ratio does not behave like the (1:4) aspect ratio channel with no augmentation ($Nu/Nu_o = 1$). It appears that the two sided walls for the (1:8) channel always has a higher heat transfer coefficient than the top and bottom walls for the smooth wall cases. Figure 40 provides the Nusselt number ratio for the area weighted average for the three Reynolds number belonging to the (1:8) aspect ratio channel. The results shows that individually the heat transfer coefficient on the smaller side walls has an enhanced h , but average wise, the overall channel has a Nusselt ratio that is the same as Dittus-Boelter correlation.

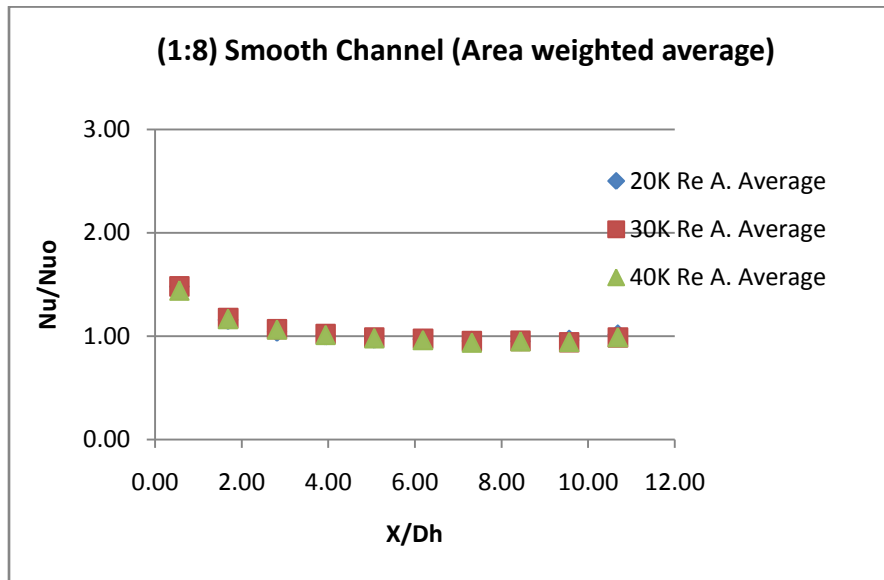


Figure 40: Area weighted average for the smooth channel of 1:8 aspect ratio

The augmentation of the side wall can be explained using isovel's characteristics of the large aspect ratio. Figure 41a and Figure 41b was taken from the Single Phase Heat Transfer Hand-book [29] providing some insight to the side wall enhancement of h . Figure 41a presents

the isovels in a rectangular channel. These isovels causes asymmetry to the flow structure, thus causing secondary flow to occur, as seen in Figure 41b.

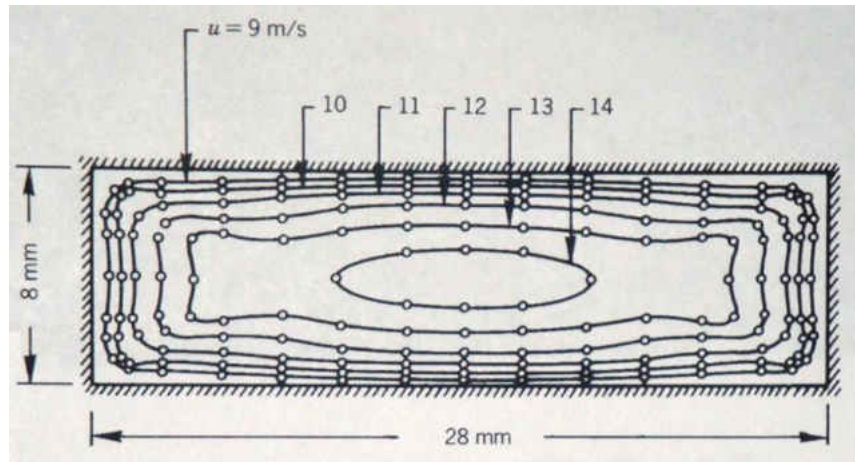


Figure 41a: Isovells from a (2:7) aspect ratio channel, Single Phase Heat Transfer Hand

Book [29]

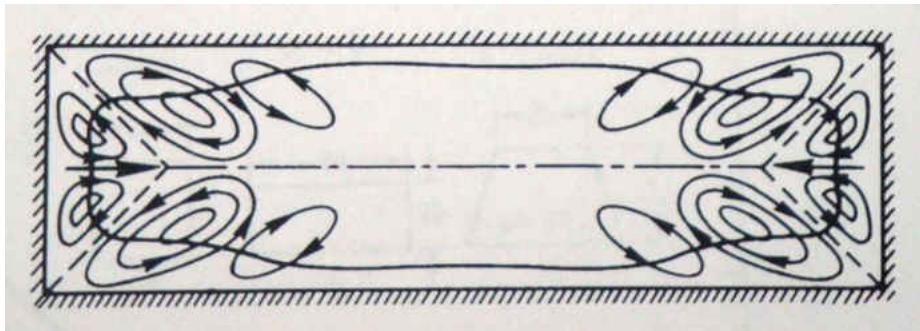


Figure 41b:: Secondary flow generate from Isovells, Single Phase Heat Transfer Hand

Book [29]

Notice that the large secondary only flow occurs around the side wall in Figure 41b. These secondary flows will create local mixing, enhancing the heat transfer rate only to the side walls. This explains the result from the smooth wall case when the side walls constantly has a higher h than the top and bottom walls.

4.2.2 Heat transfer results

A total of 21 cases were ran, three Reynolds number for each rib size of each channel aspect ratio. Instead of showing the actual heat transfer coefficient, it is easier to see the level of augmentation if the data was reported in term of Nusselt number ratio. The Nu_0 is the baseline Nusselt number calculated based on Dittus-Boelter's correlation for a circular duct using the non-ribbed portion of the equivalent hydraulic diameter. The full set of data is as follow: Figure 42 to Figure 44 corresponds to the 1st channel (1:4) aspect ratio; the uncertainty bars for each Reynolds number were graphed, an example of the uncertainty calculation is available in the APPENDIX. The same method [36] of calculating uncertainties in the previous test rig was employed here as well. The level of uncertainty obtained for this rig was around $\pm 10\%$ for the worst case pertaining to the heat transfer tests.

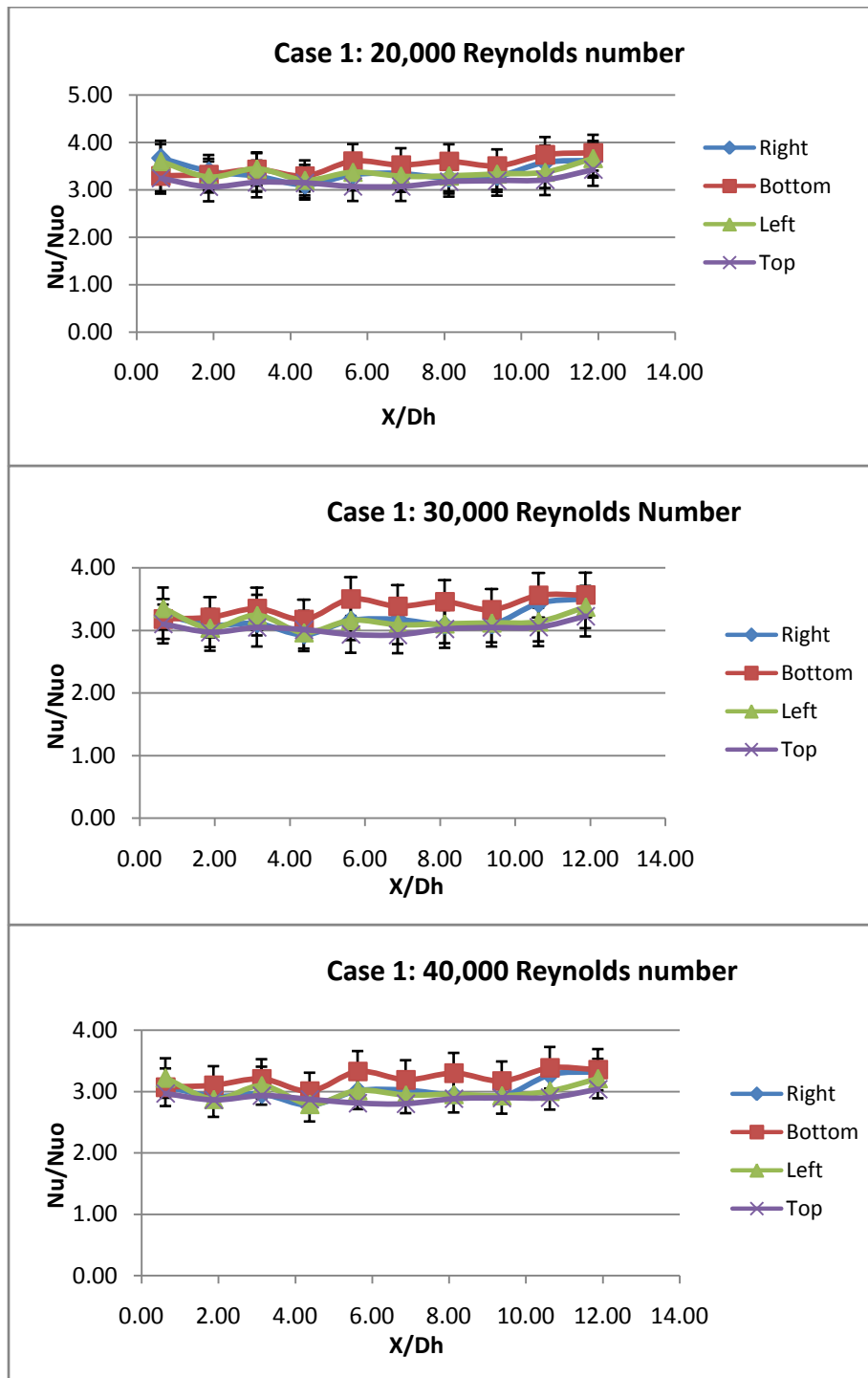


Figure 42: Case 1, all walls heat transfer augmentation

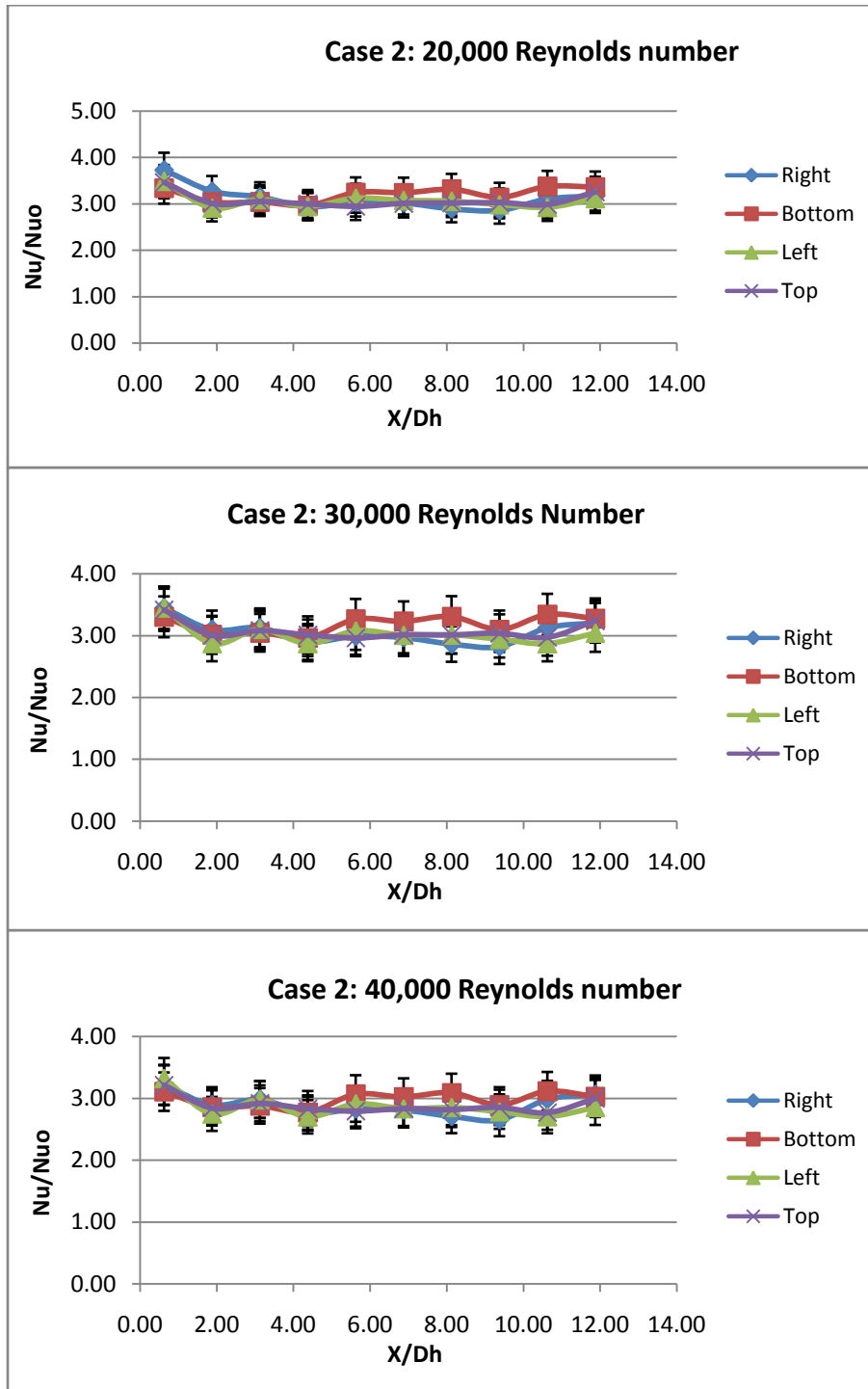


Figure 43: Case 2, all walls heat transfer augmentation

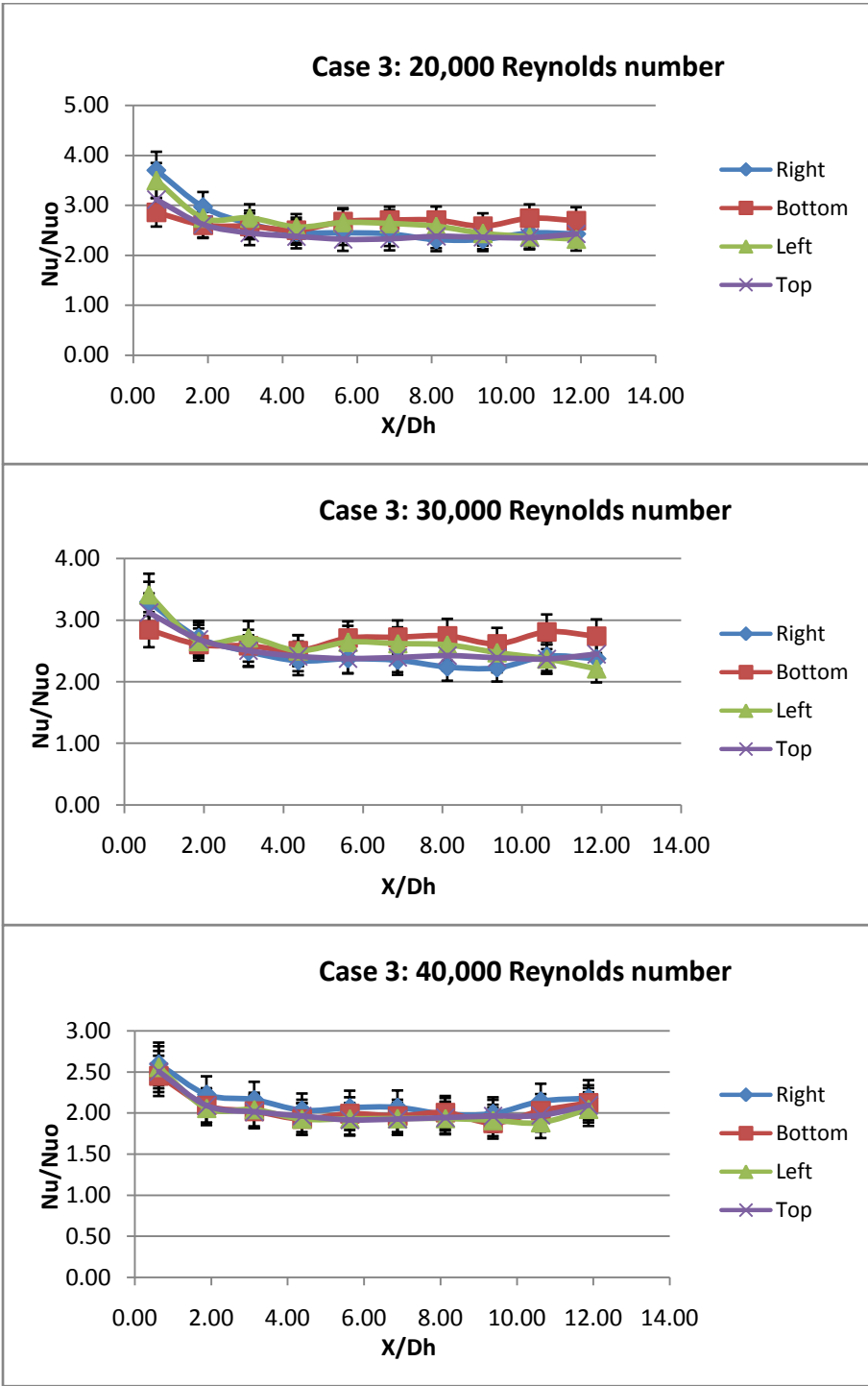


Figure 44: Case 3, all walls heat transfer augmentation

In all cases from the (1:4) aspect ratio channel, the bottom walls seems to have the largest heat transfer augmentation, but the uncertainty band for all walls overlap each other, therefore it is accurate to assume that the augmentation for all walls are similar.

Figure 45 is a summary of all cases ran with the (1:4) channel, it shows the area weighted average of the four walls per case per Reynolds number. Case1 provided the highest heat transfer augmentation; this corresponds closely with the literature stating that $P/e=10$ gave the highest heat transfer augmentation for square ribs, which were immensely tested. In this case, the heat transfer augmentation was highest with the square rib attachments, and the degree of augmentation decreases as the Reynolds number and the rib's width increases.

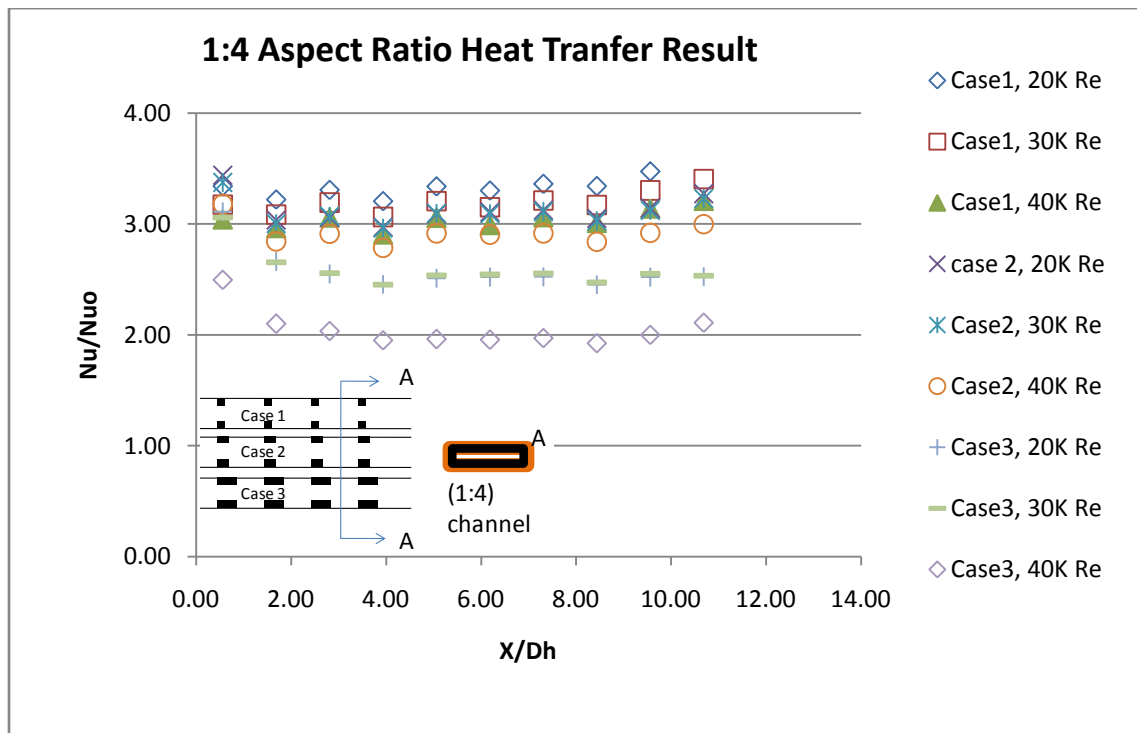


Figure 45: Summary of all cases ran for 1:4 aspect ratio channel

Figure 46 to Figure 50 are the results obtained from the (1:8) aspect ratio channel.

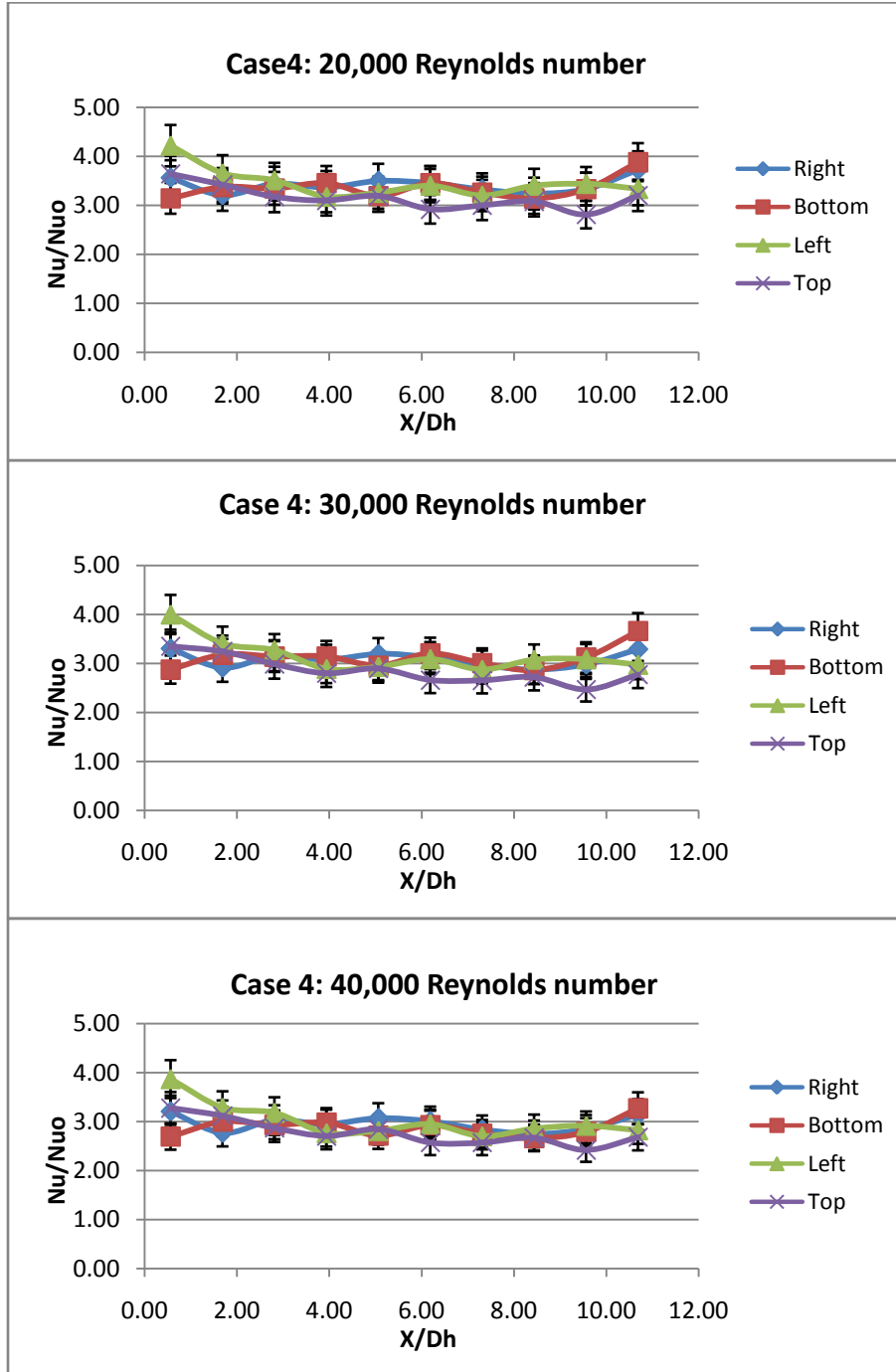


Figure 46: Case 4, all walls heat transfer augmentation

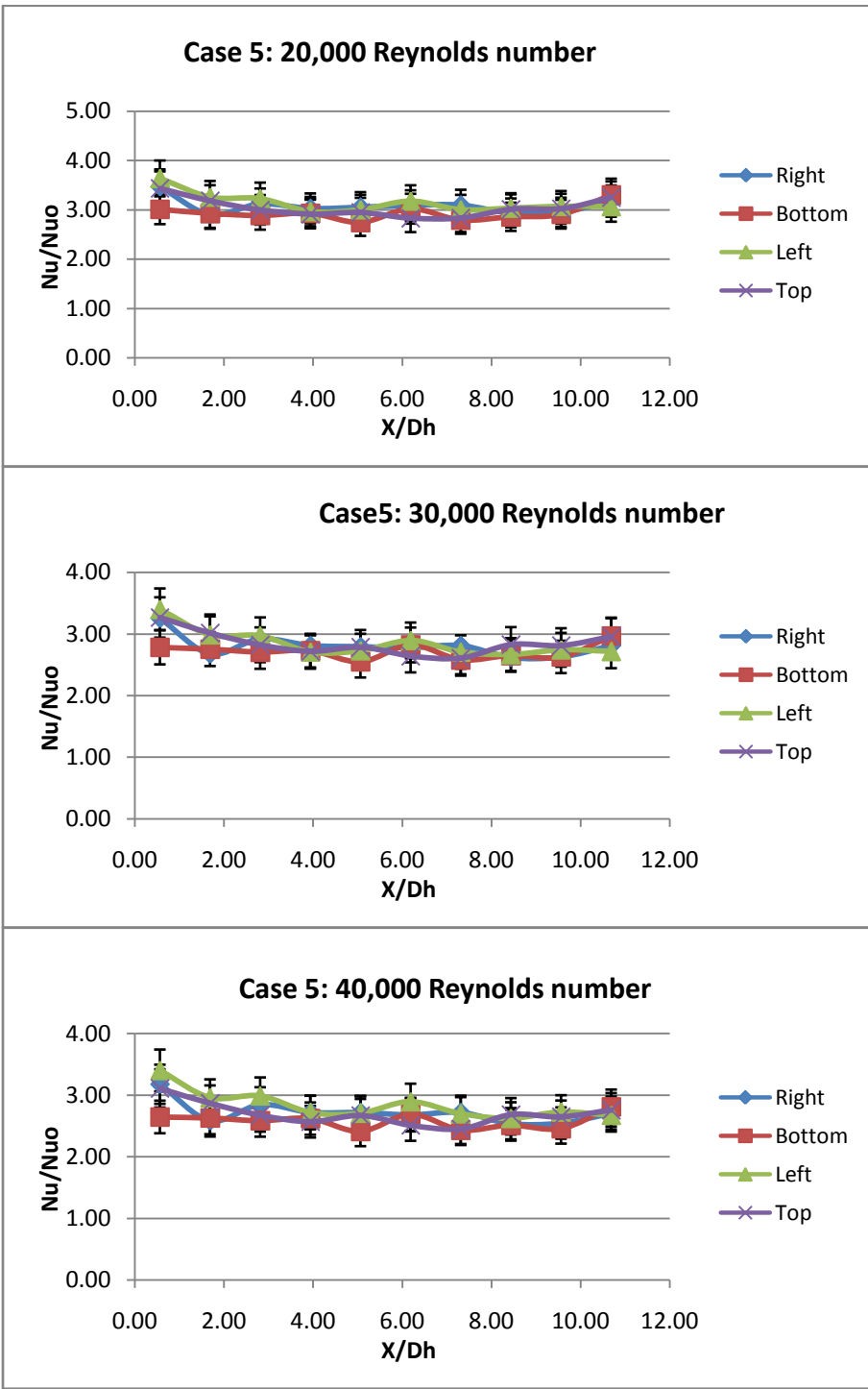


Figure 47: Case5, all walls heat transfer augmentation

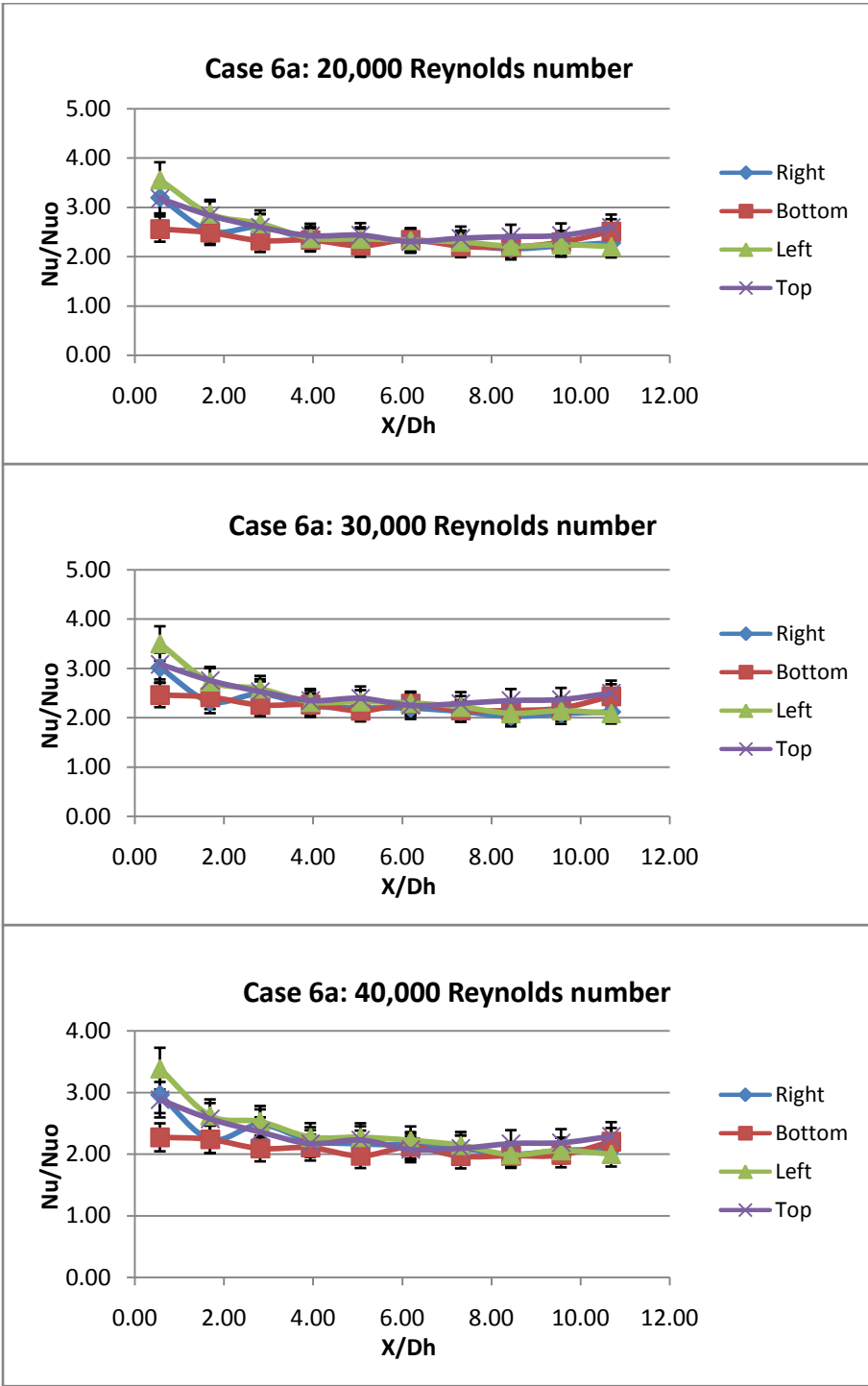


Figure 48: Case 6a, all walls heat transfer augmentation

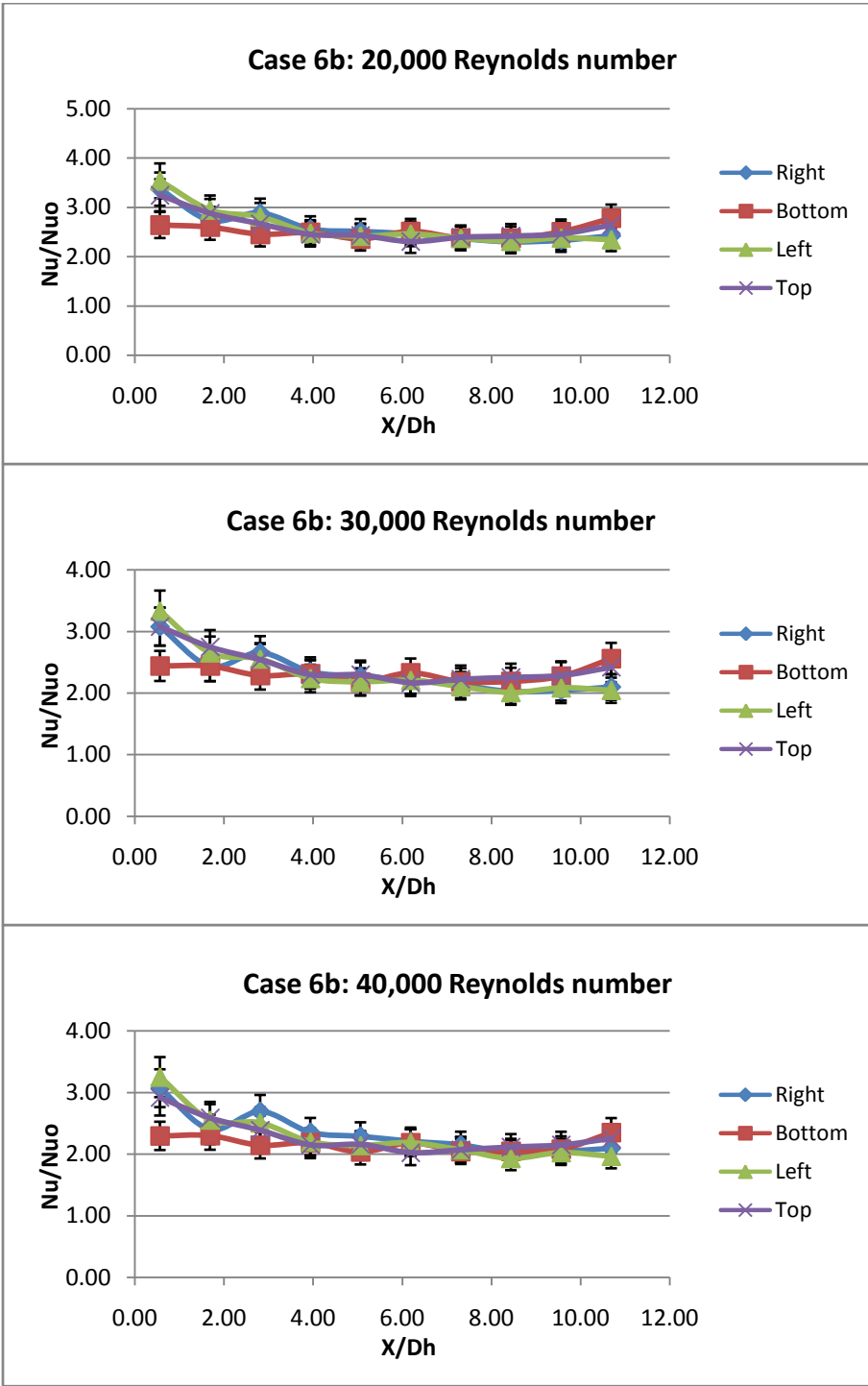


Figure 49: Case 6b, all walls heat transfer augmentation

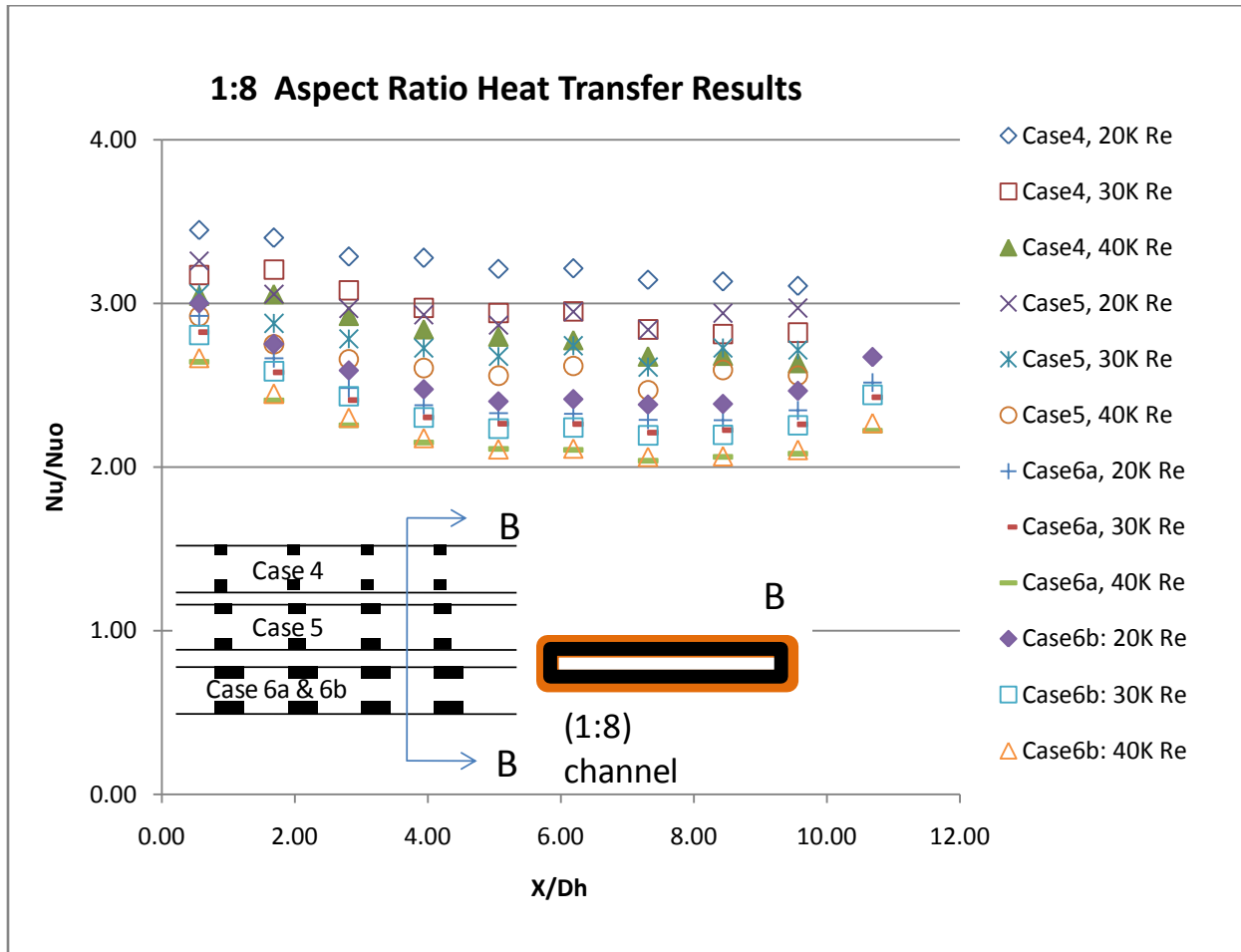


Figure 50: Summary of all cases ran for 1:8 aspect ratio channel

Of all the cases ran for the (1:8) aspect ratio channels, there seems to be no dominating wall effects like the (1:4) channel. From the results of the two channels, the larger aspect ratio channel has a more uniform heat transfer augmentation from wall to wall than the smaller channel. When comparing the two channels, Figure 45 and Figure 50, the (1:4) channel has a better augmentation at $e/P = 0.1$ and 0.3 , but has a similar augmentation for $e/P = 0.5$.

From Figure 45 and Figure 50, the trend of heat transfer augmentation decreases as a function of Reynolds number increase, which corresponds consistently with all available texts.

This is because the higher Reynolds number increases turbulence intensity, so the boundary layer disruption caused by the ribs becomes less effective. Rib's width also decreases the heat transfer augmentation as the e/P ratio become larger. Figure 51, taken from Webb et al [13] shows a distribution of the different P/e patterns. As the ribs becomes wider and wider, this led to less available space between the ribs to have the flow re-attach to the channel surface. Without the reattachment region, the local high heat transfer hot spot is not utilized to its fullest potential. From Figure 51, it requires 6 to 8 times the rib's height for the main flow to reattach, which means the rib size cannot exceed e/p of 0.3.

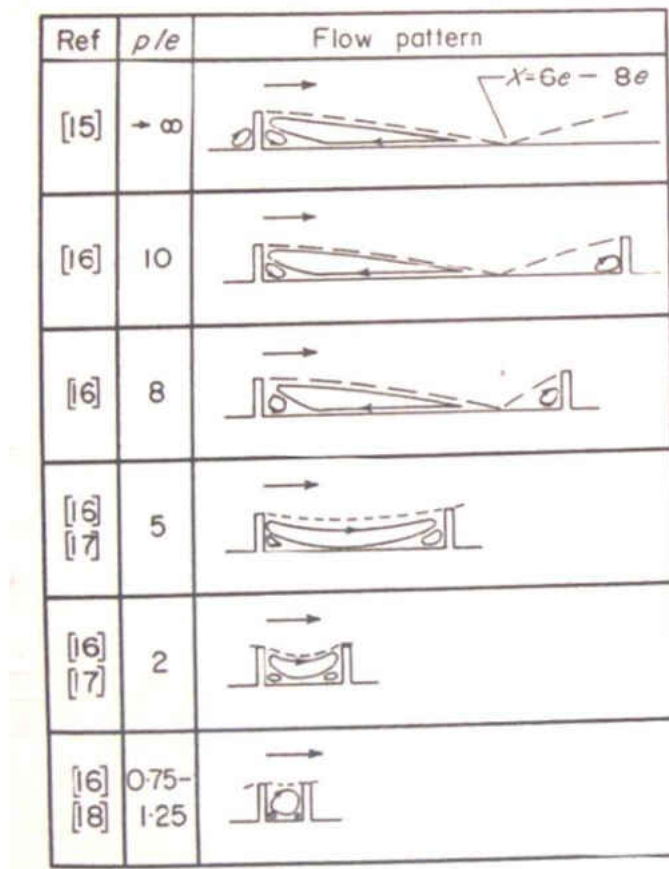


Figure 51: Flow pattern as a function of p/e Webb [13]

4.2.3 Pressure distribution results

The pressure measurements were taken consecutively with the heat transfer tests. Like the heat transfer distribution, the pressure results for the smooth walls were also compared with a correlation proposed by Blassius for internal pipe flow in terms of friction factor. The results for the (1:4) aspect ratio channels are available on Figure 52 and the results for the (1:8) aspect ratio channels are on Figure 53. With the overall uncertainty of the friction factors being less than 12 percent according to the Kline and McClintok [36] method.

The smooth wall friction factor for both channels matched Blassius correlation. With the ribs, the friction factor increased exponentially due to the large ribs. The current rib height-to-hydraulic diameter (e/D_h) is 0.125 and 0.1125 for AR of (1:4) and (1:8) respectively; which has a blockage ratio of 45 and 50 percent. There is a few available works for high blockage ratio channel; the location where such a design exists is in a place that has no pressure head limit and/or pressure head is not of an issue. These locations uses these channels for choke flow; or for structural support and the ribs function as flow turbulators. Figure 52 and Figure 53 shows a decrease in friction factor as the rib width increases. This is the opposite trend of the heat transfer enhancement. Webb [13], in 1970 explained the reason for such a phenomenon occurring. Figure 51 exhibits the different rib locations and their relative reattaching zone.

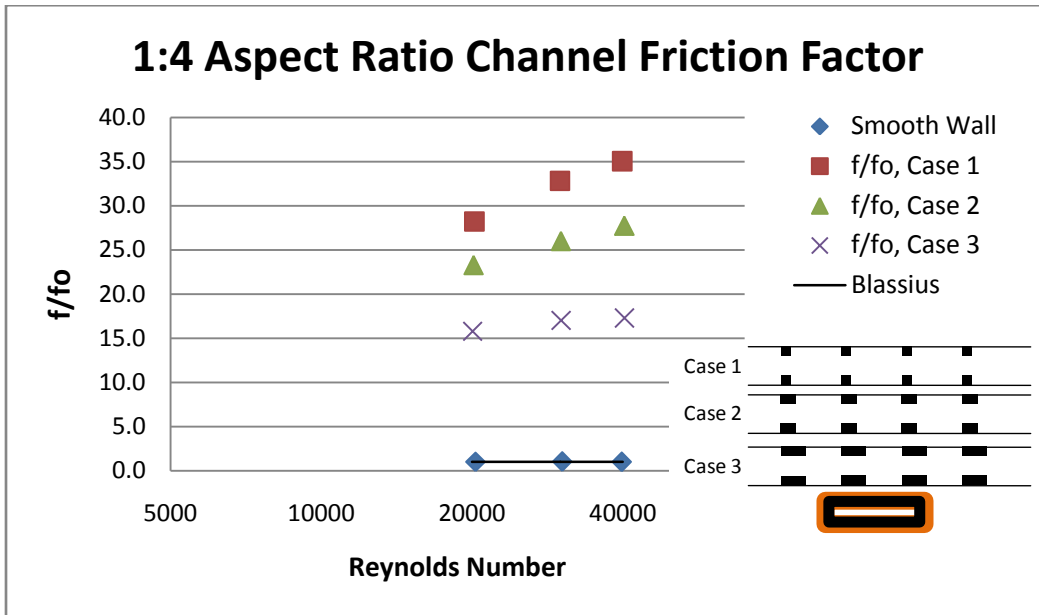


Figure 52: 1:4 aspect ratio channel friction factor distribution

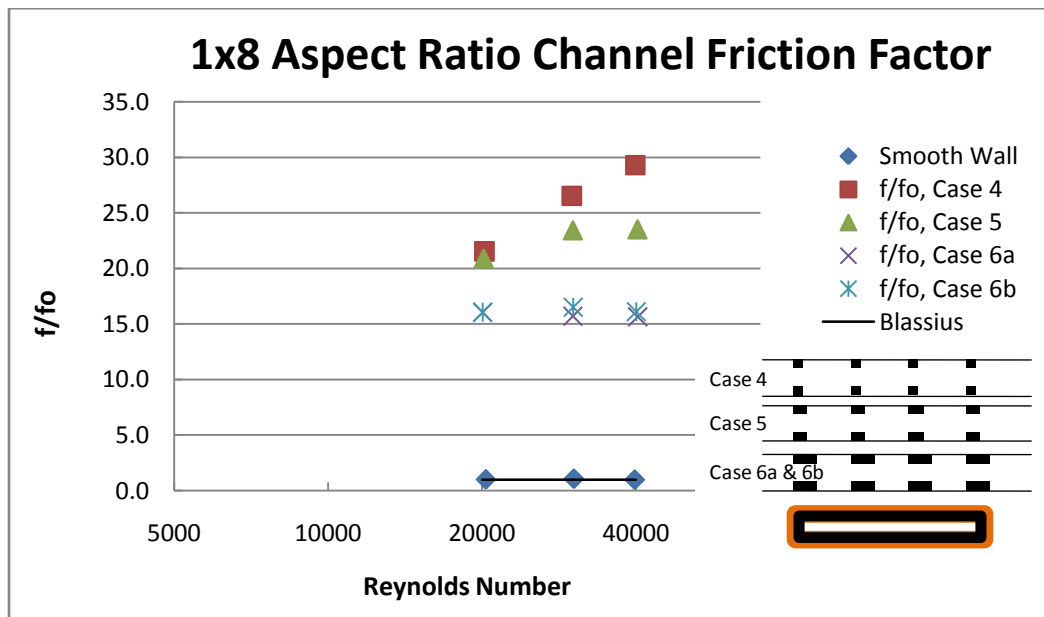


Figure 53: 1:8 aspect ratio channel friction factor distribution

For the current test setup, any rib size ratio $W_r/P > 0.1$, the flow will not be able to re-attach to the channel's surface between the ribs. Meaning that the fluid will jet across all the ribs causing only cavity driven flow between the consecutive ribs; this shall reduce the friction factor because the fluid does not re-attach to the channel's surface, a lower amount of momentum will be loss. The reason is because at the re-attachment zone, all local fluid momentum is loss and the boundary layer begins to grow.

To review the performance level of the current design, it is important to simultaneously look at both heat transfer and friction factor results. The thermal performance factor was once again calculated, the same equation 12 was used again. The results are shown in Figure 54 and Figure 55 for the (1:4) and (1:8) channels respectively.

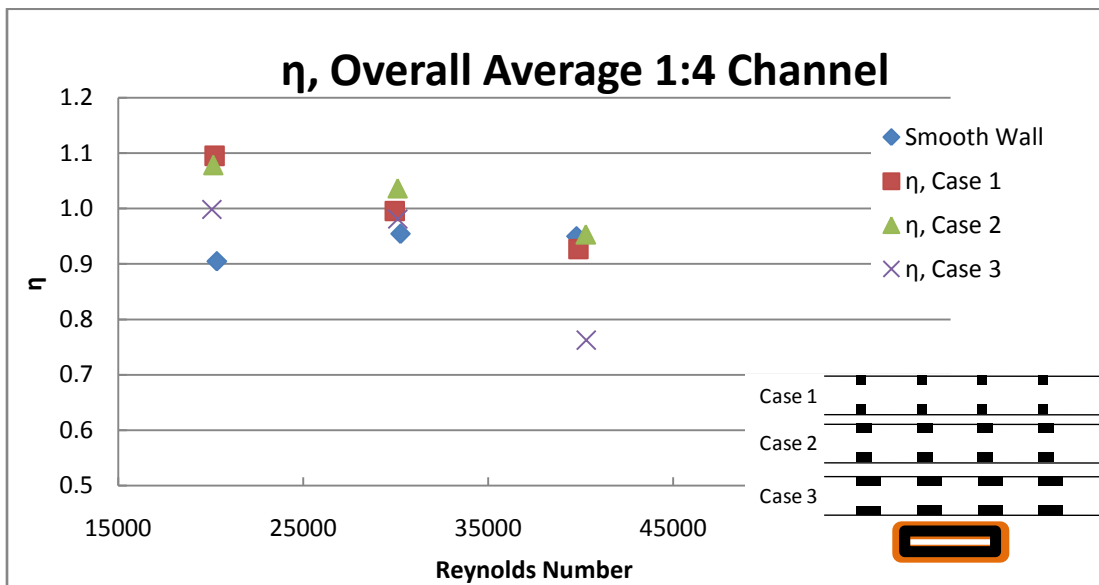


Figure 54: Thermal performance for the 1:4 aspect ratio channel

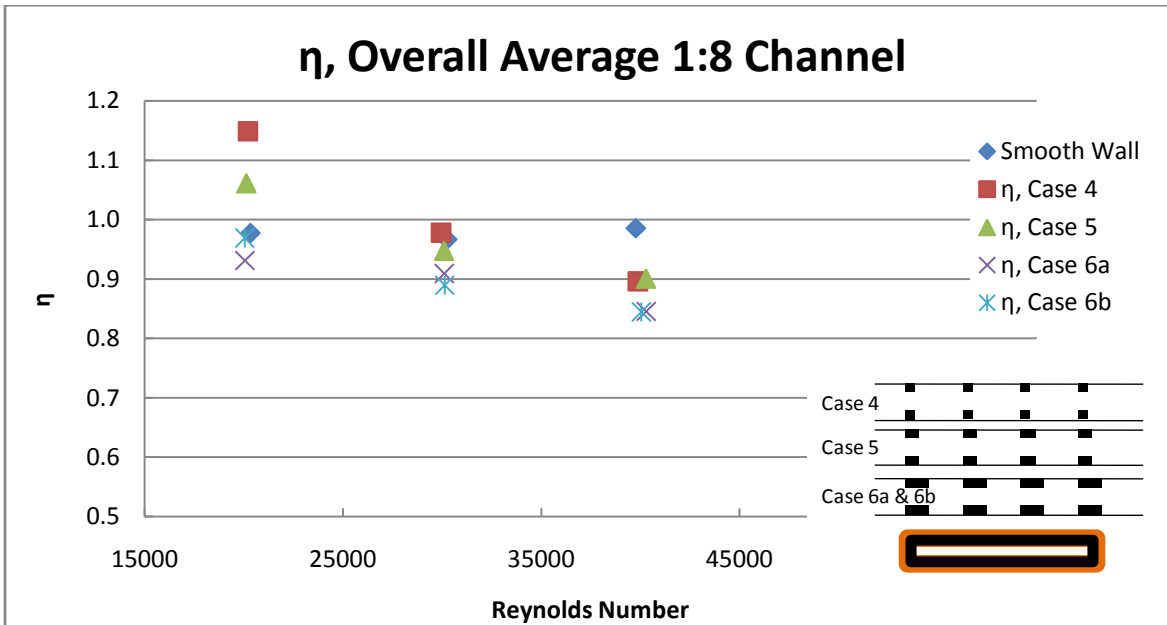


Figure 55: Thermal performance for the 1:8 aspect ratio channel

For a design to be thermally effective, the performance level needs to be one, like the smooth channels. The current design's thermal performance is similar to Taslim's [19] reported in Figure 29 for the largest blockage ratio. For the current rig, the blockage ratio is from 45 to 50%; hence the friction factor completely dominates, causing the thermal performance to decay.

Unexpectedly, the large rib does not perform like it was intended; high blockage ratio ribs should not be used for thermal performance factor alone. Large rib blockage ratio is best for heat transfer augmentation if the design does not put a large specification on pressure drop or the pressure supply is well over the channel design's pressure drop. Large ribs like the current turbulators' design is more useful for flow restriction or structure design.

4.2.4 Channel's correlation

With the data collected, a heat transfer and friction factor correlation using the law of the wall was attempted. The friction and heat transfer similarity laws in a 4 ribbed wall is expressed as follow [14]:

$$R = (f/2)^{-1/2} + 2.5 \ln((2e/D_h)(2W_c/(W_c+H))) + 2.5 \quad (13)$$

$$G = ((f/2)^{1/2})/St + 2.5 \ln((2e/D_h)(2W_c/(W_c+H_c))) + 2.5 \quad (14)$$

The friction factor for these correlations in equations (13) and (14) were converted to Fanning friction factor, which was equal to a quarter of the values obtained from equations (10) and (11). Figure 56 plotted the results using equation 13 to calculate the law of the wall's roughness function. To predict the roughness value, an equation to correlate all of these data is needed.

The Roughness value for this channel is a function of the aspect ratio and the rib aspect ratio:

$$R_{corel} = C*(W_c/H_c)^m (W_r/e)^n \quad (15)$$

where: for channel aspect ratio of 1:4 ($W_c:H$)

$$C = 3.8; \quad m = 0.661; \quad n = 0.074$$

for channel aspect ratio of 1:8 ($W_c:H$)

$$C = 2.7; \quad m = 0.661; \quad n = 0.0579$$

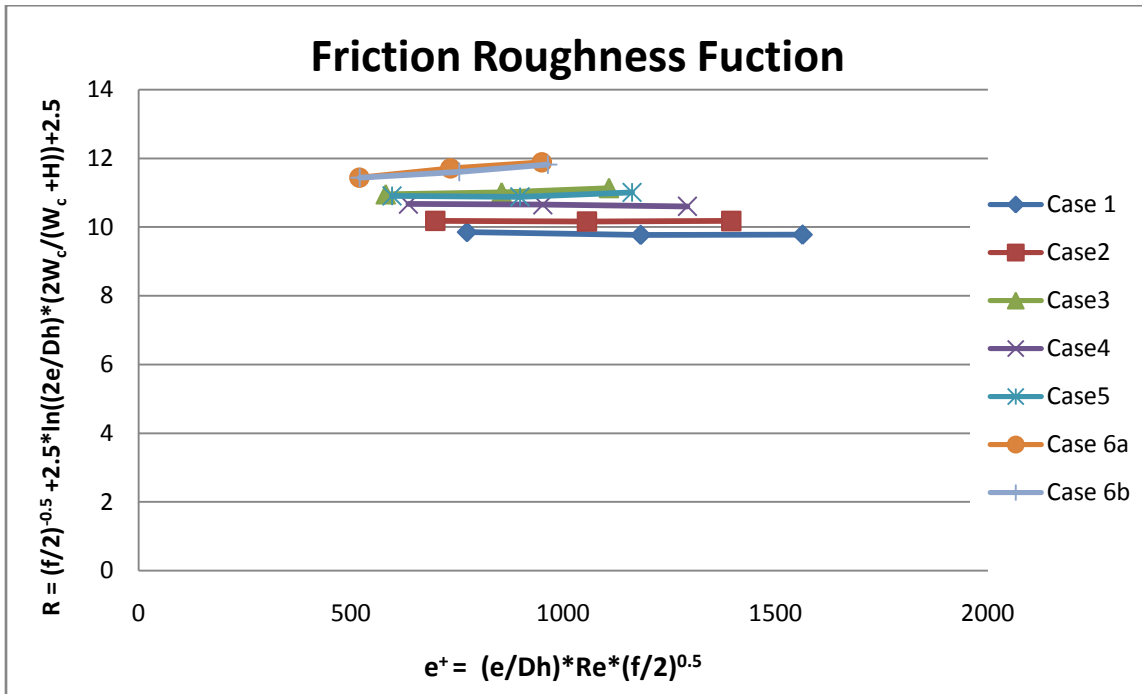


Figure 56: Friction roughness function

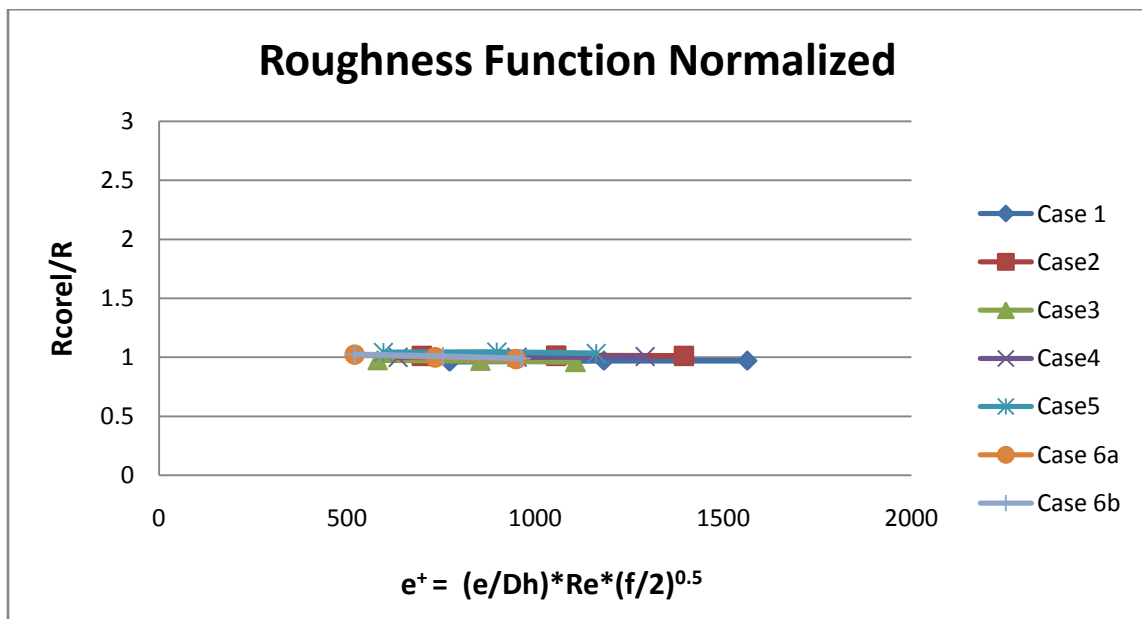


Figure 57: Normalize friction roughness function

The correlated values obtained using equation 15 is graphed as a normalized distribution with the law of the wall roughness correlation using equation 13 being graphed on Figure 57. It is apparent that the semi-empirical correlation using equation 15 matches with the law of the wall with a 4% discrepancy.

These are the same procedures as the heat transfer roughness function. Figure 58 is the plotted heat transfer roughness function for all cases ran using the law of the wall from equation 14. A semi-empirical data correlation was used to merge these data points together so that the heat transfer coefficient can calculate the desired Reynolds number. The correlation for this rig is identical to the correlation Han [11] used.

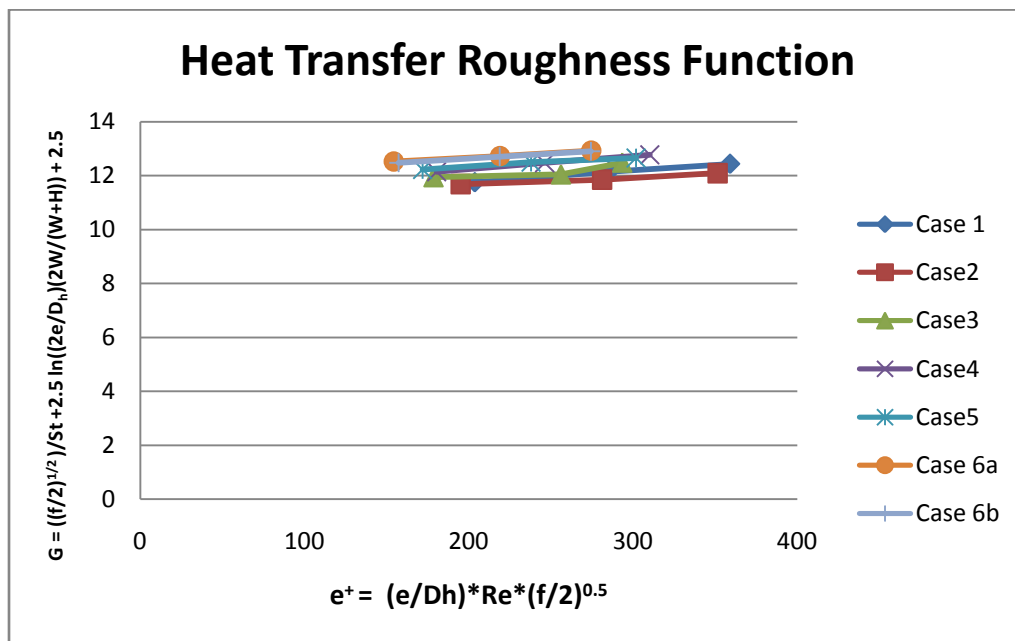


Figure 58: Heat transfer roughness function

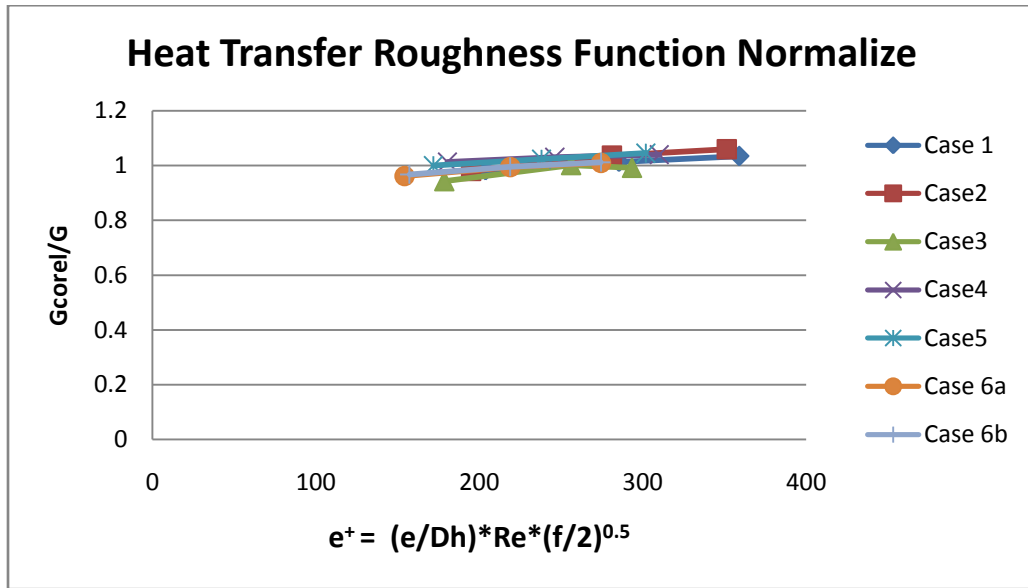


Figure 59: Normalize heat transfer roughness function

The data for both aspect ratios conformed to the heat transfer roughness function as a function of the roughness Reynolds number (e^+) and the channel aspect ratio. The correlation is in the form of:

$$G_{\text{corel}} = C(e^+)^n \left(\frac{W_c/H}{10}\right)^m \quad (16)$$

where: for the 1:4 ($W_c:H$) aspect ratio channel,

$$C = 6.514; \quad n = 0.1902; \quad m = 0.4781$$

for the 1:8 ($W_c:H$) aspect ratio channel,

$$C = 11.108; \quad n = 0.1402; \quad m = 2.802$$

The normalized value from the heat transfer roughness function with the law of the wall is plotted in Figure 59. All of these data are within $\pm 5\%$ discrepancy of one another.

CHAPTER 5: CONCLUSION/FUTURE WORKS

A number of large aspect ratio channels were tested with the parameter of rib-width-to-pitch variation. For the first test setup, although different inlet conditions were applied, the overall average heat transfer coefficient was not greatly affected. The following conclusions can be made:

- 1) With a high horizontal flow rate, the oscillating trend in the Nusselt number was observed from one segment to the next. This is because of the reattachment from the separation and circulation zone.
- 2) Thermal performance decreases as Reynolds number increases, following the trend of a number of authors because the increase in Reynolds number also means that the turbulence intensity of the flow is acting in conjunction with the turbulence caused by the ribs, resulting in the enhancement from the rib to decay.
- 3) Although the overall average Nu/Nu_0 was not affected by the inlet conditions, further investigations of the vertical channel's inlet needs to be thoroughly examined to determine the ratio of heat picked up by the bottommost copper surface entering the vertical channel.
- 4) The extent of the recirculation zone is still unknown from the effects of the horizontal flow conditioning. Other methods of measurements and/or CFD studies must be used to fully understand the local flow structures.

For the second test setup, extremely high blockage ratio for two different aspect ratio channels were tested with varying rib width while keeping all other parameters constant. The following conclusions were made:

- 1) The increase in rib width and without the appropriate pitch length, the flow will not re-attach to the channel's surface causing it to lose one of the highest heat transfer region.
- 2) For constant P/W_r parameters, square ribs ($e=W_r$) produces the highest heat transfer enhancement and the highest friction factor.
- 3) Friction factor drops with wider rib usage. This was explained by speculation that with the absence of the re-attachment zone, the momentum of the fluid would collide with the channel's surface and be saved.
- 4) A more in-depth parametric study is required in order to use of the idea of varying the rib's width for internal cooling channel
- 5) Semi-empirical correlations was also derived, results varied less than 5% of the existing data for both friction roughness function and the heat transfer roughness function using the law of the wall.

For future studies, it is best if the local data is acquired using thermochromatic liquid crystal technique to obtain the surface heat transfer coefficient. Computational Fluid Dynamics (CFD) is needed to locally study the effect of ribs and utilizes all local hot spot generated by the secondary flow effect and gaining the ability to view all of the flow structures throughout the channel.

APPENDIX: UNCERTAINTY CALCULATION

Error measured::

Manometer: range 0-52 "H2O
0.1% reading + 0.1% full scale + 1 digit

Manometer: range 0-52 inch H2O
accuracy +/- 0.2% of full scale
repeatability: +/- 0.1%

Voltmeter: +/- 0.005 volts (using Keithly)
+/- 0.01A + 2.5% of reading

DAQ system: Resolution 16bits
Input 0- +/- 5 volts

TC: gain 100 --> error (typical 0.01%) (max 0.1%)

CIO-EXP32 board.

venturi uncertainty +/- 3% of reading

$q = V \cdot I$ <-- Measured, with uncertainty of the voltmeter

$A = L \cdot W$ <-- Measured using the caliber, +/- 0.005 inch

T_i, T_{inf} <-- Measured using the computer DAQ system accuracy +/- 1degC

$h = q \cdot A \cdot T_i \quad T_{inf}$

INPUTS

flowrate := (61.2)scfm

<--Radial Vent Flowrate

$T_{inlet} := 24.3^{\circ}C$

<--Inlet Temperature

$T_{amb} := 24.6^{\circ}C$

<--Ambient Temperature

width := 4in

length := 2in

height := 1in

<-- copper's height, should not change

$A_{conRight} := \frac{3}{8} \text{in} \cdot 1 \text{in}$

$A_{conBottom} := \frac{3}{8} \text{in} \cdot 4 \text{in}$

$A_{conLeft} := A_{conRight}$

$A_{conTop} := A_{conBottom}$

Voltage Inputs, Right, Bottom, Left, Top wall

$$V_{\text{Right}} := \begin{pmatrix} 4.885 \\ 4.914 \\ 4.383 \\ 4.458 \\ 4.693 \\ 4.336 \\ 4.122 \\ 4.437 \\ 4.292 \\ 4.663 \end{pmatrix} \text{ V}$$

$$V_{\text{Bottom}} := \begin{pmatrix} 15.211 \\ 15.288 \\ 14.364 \\ 15.11 \\ 14.831 \\ 15.023 \\ 14.83 \\ 15.129 \\ 14.988 \\ 15.19 \end{pmatrix} \text{ V}$$

$$V_{\text{Left}} := \begin{pmatrix} 4.634 \\ 4.953 \\ 4.821 \\ 4.907 \\ 4.822 \\ 4.774 \\ 4.587 \\ 4.451 \\ 4.851 \\ 4.586 \end{pmatrix} \text{ V}$$

$$V_{\text{Top}} := \begin{pmatrix} 15.033 \\ 15.432 \\ 15.119 \\ 14.688 \\ 15.01 \\ 14.974 \\ 15.041 \\ 14.953 \\ 14.945 \\ 14.651 \end{pmatrix} \text{ V}$$

$$\text{Current}_{\text{Right}} := 0.85\text{A}$$

$$\text{Current}_{\text{Bottom}} := 0.88\text{A}$$

$$\text{Current}_{\text{Left}} := 0.85\text{A}$$

$$\text{Current}_{\text{Top}} := 0.88\text{A}$$

Temperature Inputs, Right, Bottom, Left, Top wall

$$T_{\text{RightCu}} := \begin{pmatrix} 52.52 \\ 55.48 \\ 55.28 \\ 57.01 \\ 57.4 \\ 58.45 \\ 59.02 \\ 60.6 \\ 60.02 \\ 61.52 \end{pmatrix} \text{ }^{\circ}\text{C}$$

$$T_{\text{BottomCu}} := \begin{pmatrix} 51.87 \\ 53.24 \\ 53.06 \\ 55.72 \\ 55.19 \\ 57.44 \\ 58.35 \\ 60.77 \\ 60.7 \\ 62.16 \end{pmatrix} \text{ }^{\circ}\text{C}$$

$$T_{\text{LeftCu}} := \begin{pmatrix} 50.48 \\ 55.3 \\ 55.48 \\ 59.3 \\ 58.89 \\ 60.66 \\ 61.18 \\ 61.56 \\ 63.45 \\ 63.27 \end{pmatrix} \text{ }^{\circ}\text{C}$$

$$T_{\text{TopCu}} := \begin{pmatrix} 52.68 \\ 55.72 \\ 56.59 \\ 57.81 \\ 59.88 \\ 61.65 \\ 62.24 \\ 63.47 \\ 64.68 \\ 64.32 \end{pmatrix} \text{ }^{\circ}\text{C}$$

Heat Leakage Loss Coefficient Inputs, Right, Bottom, Left, Top wall

$$\text{LossCoef}_{\text{Right}} := \begin{pmatrix} 7.85 \times 10^{-3} \\ 7.83 \times 10^{-3} \\ 7.22 \times 10^{-3} \\ 7.27 \times 10^{-3} \\ 7.21 \times 10^{-3} \\ 6.81 \times 10^{-3} \\ 7.12 \times 10^{-3} \\ 7.34 \times 10^{-3} \\ 7.96 \times 10^{-3} \\ 7.97 \times 10^{-3} \end{pmatrix} \frac{\text{W}}{\text{K}}$$

$$\text{LossCoef}_{\text{Bottom}} := \begin{pmatrix} 0.068 \\ 0.067 \\ 0.063 \\ 0.058 \\ 0.061 \\ 0.059 \\ 0.059 \\ 0.06 \\ 6.642 \times 10^{-3} \\ 0.066 \end{pmatrix} \frac{\text{W}}{\text{K}}$$

$$\text{LossCoef}_{\text{Left}} := \begin{pmatrix} 8.56 \times 10^{-3} \\ 7.72 \times 10^{-3} \\ 6.51 \times 10^{-3} \\ 6.66 \times 10^{-3} \\ 6.97 \times 10^{-3} \\ 6.5 \times 10^{-3} \\ 6.39 \times 10^{-3} \\ 7.19 \times 10^{-3} \\ 6.92 \times 10^{-3} \\ 8.01 \times 10^{-3} \end{pmatrix} \frac{\text{W}}{\text{K}}$$

$$\text{LossCoef}_{\text{Top}} := \begin{pmatrix} 0.062 \\ 0.057 \\ 0.059 \\ 0.056 \\ 0.052 \\ 0.056 \\ 0.052 \\ 0.055 \\ 0.058 \\ 0.06 \end{pmatrix} \frac{\text{W}}{\text{K}}$$

$$\Delta P := 0.0619 \text{ psi}$$

$$\text{inH}_2\text{O} \equiv \frac{\text{psi}}{2.768}$$

PARAMETERS

$$\mu \equiv 1.81 \cdot 10^{-5} \frac{\text{N}\cdot\text{s}}{\text{m}^2}$$

$$\text{scfm} \equiv \frac{\text{ft}^3}{\text{min}} \quad \text{density} \equiv 1.2 \frac{\text{kg}}{\text{m}^3}$$

$$m_{\text{dot}} := \text{density} \cdot \text{flow rate}$$

$$\text{Perimeter} := 2 \cdot (\text{height} + \text{width})$$

$$m_{\text{dot}} = 0.035 \frac{\text{kg}}{\text{s}}$$

$$\text{Pr} := 0.706$$

$$k_{\text{air}} := 0.0267 \frac{\text{W}}{\text{m}\cdot\text{K}}$$

$$\text{Joule} := 1 \text{N}\cdot\text{m}$$

$$\text{Cp} := 1008 \frac{\text{Joule}}{\text{kg}\cdot\text{K}}$$

$$D_h := \frac{4 \cdot \text{width} \cdot \text{height}}{2(\text{height} + \text{width})}$$

$$\text{Re} := \frac{4 \cdot m_{\text{dot}}}{\mu \cdot \text{Perimeter}}$$

$$D_h = 0.04064 \text{m}$$

$$d\text{length} := 0.005 \text{m}$$

$$d\text{height} := 0.005 \text{m}$$

$$\text{Re} = 30156$$

$$d\text{width} := 0.005 \text{m}$$

$$dT_{\text{inlet}} \equiv 1 \text{K}$$

$$d\text{flowrate} := 0.03 \text{flow rate}$$

$$d\text{flowrate} = 1.836 \text{scfm}$$

Cork Thickness:

$$\text{Cork}_{\text{thick}} \equiv .0015 \text{m}$$

$$K_{\text{cork}} \equiv 0.043 \frac{\text{W}}{\text{m}\cdot\text{K}}$$

$$dD_h := 2 \sqrt{\left[\frac{2 \cdot \text{width}^2}{(\text{height} + \text{width})^2} \cdot d\text{height} \right]^2 + \left[\frac{(2 \cdot \text{height})^2}{(\text{height} + \text{width})^2} \cdot d\text{width} \right]^2}$$

$$dD_h = 3.277 \times 10^{-4} \text{m}$$

$$d\text{Perimeter} := \sqrt{(2 \cdot d\text{height})^2 + (2 \cdot d\text{width})^2}$$

$$d\text{Perimeter} = 3.592 \times 10^{-4} \text{m}$$

$$dm_{\text{dot}} := d\text{flowrate} \cdot \text{density}$$

<-- Flow Rate uncertainty, This will be used for uncertainty in RE and HTC,DB

$$\dot{m}_{\text{dot}} = 1.04 \times 10^{-3} \frac{\text{kg}}{\text{s}}$$

$$d\text{ReN} := 4 \sqrt{\left(\frac{1 \dot{m}_{\text{dot}}}{\mu \cdot \text{Perimeter}} \right)^2 + \left(\frac{-\dot{m}_{\text{dot}}}{\mu \cdot \text{Perimeter}^2} d\text{Perimeter} \right)^2}$$

<-- Reynolds Number
Uncertainty

$$d\text{ReN} = 905.685$$

Power uncertainty Parameters

$$dV_{\text{Right}} := 0.005\text{V}$$

$$dV_{\text{Bottom}} := 0.005\text{V}$$

$$d\text{Current}_{\text{Right}} := \text{Current}_{\text{Right}} \cdot 0.025 + 0.01\text{A}$$

$$d\text{Current}_{\text{Bottom}} := \text{Current}_{\text{Bottom}} \cdot 0.025 + 0.01\text{A}$$

$$d\text{Current}_{\text{Right}} = 0.031\text{A}$$

$$d\text{Current}_{\text{Bottom}} = 0.032\text{A}$$

$$dV_{\text{Left}} := 0.005\text{V}$$

$$dV_{\text{Top}} := 0.005\text{V}$$

$$d\text{Current}_{\text{Left}} := \text{Current}_{\text{Left}} \cdot 0.025 + 0.01\text{A}$$

$$d\text{Current}_{\text{Top}} := \text{Current}_{\text{Top}} \cdot 0.025 + 0.01\text{A}$$

$$d\text{Current}_{\text{Left}} = 0.031\text{A}$$

$$d\text{Current}_{\text{Top}} = 0.032\text{A}$$

(Dittus-Boelter Eqn & its Uncertainty)

$$\text{Nu}_{\text{DB}} := 0.023 \text{Re}^{\frac{4}{5}} \cdot \text{Pr}^{0.4}$$

$$\text{Nu}_{\text{DB}} = 76.692$$

$$\text{HTC}_{\text{DB}} := k_{\text{air}} \frac{\text{Nu}_{\text{DB}}}{D_h}$$

$$\text{HTC}_{\text{DB}} = 50.386 \frac{\text{W}}{\text{m}^2 \text{K}}$$

$$dNu_{DB} := \sqrt{\left(0.023 \frac{4}{5} \cdot Re^{\frac{4}{5}-1} \cdot Pr^{0.4} \cdot dReN\right)^2}$$

← Dittus-Boelter
Uncertainty

$$dNu_{DB} = 1.843$$

$$dHTC_{DB} := \sqrt{\left(k_{air} \cdot \frac{dNu_{DB}}{D_h}\right)^2 + \left(\frac{-k_{air} \cdot Nu_{DB}}{D_h^2} \cdot dD_h\right)^2}$$

$$dHTC_{DB} = 1.277 \frac{W}{m^2 K}$$

Flow Area Uncertainty

$$dA := \sqrt{(\text{height} \cdot d\text{width})^2 + (\text{width} \cdot d\text{height})^2}$$

$$dA = 0.02 \text{ in}^2$$

← Cross section area Uncertainty

$$\text{Area}_{Right} := \text{height} \cdot \text{length}$$

$$d\text{Area}_{Right} := \sqrt{(\text{height} \cdot d\text{length})^2 + (d\text{height} \cdot \text{length})^2}$$

$$\text{Area}_{Left} := \text{Area}_{Right}$$

$$d\text{Area}_{Left} := d\text{Area}_{Right}$$

$$\text{Area}_{Bottom} := \text{length} \cdot \text{width}$$

$$d\text{Area}_{Bottom} := \sqrt{(\text{length} \cdot d\text{width})^2 + (d\text{length} \cdot \text{width})^2}$$

$$\text{Area}_{Top} := \text{Area}_{Bottom}$$

$$d\text{Area}_{Top} := d\text{Area}_{Bottom}$$

Uncertainty, Right Wall

$$i := 0, 1..9$$

$$dT_{\text{RightCu}_i} := \frac{1\text{K}}{T_{\text{RightCu}_i}} \cdot T_{\text{RightCu}_i}$$

$$dT_{\text{RightCu}} = \begin{array}{|c|} \hline 1 \\ \hline 1 \\ \hline 1 \\ \hline 1 \\ \hline 1 \\ \hline 1 \\ \hline 1 \\ \hline 1 \\ \hline 1 \\ \hline 1 \\ \hline \end{array} \text{ K}$$

$$\text{Power}_{\text{Right}} := V_{\text{Right}} \cdot \text{Current}_{\text{Right}}$$

$$\text{Power}_{\text{Right}} = \begin{array}{|c|} \hline 4.152 \\ \hline 4.177 \\ \hline 3.726 \\ \hline 3.789 \\ \hline 3.989 \\ \hline 3.686 \\ \hline 3.504 \\ \hline 3.771 \\ \hline 3.648 \\ \hline 3.964 \\ \hline \end{array} \text{ W}$$

$$\Delta T_{\text{Right}} := \begin{array}{|l} \hline i \leftarrow 0 \\ \hline \text{for } i \in 0..9 \\ \hline \Delta T_{\text{Right}_i} \leftarrow T_{\text{RightCu}_i} - T_{\text{amb}} \\ \hline \Delta T_{\text{Right}} \\ \hline \end{array}$$

$$\Delta T_{\text{Right}} = \begin{array}{|c|} \hline 27.92 \\ \hline 30.88 \\ \hline 30.68 \\ \hline 32.41 \\ \hline 32.8 \\ \hline 33.85 \\ \hline 34.42 \\ \hline 36 \\ \hline 35.42 \\ \hline 36.92 \\ \hline \end{array} \text{ K}$$

Energy loss to the environment::: These data points are taken from the heat leakage dat

$$Q_{\text{lossRight}} := \begin{cases} i \leftarrow 0 \\ \text{for } i \in 0..9 \\ Q_{\text{lossRight}_i} \leftarrow \text{LossCoef}_{\text{Right}_i} \cdot \Delta T_{\text{Right}_i} \\ Q_{\text{lossRight}} \end{cases}$$

0.219
0.242
0.222
0.236
0.236
0.231
0.245
0.264
0.282
0.294

$Q_{\text{lossRight}} =$ W

Lateral Conduction Right Wall

$$\text{ConResis}_{\text{Right}} := \frac{\text{Cork}_{\text{thick}}}{K_{\text{cork}} \cdot A_{\text{conRight}}}$$

$$Q_{\text{inRight}} := \begin{cases} i \leftarrow 0 \\ Q_{\text{inRight}_i} \leftarrow \frac{T_{\text{RightCu}_{i+1}} - T_{\text{RightCu}_i}}{\text{ConResis}_{\text{Right}}} \\ \text{for } i \in 1..8 \\ Q_{\text{inRight}_i} \leftarrow \frac{T_{\text{RightCu}_{i+1}} - T_{\text{RightCu}_i} + T_{\text{RightCu}_{i-1}} - T_{\text{RightCu}_i}}{\text{ConResis}_{\text{Right}}} \\ Q_{\text{inRight}_9} \leftarrow \frac{T_{\text{RightCu}_9} - T_{\text{RightCu}_8}}{\text{ConResis}_{\text{Right}}} \\ Q_{\text{inRight}} \end{cases}$$

$$Q_{\text{inRight}} =$$

0.021
-0.022
0.013
-9.294·10 ⁻³
4.577·10 ⁻³
-3.329·10 ⁻³
7.005·10 ⁻³
-0.015
0.014
0.01

W

<-- Lateral Conduction from one module to the next for the right wall only

$$P_{\text{Right}} := \begin{cases} i \leftarrow 0 \\ \text{for } i \in 0..9 \\ P_{\text{Right}_i} \leftarrow \text{Power}_{\text{Right}_i} + Q_{\text{inRight}_i} - Q_{\text{lossRight}_i} \\ P_{\text{Right}} \end{cases}$$

3.954
3.913
3.517
3.544
3.757
3.452
3.266
3.492
3.381
3.68

<-- Use to calculate Tbulk only

$$Q_{\text{actualRight}} := \begin{cases} i \leftarrow 0 \\ Q_{\text{actualRight}_i} \leftarrow \frac{P_{\text{Right}_i}}{2} \\ \text{for } i \in 1..9 \\ Q_{\text{actualRight}_i} \leftarrow \frac{1}{2}(P_{\text{Right}_{i-1}} + P_{\text{Right}_i}) \\ Q_{\text{actualRight}_{10}} \leftarrow \frac{P_{\text{Right}_9}}{2} \\ Q_{\text{actualRight}} \end{cases}$$

1.977
3.933
3.715
3.531
3.651
3.604
3.359
3.379
3.436
3.53
1.84

$$dQ_{\text{actualRight}} := \begin{cases} i \leftarrow 0 \\ dQ_{\text{actualRight}_i} \leftarrow \frac{\sqrt{(V_{\text{Right}_i} \cdot d\text{Current}_{\text{Right}})^2 + |\text{Current}_{\text{Right}} \cdot dV_{\text{Right}}|^2}}{2} \\ \text{for } i \in 1..9 \\ dQ_{\text{actualRight}_i} \leftarrow \frac{1}{2} \cdot \frac{\sqrt{(V_{\text{Right}_{i-1}} \cdot d\text{Current}_{\text{Right}})^2 + |\text{Current}_{\text{Right}} \cdot dV_{\text{Right}}|^2} \dots}{\sqrt{(V_{\text{Right}_i} \cdot d\text{Current}_{\text{Right}})^2 + |\text{Current}_{\text{Right}} \cdot dV_{\text{Right}}|^2}} \\ dQ_{\text{actualRight}_{10}} \leftarrow \frac{\sqrt{(V_{\text{Right}_9} \cdot d\text{Current}_{\text{Right}})^2 + |\text{Current}_{\text{Right}} \cdot dV_{\text{Right}}|^2}}{2} \\ dQ_{\text{actualRight}} \end{cases}$$

$$dQ_{\text{actual Right}} = \begin{array}{|c|} \hline 0.076 \\ \hline 0.108 \\ \hline 0.103 \\ \hline 0.098 \\ \hline 0.101 \\ \hline 0.1 \\ \hline 0.094 \\ \hline 0.095 \\ \hline 0.097 \\ \hline 0.099 \\ \hline 0.073 \\ \hline \end{array} \text{ W}$$

Uncertainty, Bottom Wall

$$i := 0, 1..9$$

$$dT_{\text{BottomCu}_i} := \frac{1\text{K}}{T_{\text{BottomCu}_i}} \cdot T_{\text{BottomCu}_i}$$

$$dT_{\text{BottomCu}} = \begin{array}{|c|} \hline 1 \\ \hline 1 \\ \hline 1 \\ \hline 1 \\ \hline 1 \\ \hline 1 \\ \hline 1 \\ \hline 1 \\ \hline 1 \\ \hline \end{array} \text{ K}$$

$$\text{Power}_{\text{Bottom}} := V_{\text{Bottom}} \cdot \text{Current}_{\text{Bottom}}$$

$$\text{Power}_{\text{Bottom}} = \begin{array}{|c|} \hline 13.386 \\ \hline 13.453 \\ \hline 12.64 \\ \hline 13.297 \\ \hline 13.051 \\ \hline 13.22 \\ \hline 13.05 \\ \hline 13.314 \\ \hline 13.189 \\ \hline 13.367 \\ \hline \end{array} \text{ W}$$

$$\Delta T_{\text{Bottom}} := \begin{cases} i \leftarrow 0 \\ \text{for } i \in 0..9 \\ \Delta T_{\text{Bottom}_i} \leftarrow T_{\text{BottomCu}_i} - T_{\text{amb}} \\ \Delta T_{\text{Bottom}} \end{cases}$$

$$\Delta T_{\text{Bottom}} = \begin{array}{|c|} \hline 27.27 \\ \hline 28.64 \\ \hline 28.46 \\ \hline 31.12 \\ \hline 30.59 \\ \hline 32.84 \\ \hline 33.75 \\ \hline 36.17 \\ \hline 36.1 \\ \hline 37.56 \\ \hline \end{array} \text{ K}$$

Energy loss to the environment::: These data points are taken from the heat leakage dat

$$\begin{array}{l}
 \text{Qloss}_{\text{Bottom}} := \left| \begin{array}{l}
 i \leftarrow 0 \\
 \text{for } i \in 0..9 \\
 \text{Qloss}_{\text{Bottom}_i} \leftarrow \text{LossCoef}_{\text{Bottom}_i} \cdot \Delta T_{\text{Bottom}_i} \\
 \text{Qloss}_{\text{Bottom}}
 \end{array} \right.
 \end{array}$$

1.854
1.919
1.793
1.805
1.866
1.938
1.991
2.17
0.24
2.479

Qloss_{Bottom} = W

Lateral Conduction

$$\text{ConRes}_{\text{Bottom}} := \frac{\text{Cork}_{\text{thick}}}{K_{\text{cork}} \cdot A_{\text{conBottom}}}$$

$$\begin{array}{l}
 \text{Qin}_{\text{Bottom}} := \left| \begin{array}{l}
 i \leftarrow 0 \\
 \text{Qin}_{\text{Bottom}_i} \leftarrow \frac{T_{\text{BottomCu}_{i+1}} - T_{\text{BottomCu}_i}}{\text{ConRes}_{\text{Bottom}}} \\
 \text{for } i \in 1..8 \\
 \text{Qin}_{\text{Bottom}_i} \leftarrow \frac{T_{\text{BottomCu}_{i+1}} - T_{\text{BottomCu}_i} + T_{\text{BottomCu}_{i-1}} - T_{\text{BottomCu}_i}}{\text{ConRes}_{\text{Right}}} \\
 \text{Qin}_{\text{Bottom}_9} \leftarrow \frac{T_{\text{BottomCu}_9} - T_{\text{BottomCu}_8}}{\text{ConRes}_{\text{Bottom}}} \\
 \text{Qin}_{\text{Bottom}}
 \end{array} \right.
 \end{array}$$

$$Q_{in_Bottom} = \begin{array}{|c|} \hline 0.038 \\ \hline -0.011 \\ \hline 0.02 \\ \hline -0.022 \\ \hline 0.019 \\ \hline -9.294 \cdot 10^{-3} \\ \hline 0.01 \\ \hline -0.017 \\ \hline 0.011 \\ \hline 0.041 \\ \hline \end{array} W$$

<-- Lateral Conduction from one module to the next for the Bottom wall only

$$P_{Bottom} := \begin{array}{|l} \hline i \leftarrow 0 \\ \hline \text{for } i \in 0..9 \\ \hline P_{Bottom_i} \leftarrow Power_{Bottom_i} + Q_{in_Bottom_i} - Q_{loss_Bottom_i} \\ \hline P_{Bottom} \\ \hline \end{array} \quad P_{Bottom} = \begin{array}{|c|} \hline 11.569 \\ \hline 11.524 \\ \hline 10.867 \\ \hline 11.47 \\ \hline 11.205 \\ \hline 11.273 \\ \hline 11.07 \\ \hline 11.126 \\ \hline 12.96 \\ \hline 10.929 \\ \hline \end{array} W$$

<-- Use to calculate Tbulk only

$$Q_{actual_Bottom} := \begin{array}{|l} \hline i \leftarrow 0 \\ \hline Q_{actual_Bottom_i} \leftarrow \frac{P_{Bottom_i}}{2} \\ \hline \text{for } i \in 1..9 \\ \hline Q_{actual_Bottom_i} \leftarrow \frac{1}{2} (P_{Bottom_{i-1}} + P_{Bottom_i}) \\ \hline Q_{actual_Bottom_{10}} \leftarrow \frac{P_{Bottom_9}}{2} \\ \hline Q_{actual_Bottom} \\ \hline \end{array} \quad Q_{actual_Bottom} = \begin{array}{|c|} \hline 5.785 \\ \hline 11.547 \\ \hline 11.195 \\ \hline 11.168 \\ \hline 11.337 \\ \hline 11.239 \\ \hline 11.172 \\ \hline 11.098 \\ \hline 12.043 \\ \hline 11.945 \\ \hline 5.464 \\ \hline \end{array} W$$

$$\begin{aligned}
 dQ_{\text{actualBottom}} &:= \begin{cases} i \leftarrow 0 \\ dQ_{\text{actualBottom}_i} \leftarrow \sqrt{\frac{(V_{\text{Bottom}_i} \cdot d\text{Current}_{\text{Bottom}})^2 + |\text{Current}_{\text{Bottom}} \cdot dV_{\text{Bottom}}|^2}{2}} \\ \text{for } i \in 1..9 \\ dQ_{\text{actualBottom}_i} \leftarrow \frac{1}{2} \cdot \sqrt{\frac{\left[\sqrt{(V_{\text{Bottom}_{i-1}} \cdot d\text{Current}_{\text{Bottom}})^2 + |\text{Current}_{\text{Bottom}} \cdot dV_{\text{Bottom}}|^2} \right]^2 + (V_{\text{Bottom}_i} \cdot d\text{Current}_{\text{Bottom}})^2 + |\text{Current}_{\text{Bottom}} \cdot dV_{\text{Bottom}}|^2}{2}} \\ dQ_{\text{actualBottom}_{10}} \leftarrow \sqrt{\frac{(V_{\text{Bottom}_9} \cdot d\text{Current}_{\text{Bottom}})^2 + |\text{Current}_{\text{Bottom}} \cdot dV_{\text{Bottom}}|^2}{2}} \\ dQ_{\text{actualBottom}} \end{cases}
 \end{aligned}$$

0.243
0.345
0.336
0.334
0.339
0.338
0.338
0.339
0.341
0.341
0.243

dQ_{actualBottom} = W

Uncertainty, Left Wall

$$i := 0, 1..9$$

$$dT_{LeftCu_i} := \frac{1K}{T_{LeftCu_i}} \cdot T_{LeftCu_i}$$

1
1
1
1
1
1
1
1
1
1

$$dT_{LeftCu} = \text{K}$$

$$Power_{Left} := V_{Left} \cdot Current_{Left}$$

3.939
4.21
4.098
4.171
4.099
4.058
3.899
3.783
4.123
3.898

$$Power_{Left} = \text{W}$$

$$\Delta T_{Left} := \begin{cases} i \leftarrow 0 \\ \text{for } i \in 0..9 \\ \Delta T_{Left_i} \leftarrow T_{LeftCu_i} - T_{amb} \\ \Delta T_{Left} \end{cases}$$

25.88
30.7
30.88
34.7
34.29
36.06
36.58
36.96
38.85
38.67

$$\Delta T_{Left} = \text{K}$$

Energy loss to the environment::: These data points are taken from the heat leakage dat

$$Q_{lossLeft} := \begin{cases} i \leftarrow 0 \\ \text{for } i \in 0..9 \\ Q_{lossLeft_i} \leftarrow LossCoef_{Left_i} \cdot \Delta T_{Left_i} \\ Q_{lossLeft} \end{cases}$$

0.222
0.237
0.201
0.231
0.239
0.234
0.234
0.266
0.269
0.31

$$Q_{lossLeft} = \text{W}$$

Lateral Conduction Left Wall only

$$\text{ConResis}_{\text{Left}} := \frac{\text{Cork}_{\text{thick}}}{K_{\text{cork}} \cdot A_{\text{conLeft}}}$$

$$\text{Qin}_{\text{Left}} := \begin{cases} i \leftarrow 0 \\ \text{Qin}_{\text{Left}_i} \leftarrow \frac{T_{\text{LeftCu}_{i+1}} - T_{\text{LeftCu}_i}}{\text{ConResis}_{\text{Left}}} \\ \text{for } i \in 1..8 \\ \text{Qin}_{\text{Left}_i} \leftarrow \frac{T_{\text{LeftCu}_{i+1}} - T_{\text{LeftCu}_i} + T_{\text{LeftCu}_{i-1}} - T_{\text{LeftCu}_i}}{\text{ConResis}_{\text{Right}}} \\ \text{Qin}_{\text{Left}_9} \leftarrow \frac{T_{\text{LeftCu}_9} - T_{\text{LeftCu}_8}}{\text{ConResis}_{\text{Left}}} \\ \text{Qin}_{\text{Left}} \end{cases}$$

0.033
-0.032
0.025
-0.029
0.015
-8.669·10 ⁻³
-9.71·10 ⁻⁴
0.01
-0.014
-1.248·10 ⁻³

Qin_{Left} = W

<-- Lateral Conduction from one module to the next for the right wall only

$$\text{P}_{\text{Left}} := \begin{cases} i \leftarrow 0 \\ \text{for } i \in 0..9 \\ \text{P}_{\text{Left}_i} \leftarrow \text{Power}_{\text{Left}_i} + \text{Qin}_{\text{Left}_i} - \text{Qloss}_{\text{Left}_i} \\ \text{P}_{\text{Left}} \end{cases}$$

3.751
3.941
3.922
3.911
3.875
3.815
3.664
3.528
3.84
3.587

P_{Left} = W

Qactual_{Left} :=

i ← 0	
Qactual _{Left_i} ← $\frac{P_{Left_i}}{2}$	
for i ∈ 1..9	
Qactual _{Left_i} ← $\frac{1}{2}(P_{Left_{i-1}} + P_{Left_i})$	
Qactual _{Left₁₀} ← $\frac{P_{Left_9}}{2}$	
Qactual _{Left}	

← Use to calculate Tbulk only

1.875
3.846
3.931
3.916
3.893
3.845
3.74
3.596
3.684
3.714
1.794

Qactual_{Left} = W

dQactual_{Left} :=

i ← 0	
dQactual _{Left_i} ← $\frac{\sqrt{(V_{Left_i} \cdot dCurrent_{Left})^2 + (Current_{Left} \cdot dV_{Left})^2}}{2}$	
for i ∈ 1..9	
dQactual _{Left_i} ← $\frac{1}{2} \cdot \left[\frac{\sqrt{(V_{Left_{i-1}} \cdot dCurrent_{Left})^2 + (Current_{Left} \cdot dV_{Left})^2}}{\sqrt{(V_{Left_i} \cdot dCurrent_{Left})^2 + (Current_{Left} \cdot dV_{Left})^2}} \right] \dots$	
dQactual _{Left₁₀} ← $\frac{\sqrt{(V_{Left_9} \cdot dCurrent_{Left})^2 + (Current_{Left} \cdot dV_{Left})^2}}{2}$	
dQactual _{Left}	

0.072
0.106
0.108
0.108
0.108
0.106
0.103
0.1
0.103
0.104
0.072

dQactual_{Left} = W

Uncertainty, Top Wall

$$i := 0, 1..9$$

$$dT_{TopCu_i} := \frac{1K}{T_{TopCu_i}} \cdot T_{TopCu_i}$$

$$dT_{TopCu} =$$

1
1
1
1
1
1
1
1
1
1

K

$$Power_{Top} := V_{Top} \cdot Current_{Top}$$

$$Power_{Top} =$$

13.229
13.58
13.305
12.925
13.209
13.177
13.236
13.159
13.152
12.893

W

$$\Delta T_{Top} := \begin{cases} i \leftarrow 0 \\ \text{for } i \in 0..9 \\ \Delta T_{Top_i} \leftarrow T_{TopCu_i} - T_{amb} \\ \Delta T_{Top} \end{cases}$$

$$\Delta T_{Top} =$$

28.08
31.12
31.99
33.21
35.28
37.05
37.64
38.87
40.08
39.72

K

Energy loss to the environment::: These data points are taken from the heat leakage dat

$$Q_{loss_{Top}} := \begin{cases} i \leftarrow 0 \\ \text{for } i \in 0..9 \\ Q_{loss_{Top_i}} \leftarrow LossCoef_{Top_i} \cdot \Delta T_{Top_i} \\ Q_{loss_{Top}} \end{cases}$$

$$Q_{loss_{Top}} =$$

1.741
1.774
1.887
1.86
1.835
2.075
1.957
2.138
2.325
2.383

W

Lateral Conduction Top Wall only

$$\text{ConResis}_{\text{Top}} := \frac{\text{Cork}_{\text{thick}}}{K_{\text{cork}} \cdot A_{\text{conTop}}}$$

$$\text{Qin}_{\text{Top}} := \left| \begin{array}{l} i \leftarrow 0 \\ \text{Qin}_{\text{Top}_i} \leftarrow \frac{T_{\text{TopCu}_{i+1}} - T_{\text{TopCu}_i}}{\text{ConResis}_{\text{Top}}} \\ \text{for } i \in 1..8 \\ \text{Qin}_{\text{Top}_i} \leftarrow \frac{T_{\text{TopCu}_{i+1}} - T_{\text{TopCu}_i} + T_{\text{TopCu}_{i-1}} - T_{\text{TopCu}_i}}{\text{ConResis}_{\text{Right}}} \\ \text{Qin}_{\text{Top}_9} \leftarrow \frac{T_{\text{TopCu}_9} - T_{\text{TopCu}_8}}{\text{ConResis}_{\text{Top}}} \\ \text{Qin}_{\text{Top}} \end{array} \right.$$

0.084
-0.015
2.427·10 ⁻³
5.895·10 ⁻³
-2.081·10 ⁻³
-8.184·10 ⁻³
4.439·10 ⁻³
-1.387·10 ⁻⁴
-0.011
-9.987·10 ⁻³

Qin_{Top} = W

<- Lateral Conduction from one module to the next for the right wall only

$$\text{P}_{\text{Top}} := \left| \begin{array}{l} i \leftarrow 0 \\ \text{for } i \in 0..9 \\ \text{P}_{\text{Top}_i} \leftarrow \text{Power}_{\text{Top}_i} + \text{Qin}_{\text{Top}_i} - \text{Qloss}_{\text{Top}_i} \\ \text{P}_{\text{Top}} \end{array} \right.$$

11.572
11.791
11.42
11.072
11.372
11.094
11.283
11.021
10.816
10.5

P_{Top} = W

← Use to calculate Tbulk only

$$\begin{array}{l}
 \text{Qactual}_{\text{Top}} := \left| \begin{array}{l}
 i \leftarrow 0 \\
 \text{Qactual}_{\text{Top}_i} \leftarrow \frac{P_{\text{Top}_i}}{2} \\
 \text{for } i \in 1..9 \\
 \text{Qactual}_{\text{Top}_i} \leftarrow \frac{1}{2} (P_{\text{Top}_{i-1}} + P_{\text{Top}_i}) \\
 \text{Qactual}_{\text{Top}_{10}} \leftarrow \frac{P_{\text{Top}_9}}{2} \\
 \text{Qactual}_{\text{Top}}
 \end{array} \right.
 \end{array}$$

5.786
11.682
11.606
11.246
11.222
11.233
11.189
11.152
10.918
10.658
5.25

Qactual_{Top} = 11.233 W

$$\begin{array}{l}
 \text{dQactual}_{\text{Top}} := \left| \begin{array}{l}
 i \leftarrow 0 \\
 \text{dQactual}_{\text{Top}_i} \leftarrow \frac{\sqrt{(V_{\text{Top}_i} \cdot d\text{Current}_{\text{Top}})^2 + (\text{Current}_{\text{Top}} \cdot dV_{\text{Top}})^2}}{2} \\
 \text{for } i \in 1..9 \\
 \text{dQactual}_{\text{Top}_i} \leftarrow \frac{1}{2} \cdot \left[\frac{\sqrt{(V_{\text{Top}_{i-1}} \cdot d\text{Current}_{\text{Top}})^2 + (\text{Current}_{\text{Top}} \cdot dV_{\text{Top}})^2}}{\sqrt{(V_{\text{Top}_i} \cdot d\text{Current}_{\text{Top}})^2 + (\text{Current}_{\text{Top}} \cdot dV_{\text{Top}})^2}} \right] \dots \\
 \text{dQactual}_{\text{Top}_{10}} \leftarrow \frac{\sqrt{(V_{\text{Top}_9} \cdot d\text{Current}_{\text{Top}})^2 + (\text{Current}_{\text{Top}} \cdot dV_{\text{Top}})^2}}{2} \\
 \text{dQactual}_{\text{Top}}
 \end{array} \right.
 \end{array}$$

0.241
0.345
0.346
0.337
0.336
0.339
0.34
0.339
0.338
0.335
0.234

dQactual_{Top} = 0.339 W

$$Q_{in_total} := Q_{actual_Right} + Q_{actual_Bottom} + Q_{actual_Left} + Q_{actual_Top}$$

15.423
31.008
30.448
29.861
30.102
29.921
29.458
29.225
30.082
29.846
14.348

<-- Use to calculate Tbulk ONLY

$$dQ_{in_total} := \sqrt{dQ_{actual_Right}^2 + dQ_{actual_Bottom}^2 + dQ_{actual_Left}^2 + dQ_{actual_Top}^2}$$

0.358
0.511
0.504
0.496
0.499
0.5
0.499
0.499
0.5
0.499
0.353

<-- Use to calculate dTbulk ONLY

$$T_{bulk} := \begin{cases} i \leftarrow 0 \\ T_{bulk_i} \leftarrow \frac{Q_{in_total_i}}{m_{dot} \cdot Cp} + T_{inlet} \\ \text{for } i \in 1..10 \\ T_{bulk_i} \leftarrow \frac{Q_{in_total_i}}{m_{dot} \cdot Cp} + T_{bulk_i-1} \\ T_{bulk} \end{cases}$$

<-- Bulk Temperature calculation, flow through the radial vent

<-- Bulk Temperature Uncertainty

$$dT_{\text{blk}} := \begin{cases} i \leftarrow 0 \\ dT_{\text{blk}_i} \leftarrow \sqrt{\left(\frac{1}{\dot{m} \cdot C_p} \cdot dQ_{\text{in_total}_0}\right)^2 + \left(\frac{-Q_{\text{in_total}_0}}{\dot{m}^2 \cdot C_p} d\dot{m}\right)^2} + dT_{\text{inlet}}^2 \\ \text{for } i \in 1..10 \\ dT_{\text{blk}_i} \leftarrow \sqrt{\left(\frac{1}{\dot{m} \cdot C_p} \cdot dQ_{\text{in_total}_i}\right)^2 + \left(\frac{-Q_{\text{in_total}_i}}{\dot{m}^2 \cdot C_p} d\dot{m}\right)^2} + (dT_{\text{blk}_{i-1}})^2 \\ dT_{\text{blk}} \end{cases}$$

24.741
25.629
26.5
27.355
28.217
29.073
29.916
30.753
31.614
32.468
32.879

$T_{\text{blk}} =$ °C

1
1.001
1.001
1.001
1.002
1.002
1.003
1.003
1.004
1.004
1.004

$dT_{\text{blk}} =$ K

$$\text{HTC}_{\text{Right}} := \begin{cases} i \leftarrow 0 \\ \text{HTC}_{\text{Right}_i} \leftarrow \frac{Q_{\text{actual_Right}_i}}{\frac{\text{Area}_{\text{Right}}}{2} \cdot (T_{\text{RightCu}_i} - T_{\text{blk}_i})} \\ \text{for } i \in 1..9 \\ \text{HTC}_{\text{Right}_i} \leftarrow \frac{Q_{\text{actual_Right}_i}}{\text{Area}_{\text{Right}} \cdot (T_{\text{RightCu}_i} - T_{\text{blk}_i})} \\ \text{HTC}_{\text{Right}} \end{cases}$$

110.303
102.12
100.049
92.277
96.951
95.091
89.439
87.737
93.757
94.173

$\text{HTC}_{\text{Right}} =$ $\frac{\text{W}}{\text{m}^2 \cdot \text{K}}$

$$\text{Augment}_{\text{Right}} := \frac{\text{HTC}_{\text{Right}}}{\text{HTC}_{\text{DB}}}$$

2.189
2.027
1.986
1.831
1.924
1.887
1.775
1.741
1.861
1.869

$$d\text{HTC}_{\text{Right}} := i \leftarrow 0$$

$$d\text{HTC}_{\text{Right}_i} \leftarrow \sqrt{\left[\frac{1}{\text{Area}_{\text{Right}} \cdot \left(T_{\text{RightCu}_i} - T_{\text{blk}_i} \right)} \cdot d\text{Qactual}_{\text{Right}_i} \right]^2 \dots + \left[\frac{-\text{Qactual}_{\text{Right}_i}}{\left(\frac{\text{Area}_{\text{Right}}}{2} \right) \cdot \left(T_{\text{RightCu}_i} - T_{\text{blk}_i} \right)} \cdot d\text{Area}_{\text{Right}} \right]^2 \dots + \left[\frac{-\text{Qactual}_{\text{Right}_i}}{\frac{\text{Area}_{\text{Right}}}{2} \cdot \left(T_{\text{RightCu}_i} - T_{\text{blk}_i} \right)^2} \cdot dT_{\text{RightCu}_i} \right]^2 \dots + \left[\frac{\text{Qactual}_{\text{Right}_i}}{\frac{\text{Area}_{\text{Right}}}{2} \cdot \left(T_{\text{RightCu}_i} - T_{\text{blk}_i} \right)^2} \cdot dT_{\text{blk}_i} \right]^2 \dots}$$

for $i \in 0..9$

$$d\text{HTC}_{\text{Right}_i} \leftarrow \sqrt{\left[\frac{1}{\text{Area}_{\text{Right}} \cdot \left(T_{\text{RightCu}_i} - T_{\text{blk}_i} \right)} \cdot d\text{Qactual}_{\text{Right}_i} \right]^2 \dots + \left[\frac{-\text{Qactual}_{\text{Right}_i}}{\text{Area}_{\text{Right}}^2 \cdot \left(T_{\text{RightCu}_i} - T_{\text{blk}_i} \right)} \cdot d\text{Area}_{\text{Right}} \right]^2 \dots + \left[\frac{-\text{Qactual}_{\text{Right}_i}}{\text{Area}_{\text{Right}} \cdot \left(T_{\text{RightCu}_i} - T_{\text{blk}_i} \right)^2} \cdot dT_{\text{RightCu}_i} \right]^2 \dots + \left[\frac{\text{Qactual}_{\text{Right}_i}}{\text{Area}_{\text{Right}} \cdot \left(T_{\text{RightCu}_i} - T_{\text{blk}_i} \right)^2} \cdot dT_{\text{blk}_i} \right]^2 \dots}$$

$$d\text{HTC}_{\text{Right}}$$

uncertainty percentage :

3.538
5.626
5.674
5.117
5.443
5.313
5.039
4.86
5.392
5.326

$$\frac{W}{m^2 \cdot K}$$

$$Unct_{Right\%} := \frac{dHTC_{Right}}{HTC_{Right}} \cdot 100$$

3.208
5.509
5.671
5.545
5.614
5.588
5.634
5.539
5.751
5.655

$$Unct_{Right\%} =$$

$$HTC_{Bottom} := \begin{cases} i \leftarrow 0 \\ HTC_{Bottom_i} \leftarrow \frac{Q_{actual_{Bottom_i}}}{\frac{Area_{Bottom}}{2} \cdot (T_{Bottom_{Cu_i}} - T_{blk_i})} \\ \text{for } i \in 1..9 \\ HTC_{Bottom_i} \leftarrow \frac{Q_{actual_{Bottom_i}}}{Area_{Bottom} \cdot (T_{Bottom_{Cu_i}} - T_{blk_i})} \\ HTC_{Bottom} \end{cases}$$

82.627
81.024
81.67
76.287
81.436
76.764
76.124
71.633
80.223
77.943

$$HTC_{Bottom} = \frac{W}{m^2 \cdot K}$$

$$Augment_{Bottom} := \frac{HTC_{Bottom}}{HTC_{DB}}$$

1.64
1.608
1.621
1.514
1.616
1.524
1.511
1.422
1.592
1.547

$$Augment_{Bottom} =$$

dHTC_{Bottom} := i ← 0

$$dHTC_{Bottom_i} \leftarrow \sqrt{\left[\frac{1}{\frac{Area_{Bottom}}{2} \cdot (T_{BottomCu_i} - T_{blk_i})} \cdot dQ_{actualBottom_i} \right]^2 \dots + \left[\frac{-Q_{actualBottom_i}}{\left(\frac{Area_{Bottom}}{2}\right)^2 \cdot (T_{BottomCu_i} - T_{blk_i})} \cdot dArea_{Bottom} \right]^2 \dots + \left[\frac{-Q_{actualBottom_i}}{\frac{Area_{Bottom}}{2} \cdot (T_{BottomCu_i} - T_{blk_i})^2} \cdot dT_{BottomCu_i} \right]^2 \dots + \left[\frac{Q_{actualBottom_i}}{\frac{Area_{Bottom}}{2} \cdot (T_{BottomCu_i} - T_{blk_i})^2} \cdot dT_{blk_i} \right]^2}$$

for i ∈ 0..9

$$dHTC_{Bottom_i} \leftarrow \sqrt{\left[\frac{1}{Area_{Bottom} \cdot (T_{BottomCu_i} - T_{blk_i})} \cdot dQ_{actualBottom_i} \right]^2 \dots + \left[\frac{-Q_{actualBottom_i}}{Area_{Bottom}^2 \cdot (T_{BottomCu_i} - T_{blk_i})} \cdot dArea_{Bottom} \right]^2 \dots + \left[\frac{-Q_{actualBottom_i}}{Area_{Bottom} \cdot (T_{BottomCu_i} - T_{blk_i})^2} \cdot dT_{BottomCu_i} \right]^2 \dots + \left[\frac{Q_{actualBottom_i}}{Area_{Bottom} \cdot (T_{BottomCu_i} - T_{blk_i})^2} \cdot dT_{blk_i} \right]^2}$$

dHTC_{Bottom}

uncertainty percentage:

$$d\text{HTC}_{\text{Bottom}} = \frac{W}{m^2 \cdot K}$$

2.77
4.811
4.998
4.441
4.923
4.478
4.44
4.032
4.525
4.342

$$\text{Unct}_{\text{Bottom}}\% := \frac{d\text{HTC}_{\text{Bottom}}}{\text{HTC}_{\text{Bottom}}} \cdot 100$$

$$\text{Unct}_{\text{Bottom}}\% =$$

3.353
5.938
6.12
5.822
6.046
5.833
5.833
5.628
5.64
5.57

$$\text{HTC}_{\text{Left}} := \begin{cases} i \leftarrow 0 \\ \text{HTC}_{\text{Left}_i} \leftarrow \frac{Q_{\text{actual}_{\text{Left}_i}}}{\frac{\text{Area}_{\text{Left}}}{2} \cdot (T_{\text{LeftCu}_i} - T_{\text{blk}_i})} \\ \text{for } i \in 1..9 \\ \text{HTC}_{\text{Left}_i} \leftarrow \frac{Q_{\text{actual}_{\text{Left}_i}}}{\text{Area}_{\text{Left}} \cdot (T_{\text{LeftCu}_i} - T_{\text{blk}_i})} \\ \text{HTC}_{\text{Left}} \end{cases}$$

$$\text{HTC}_{\text{Left}} = \frac{W}{m^2 \cdot K}$$

112.938
100.452
105.139
95.012
98.354
94.335
92.7
90.467
89.684
93.438

$$\text{Augment}_{\text{Left}} := \frac{\text{HTC}_{\text{Left}}}{\text{HTC}_{\text{DB}}}$$

$$\text{Augment}_{\text{Left}} =$$

2.241
1.994
2.087
1.886
1.952
1.872
1.84
1.795
1.78
1.854

$dHTC_{Left} := i \leftarrow 0$

$$dHTC_{Left_i} \leftarrow \sqrt{\left[\frac{1}{\frac{Area_{Left}}{2} \cdot (T_{LeftCu_i} - T_{blk_i})} \cdot dQ_{actual_{Left_i}} \right]^2 \dots + \left[\frac{-Q_{actual_{Left_i}}}{\left(\frac{Area_{Left}}{2}\right)^2 \cdot (T_{LeftCu_i} - T_{blk_i})} \cdot dArea_{Left} \right]^2 \dots + \left[\frac{-Q_{actual_{Left_i}}}{\frac{Area_{Left}}{2} \cdot (T_{LeftCu_i} - T_{blk_i})^2} \cdot dT_{LeftCu_i} \right]^2 \dots + \left[\frac{Q_{actual_{Left_i}}}{\frac{Area_{Left}}{2} \cdot (T_{LeftCu_i} - T_{blk_i})^2} \cdot dT_{blk_i} \right]^2}$$

for $i \in 0..9$

$$dHTC_{Left_1} \leftarrow \sqrt{\left[\frac{1}{Area_{Left} \cdot (T_{LeftCu_1} - T_{blk_1})} \cdot dQ_{actual_{Left_1}} \right]^2 \dots + \left[\frac{-Q_{actual_{Left_1}}}{Area_{Left}^2 \cdot (T_{LeftCu_1} - T_{blk_1})} \cdot dArea_{Left} \right]^2 \dots + \left[\frac{-Q_{actual_{Left_1}}}{Area_{Left} \cdot (T_{LeftCu_1} - T_{blk_1})^2} \cdot dT_{LeftCu_1} \right]^2 \dots + \left[\frac{Q_{actual_{Left_1}}}{Area_{Left} \cdot (T_{LeftCu_1} - T_{blk_1})^2} \cdot dT_{blk_1} \right]^2}$$

$dHTC_{Left}$

uncertainty percentage:

3.806
5.561
5.92
4.981
5.319
4.993
4.948
4.886
4.739
5.064

$$d\text{HTC}_{\text{Left}} = \frac{W}{m^2 \cdot K}$$

$$\text{Unct}_{\text{Left}\%} := \frac{d\text{HTC}_{\text{Left}}}{\text{HTC}_{\text{Left}}} \cdot 100$$

3.37
5.536
5.631
5.242
5.408
5.293
5.338
5.401
5.284
5.42

$$\text{Unct}_{\text{Left}\%} =$$

$$\text{HTC}_{\text{Top}} := \begin{cases} i \leftarrow 0 \\ \text{HTC}_{\text{Top}_i} \leftarrow \frac{Q_{\text{actual_Top}_i}}{\frac{\text{Area}_{\text{Top}}}{2} \cdot (T_{\text{TopCu}_i} - T_{\text{blk}_i})} \\ \text{for } i \in 1..9 \\ \text{HTC}_{\text{Top}_i} \leftarrow \frac{Q_{\text{actual_Top}_i}}{\text{Area}_{\text{Top}} \cdot (T_{\text{TopCu}_i} - T_{\text{blk}_i})} \\ \text{HTC}_{\text{Top}} \end{cases}$$

80.253
75.217
74.729
71.544
68.668
66.809
67.066
66.042
63.976
64.831

$$\text{HTC}_{\text{Top}} = \frac{W}{m^2 \cdot K}$$

$$\text{Augment}_{\text{Top}} := \frac{\text{HTC}_{\text{Top}}}{\text{HTC}_{\text{DB}}}$$

1.593
1.493
1.483
1.42
1.363
1.326
1.331
1.311
1.27
1.287

$$\text{Augment}_{\text{Top}} =$$

dHTC_{Top} := i ← 0

$$dHTC_{Top_i} \leftarrow \sqrt{\left[\frac{1}{\frac{Area_{Top}}{2} \cdot (T_{TopCu_i} - T_{blk_i})} \cdot dQ_{actual_{Top_i}} \right]^2 \dots + \left[\frac{-Q_{actual_{Top_i}}}{\left(\frac{Area_{Top}}{2}\right)^2 \cdot (T_{TopCu_i} - T_{blk_i})} \cdot dArea_{Top} \right]^2 \dots + \left[\frac{-Q_{actual_{Top_i}}}{\frac{Area_{Top}}{2} \cdot (T_{TopCu_i} - T_{blk_i})^2} \cdot dT_{TopCu_i} \right]^2 \dots + \left[\frac{Q_{actual_{Top_i}}}{\frac{Area_{Top}}{2} \cdot (T_{TopCu_i} - T_{blk_i})^2} \cdot dT_{blk_i} \right]^2}$$

for i ∈ 0..9

$$dHTC_{Top_i} \leftarrow \sqrt{\left[\frac{1}{Area_{Top} \cdot (T_{TopCu_i} - T_{blk_i})} \cdot dQ_{actual_{Top_i}} \right]^2 \dots + \left[\frac{-Q_{actual_{Top_i}}}{Area_{Top}^2 \cdot (T_{TopCu_i} - T_{blk_i})} \cdot dArea_{Top} \right]^2 \dots + \left[\frac{-Q_{actual_{Top_i}}}{Area_{Top} \cdot (T_{TopCu_i} - T_{blk_i})^2} \cdot dT_{TopCu_i} \right]^2 \dots + \left[\frac{Q_{actual_{Top_i}}}{Area_{Top} \cdot (T_{TopCu_i} - T_{blk_i})^2} \cdot dT_{blk_i} \right]^2}$$

dHTC_{Top}

uncertainty percentage:

2.631
4.18
4.165
3.962
3.7
3.541
3.579
3.5
3.387
3.536

$$d\text{HTC}_{\text{Top}} = \frac{W}{m^2 K}$$

$$\text{Unct}_{\text{Top}\%} := \frac{d\text{HTC}_{\text{Top}}}{\text{HTC}_{\text{Top}}} \cdot 100$$

3.278
5.558
5.573
5.538
5.388
5.3
5.337
5.299
5.295
5.454

$$\text{Unct}_{\text{Top}\%} =$$

$$\text{HTC}_{\text{avg}} := \text{HTC}_{\text{Right}} \cdot \left(\frac{0.5 \cdot \text{height}}{\text{height} + \text{width}} \right) + \text{HTC}_{\text{Bottom}} \cdot \left(\frac{0.5 \cdot \text{width}}{\text{height} + \text{width}} \right) \dots$$

$$+ \text{HTC}_{\text{Left}} \cdot \left(\frac{0.5 \cdot \text{height}}{\text{height} + \text{width}} \right) + \text{HTC}_{\text{Top}} \cdot \left(\frac{0.5 \cdot \text{width}}{\text{height} + \text{width}} \right)$$

Frition factor Uncertainty

$$f := \frac{\Delta P \cdot D_h}{\Delta X \cdot \frac{1}{2} \cdot \text{density} \cdot \text{Vel}^2}$$

$$\Delta X := 20.25 \text{ n}$$

$$A_{\text{flow}} := \text{height} \cdot \text{width}$$

$$\text{Vel} := \frac{\dot{m}}{\text{density} \cdot A_{\text{flow}}}$$

$$\text{Vel} = 11.192 \frac{\text{m}}{\text{s}}$$

$$d\Delta P := 0.00 \text{ psi}$$

$$f = 0.449$$

$$d\Delta X := 0.25 \text{ n}$$

$$dA_{\text{flow}} := \sqrt{(\text{height} \cdot d\text{width})^2 + (d\text{height} \cdot \text{width})^2}$$

$$d\text{Vel} := \sqrt{\left(\frac{d\dot{m}}{\text{density} \cdot A_{\text{flow}}} \right)^2 + \left(\frac{\dot{m}}{\text{density} \cdot A_{\text{flow}}^2} \cdot dA_{\text{flow}} \right)^2}$$

$$f_{\text{unct}} := \sqrt{\left(\frac{d\Delta P \cdot D_h}{\Delta X \cdot \frac{1}{2} \cdot \text{density} \cdot \text{Vel}^2} \right)^2 + \left(\frac{\Delta P \cdot dD_h}{\Delta X \cdot \frac{1}{2} \cdot \text{density} \cdot \text{Vel}^2} \right)^2 + \left[\left(\frac{-\Delta P \cdot D_h}{\Delta X^2 \cdot \frac{1}{2} \cdot \text{density} \cdot \text{Vel}^2} \cdot d\Delta X \right)^2 \dots \right. \\ \left. + \left(\frac{-2 \cdot \Delta P \cdot D_h}{\Delta X \cdot \frac{1}{2} \cdot \text{density} \cdot \text{Vel}^3} \cdot d\text{Vel} \right)^2 \right]}$$

$$f_{\text{unct}} = 0.052$$

$$\frac{f_{\text{unct}}}{f} = 0.115$$

REFERENCES

- [1] T. Sourmail, *Coating of Turbine Blade*. www.msm.cam.ac.uk/phase-trans/2003/Superalloys/coatings/index.html, University of Cambridge, (2003).
- [2] L. O'Donoghue, *Why don't Gas Turbine Blades burn?* <http://www.ul.ie/elements/Issue6/Gas%20Turbine%20Blades.htm>, University of Limerick
- [3] J. C. Han and P. Zhang, *Effect of rib-angle orientation on local mass transfer distribution in a three-pass rib-roughened channel*. Journal of Turbomachinery. Vol. 113: p. 123 - 130.
- [4] J. C. Han, L. R. Glicksman and W. M. Rohsenow, *An Investigation of Heat Transfer and Friction for Rib-Roughened Surfaces*. International Journal Heat Mass Transfer, 1978. Vol. 21: p. 1143-1156.
- [5] J. C. Han and C. K. Lei, *Heat Transfer and Friction in Square Ducts with Two Opposite Rib-Roughened Walls*. 1983, ASME, 83-HT-26. p. 1 - 8.
- [6] J. C. Han, J.S.Park. and C. K. Lei, *Heat Transfer Enhancement in Channels with Turbulence Promoters*, in ASME, 84-WA/HT-72. 1984. p. 1-8.
- [7] J. C. Han, J.S.Park and C. K. Lei, *Heat transfer Enhancement in Channels with Turbulence Promoters*. Journal of Engineering for Gas Turbines and Power, 1985. Vol. 107: p. 628 - 635.
- [8] J. C. Han, *Heat Transfer and Friction in Channels with Two Opposite Rib-Roughened Walls*. Journal of Heat Transfer, 1984. Vol. 106: p. 774 -781.
- [9] J. C. Han and J. S. Park, *Developing heat transfer in rectangular channels with rib turbulators*. International Journal Heat Mass Transfer, 1988. Vol. 1: p. 183 -195.
- [10] J. C. Han, *Heat Transfer and friction characteristics in rectangular channels with rib turbulators*. Journal of Heat Transfer, 1988. Vol. 110: p. 321 - 328.
- [11] J. C. Han, S. Ou, J. S. Park and C. K. Lei, *Augment heat transfer in rectangular channels of narrow aspect ratios with rib turbulators*. International Journal Heat Mass Transfer, 1989. Vol. 32, No. 9: p. 1619-1630
- [12] J. C. Han and Y. M. Zhang, *High performance heat transfer ducts with parallel broken and V-shaped broken ribs*. International Journal Heat Mass Transfer, 1992. Vol. 35, No. 2: p. 513 - 523.

- [13] R. L. Webb, E. R. G. Eckert and R. J. Goldstein, *Heat Transfer and Friction in tubes*. International Journal Heat Mass Transfer, 1971. Vol. 14: p. 601-617.
- [14] P. R. Chandra, M.E. Niland and J. C. Han, *Turbulent flow heat transfer and friction in a rectangular channel with varying number of ribbed walls*. Journal of Turbomachinery, 1997. Vol. 119: p. 374-380.
- [15] P. R. Chandra, C. R. Alexander and J. C. Han, *Heat Transfer and friction behaviors in rectangular channels with varying number of ribbed walls*. International Journal Heat Mass Transfer, 2003. Vol. 46: p. 481-495.
- [16] P. R. Chandra and J. C. Han, *Pressure drop and mass transfer in two-pass ribbed channels*. Journal of Thermophysics, 1989. Vol. 3, No. 3: p. 315 - 320.
- [17] P. R. Chandra, M. L. Fontenot and J. C. Han, *Effect of rib profiles on turbulent channel flow heat transfer*. Journal of Thermophysics and Heat Transfer, 1998. Vol. 12, No. 1: p. 116 - 118.
- [18] M. E. Taslim and S. D. Spring, *Effects of Turbulator profile and spacing on heat transfer and friction in a channel*. Journal of Thermophysics and Heat Transfer, 1994. Vol. 8, No. 3: p. 555-562.
- [19] M. E. Taslim and C. M. Wadsworth, *An experimental investigation of the rib surface-averaged heat transfer coefficient in a rib roughened square passage*. journal of Turbomachinery, 1997. Vol. 119: p. 381-389.
- [20] M. E. Taslim, T. Li and S. D. Spring *Measurements of heat transfer coefficients and friction factors in passages rib-roughened on all walls*. Journal of Turbomachinery, 1998. Vol. 120: p. 564-570.
- [21] M. E. Taslim, and G. J. Korotky, *Low-aspect-ratio rib heat transfer coefficient measurements in a square channel*. Journal of Turbomachinery, 1998. Vol. 120: p. 831 - 838.
- [22] L. Casarsa, M. Cakan and T. Arts, *Characterization of the velocity and heat transfer fields in an internal cooling channel with high blockage ratio*, in *ASME Turbo Expo. 2002*, GT-2002-30207: Amsterdam. p. 1-8.
- [23] L. M. Wright, and A. S. Gohardani, *Effect of turbulator width and spacing on the thermal performance of angled ribs in a rectangular channel (AR = 3:1)*. in *ASME International Mechanical Engineering Congress and Exposition 2008*. Boston, Massachusetts, USA: ASME.

- [24] M. J. Lewis, *Optimizing the thermohydraulic performance of rough surfaces*. International Journal Heat Mass Transfer, 1975. Vol. 18: p. 1243-1248.
- [25] T. M. Liou, J. J. Hwang, and S. H. Chen, *Turbulent heat transfer and fluid flow in a channel with repeated rib paris*. in *ASME/JSME Thermal Engineering Proceedings*. 1991. Reno, Nevada, USA: ASME.
- [26] T. M. Liou and J. J. Hwang, *Turbulent heat transfer augmentation and friction in periodic fully developed channel flow*. Journal of Heat Transfer, 1992. Vol. 114: p. 56 - 64.
- [27] T. M. Liou, W. B. Wang and Y. J. Chang, *Holographic interferometry study of spatially periodic heat transfer in a channel with ribs detached from one wall*. Journal of Heat Transfer, 1995. Vol. 117: p. 32 - 39.
- [28] E. M. Sparrow and N. Cur, *Turbulent heat transfer in a symmetrically or asymmetrically heated flat rectangular duct with flow separation at inlet*. Journal of Heat Transfer, 1992. Vol. 104: p. 82 - 89.
- [29] S. Kakaç, R. K. Shah and W. Aung, *Handbook of single-phase convective heat transfer*. 1987: John Wiley & Sons. 76.
- [30] Y. M. Zhang, W. Z. Gu, and J. C. Han, *Heat transfer and friction in rectangular channels with ribbed or ribbed-grooved walls*. Journal of Heat Transfer, 1994. Vol. 116: p. 58-65.
- [31] C. O. Olsson and B. Sunden, *Experimental Study of flow and heat transfer in rib-roughened rectangular channels*. Experimental thermal and Fluid Science, 1998. Vol. 16: p. 349-365.
- [32] L. Cai, O. Hidehiro, H. Masafumi, N. Hiroshi and F. Hideomi, *Influence of channel aspect ratio on heat transfer characteristics in sharp-turn connected two-pass channels with inclined divider wall*. Experimental thermal and Fluid Science, 2004. Vol. 28: p. 513 - 523.
- [33] S. W. Chang, T. M. Liou, and M. H. Lu, *Heat transfer of rectangular narrow channel with two opposite scale-roughened walls*. International Journal Heat Mass Transfer, 2005. Vol. 48: p. 3921 - 3931.
- [34] J. C. Han, S. Dutta, and S. Ekkad, *Gas turbine heat transfer and cooling technology*. 2000: Taylor & Francis.
- [35] P. M. Ligrani, M. M. Oliveria, and T. Blaskovich, *Comparison of heat transfer augmentation techniques*. AIAA Journal, 2003. Vol. 41, No. 3: p. 337 - 362.

- [36] S. J. Kline, and F. A. McClintock, *Describing uncertainties in single-sample experiments*. Mechanical Engineering, 1953. Vol. 75: p. 3 - 8.
- [37] R. W. Fox, A. T. McDonald, and P. J. Pritchard, *Introduction to Fluid Mechanics*. Sixth ed. 2004: John Wiley & Sons, Inc.